

Ab initio perspective on hydrogenated amorphous silicon for thin-film and heterojunction photovoltaics

Philippe Czaja

Energie & Umwelt / Energy & Environment

Band / Volume 494

ISBN 978-3-95806-474-4

Forschungszentrum Jülich GmbH
Institut für Energie- und Klimaforschung
IEK-5 Photovoltaik

Ab initio perspective on hydrogenated amorphous silicon for thin-film and hetero- junction photovoltaics

Philippe Czaja

Schriften des Forschungszentrums Jülich
Reihe Energie & Umwelt / Energy & Environment

Band / Volume 494

ISSN 1866-1793

ISBN 978-3-95806-474-4

Bibliografische Information der Deutschen Nationalbibliothek.
Die Deutsche Nationalbibliothek verzeichnet diese Publikation in der
Deutschen Nationalbibliografie; detaillierte Bibliografische Daten
sind im Internet über <http://dnb.d-nb.de> abrufbar.

Herausgeber und Vertrieb: Forschungszentrum Jülich GmbH
Zentralbibliothek, Verlag
52425 Jülich
Tel.: +49 2461 61-5368
Fax: +49 2461 61-6103
zb-publikation@fz-juelich.de
www.fz-juelich.de/zb

Umschlaggestaltung: Grafische Medien, Forschungszentrum Jülich GmbH

Druck: Grafische Medien, Forschungszentrum Jülich GmbH

Copyright: Forschungszentrum Jülich 2020

Schriften des Forschungszentrums Jülich
Reihe Energie & Umwelt / Energy & Environment, Band / Volume 494

D 77 (Diss. Mainz, Univ., 2019)

ISSN 1866-1793
ISBN 978-3-95806-474-4

Vollständig frei verfügbar über das Publikationsportal des Forschungszentrums Jülich (JuSER)
unter www.fz-juelich.de/zb/openaccess.



This is an Open Access publication distributed under the terms of the [Creative Commons Attribution License 4.0](https://creativecommons.org/licenses/by/4.0/), which permits unrestricted use, distribution, and reproduction in any medium, provided the original work is properly cited.

Abstract

Hydrogenated amorphous silicon (a-Si:H) has applications in photovoltaics as an absorber material in thin-film solar cells and as a passivation material in silicon-heterojunction cells, where it forms an interface with the crystalline silicon (c-Si) absorber. The physical processes occurring at this interface have crucial impact on the characteristics of the entire photovoltaic device. The key to improving the solar cell performance lies therefore in the optimization of the interface, in particular with respect to its transport and recombination properties. This requires a profound understanding of the microscopic structure of a-Si:H and a-Si:H/c-Si interfaces, and of its effect on the macroscopic properties relevant for photovoltaics, such as absorption, optical and mobility gap, band offsets, and local density of gap states. In this thesis we present an ab initio study that seeks to provide insight into the atomic and electronic structure of bulk a-Si:H and a-Si:H/c-Si interfaces, extract the relevant electronic and optical properties, and explore the computational limitations that have to be overcome in order to arrive at a predictive ab initio simulation of the silicon heterojunction.

In the first step bulk a-Si:H is investigated, for which we use atomic configurations of a-Si:H with 72 and 576 atoms, respectively. These were generated with ab initio molecular dynamics, where the larger structures are defect free, closely matching the experimental situation and enabling the comparison of the electronic and optical properties with experimental results. Density functional theory calculations are applied to both configurations in order to obtain the electronic wave functions. These are analyzed and characterized with respect to their localization and their contribution to the density of states, and are used for calculating ab initio absorption spectra of a-Si:H. The results show that both the size and the defect structure of the configurations affect the electronic and optical properties and in particular the values of the optical and mobility gap. These values can be improved by calculating quasiparticle (QP) corrections to the single-particle spectra using the G_0W_0 method. Thereby we find that the QP corrections can be described by a set of scissors shift parameters, which can also be used in calculations of larger structures. The analysis of individual contributions to the absorption by evaluating the optical matrix elements indicates that strong localization enhances the optical coupling, but has little effect on the average transition probability, for which we find a dependence $E^2 + \text{const}$ on the photon energy E , irrespective of the nature of the initial or final state.

In the second step the previously analyzed defect-free a-Si:H structure is combined with c-Si to form a realistic a-Si:H/c-Si interface structure, which undergoes a high-temperature annealing in order to obtain a very low defect density. Throughout the annealing, we monitor the evolution of the structural and electronic properties. The analysis of the bonds by means of the electron localization function reveals that dangling bonds move toward the free a-Si:H surface, leaving the interface region itself completely defect free. The hydrogen follows this movement, which indicates that in the case under consideration, hydrogen passivation does not play a significant role at the interface. A configuration with a satisfactory low density of defect states is reached after annealing at 700 K. A detailed characterization of the electronic states in this configuration in terms of their energy, localization, and location reveals that, despite

the absence of dangling bonds near the interface, localized interface states still exist, lying mostly below the conduction band edge from where they seem to move deeper into the gap throughout the annealing. The quantitative description of electronic localization also allows for the determination of the a-Si:H mobility gap, which, together with the c-Si band gap, yields band offsets that are in qualitative agreement with experimental observations. We find, however, that the error in determining the band edges is too large for an accurate calculation of the band offsets, and can be decreased only by using larger configurations.

Zusammenfassung

Hydrogenisiertes amorphes Silizium (a-Si:H) findet in der Photovoltaik Anwendung als Absorbermaterial in Dünnschicht-Solarzellen und als Passivierungsmaterial in Silizium-Heterostruktur-Zellen, wo es eine Grenzfläche mit dem kristallinen Silizium (c-Si) Absorber bildet. Die physikalischen Prozesse, die an dieser Grenzfläche auftreten, haben entscheidenden Einfluss auf die Eigenschaften der gesamten Solarzelle. Der Schlüssel zur Verbesserung der Solarzellenleistung liegt daher in der Optimierung der Grenzfläche, insbesondere hinsichtlich ihrer Transport- und Rekombinationseigenschaften. Dies erfordert ein tiefgreifendes Verständnis der mikroskopischen Struktur von a-Si:H und a-Si:H/c-Si-Grenzflächen und ihres Einflusses auf die für die Photovoltaik relevanten makroskopischen Eigenschaften, wie Absorption, optische und Mobilitäts-Bandlücke, Bandversätze und lokale Dichte von Zuständen in der Bandlücke. In dieser Arbeit präsentieren wir eine ab-initio-Studie, die anstrebt, Einblick in die atomare und elektronische Struktur von a-Si:H und a-Si:H/c-Si-Grenzflächen zu geben, die relevanten elektronischen und optischen Eigenschaften zu extrahieren und die numerischen Einschränkungen zu untersuchen, die überwunden werden müssen, um das Ziel einer prädiktive ab-initio-Simulation der Silizium-Heterostruktur zu erreichen.

Im ersten Schritt wird reines a-Si:H untersucht, wofür wir atomare Konfigurationen von a-Si:H mit 72 bzw. 576 Atomen verwenden. Diese wurden mittels ab-initio-Molekulardynamik erzeugt, wobei die größeren Strukturen defektfrei sind, was gut mit der experimentellen Situation übereinstimmt und den Vergleich der elektronischen und optischen Eigenschaften mit experimentellen Ergebnissen ermöglicht. Für beide Konfigurationen werden Dichtefunktionaltheorie-Rechnungen durchgeführt, um die elektronischen Wellenfunktionen zu erhalten. Diese werden analysiert und hinsichtlich ihrer Lokalisierung und ihres Beitrags zur Zustandsdichte charakterisiert, und werden außerdem zur Berechnung von ab-initio-Absorptionsspektren von a-Si:H verwendet. Die Ergebnisse zeigen, dass sowohl die Größe als auch die Defektstruktur der Konfigurationen die elektronischen und optischen Eigenschaften beeinflussen, insbesondere die Werte der optischen und der Mobilitäts-Bandlücke. Diese Werte können durch die Berechnung von Quasiteilchen-Korrekturen der Ein-Teilchen-Spektren mittels der G_0W_0 -Methode verbessert werden. Dabei stellen wir fest, dass die Quasiteilchen-Korrekturen durch einen Satz von scissors-shift-Parametern beschrieben werden können, der sich auch bei Rechnungen mit größeren Strukturen verwenden lässt. Die Analyse der einzelnen Beiträge zur Absorption durch Auswertung der optischen Matrixelemente weist darauf hin, dass starke Lokalisierung die optische Kopplung verstärkt, jedoch wenig Einfluss auf die durchschnittliche Übergangswahrscheinlichkeit hat, für die wir eine Abhängigkeit $E^2 + \text{const}$ von der Photonenenergie E ermitteln, unabhängig von der Art des Ausgangs- oder Endzustandes.

Im zweiten Schritt wird die zuvor analysierte defektfreie a-Si:H-Struktur mit c-Si kombiniert, um eine realistische a-Si:H/c-Si-Grenzflächenstruktur zu bilden, die einem Hochtemperatur-Tempers unterzogen wird, um eine sehr geringe Defektdichte zu erlangen. Während des Tempers überwachen wir die Entwicklung der strukturellen und elektronischen Eigenschaften. Die Analyse der Bindungen mittels der Elektronenlokalisierungsfunktion zeigt, dass sich offene

Bindungen in Richtung der freien a-Si:H-Oberfläche bewegen, wodurch der Grenzflächenbereich selbst vollständig defektfrei wird. Der Wasserstoff folgt dieser Bewegung, was darauf hindeutet, dass die Wasserstoffpassivierung im betrachteten Fall an der Grenzfläche keine wesentliche Rolle spielt. Eine Konfiguration mit einer zufriedenstellend geringen Defektdichte wird nach Tempern bei 700 K erreicht. Eine detaillierte Charakterisierung der elektronischen Zustände in dieser Konfiguration hinsichtlich ihrer Energie, ihrer Lokalisierung und ihrer räumlichen Position zeigt, dass, trotz der Abwesenheit offener Bindungen nahe der Grenzfläche, lokalisierte Grenzflächenzustände vorhanden sind, welche überwiegend unterhalb der Leitungsbandkante liegen, von wo aus sie sich während des Temperns tiefer in die Bandlücke zu bewegen scheinen. Die quantitative Beschreibung der elektronischen Lokalisierung ermöglicht auch die Bestimmung der a-Si:H-Mobilitätsücke, welche, zusammen mit der c-Si-Bandlücke, Bandversätze liefert, die mit experimentellen Beobachtungen qualitativ übereinstimmen. Wir stellen jedoch fest, dass der Fehler beim Bestimmen der Bandkanten zu groß für eine genaue Berechnung der Bandversätze ist und nur durch die Verwendung größerer Konfigurationen verringert werden kann.

Contents

1	Introduction	9
2	Theory and Methods	13
2.1	Density functional theory	13
2.1.1	The many-particle Hamiltonian	13
2.1.2	The Hohenberg-Kohn theorem	14
2.1.3	The Kohn-Sham formalism	15
2.1.4	The exchange-correlation functional	17
2.1.5	The plane-wave pseudopotential method	18
2.2	Quasiparticle corrections	20
2.2.1	Quasiparticles	21
2.2.2	GW approximation	22
2.2.3	Practical calculation	24
2.2.4	Scissors shift	25
2.3	Characterization methods	26
2.3.1	Radial pair correlation function	26
2.3.2	Bonding and the ELF	26
2.3.3	Density of states	31
2.3.4	Electronic localization	31
2.3.5	Mobility gap	36
2.3.6	Optical characterization	38
3	Hydrogenated amorphous silicon	46
3.1	Introduction	46
3.2	Computational details	48
3.3	Structural properties	51
3.4	Electronic properties	55
3.5	Optical properties	59
3.5.1	G_0W_0 calculations	60
3.5.2	Absorption spectrum	60
3.5.3	JDOS and optical matrix elements	63
3.6	Conclusions	68
4	The a-Si:H/c-Si interface	71
4.1	Introduction	71
4.2	Computational details	72
4.3	Structural and electronic properties	75
4.3.1	Atomic structure	75
4.3.2	Density of states and band offsets	76
4.3.3	Localized states	80
4.4	Evolution upon high-temperature annealing	82
4.4.1	Structural evolution	82
4.4.2	Evolution of electronic properties	87
4.5	Effect of surface passivation	92

4.6 Conclusions	92
5 Conclusions	96
Bibliography	98

1 Introduction

Silicon, both in its crystalline and amorphous phase, plays an important role in photovoltaics. Despite the advances of new materials, such as copper indium gallium selenide (CIGS) and cadmium telluride (CdTe), and technologies, like perovskite or organic photovoltaics, silicon-based solar cells still account for 93.3% of the global annual production. Thereby, mono- and multi-crystalline wafer based cells have a combined market share of 93.0%, whereas the market share of amorphous silicon thin-film solar cells has decreased to 0.3% in 2017 [1]. However, in addition to its role as an absorber material in thin-film cells, (hydrogenated) amorphous silicon (a-Si:H) has recently found a new important application as a passivation layer in silicon-heterojunction (SHJ) cells, which is the main motivation for our interest in the microscopic modeling of a-Si:H and amorphous-crystalline (a-Si:H/c-Si) interfaces.

Understanding and simulating the SHJ cell demands a multi-scale approach that relates the local microstructure to the global device characteristics [2]. At the microscopic level, which is covered within this work, this requires the accurate description of the atomic and electronic structure at the interface, which is best captured by ab initio methods. Based on this information, material properties have to be extracted, which can be used as parameters in meso- and macroscopic simulations, and to establish the structure-property relations. Along these lines, the aim of this thesis is to contribute to the understanding of the local microstructure at the a-Si:H/c-Si interface and its impact on the cell characteristics, and to advance towards the goal of a fully ab initio based simulation of the SHJ that allows for the prediction of the relevant macroscopic material properties from the microscopic structure.

In order to understand what the relevant material properties are in the context of photovoltaics in general and heterojunctions in particular, we briefly recapitulate the working principle of a

n p

Figure 1.1: Working principle of a solar cell. An electron-hole pair is generated by photon absorption in the absorber. The charge carriers are then separated by a p-n-junction and are collected at the carrier-selective terminals. [3]

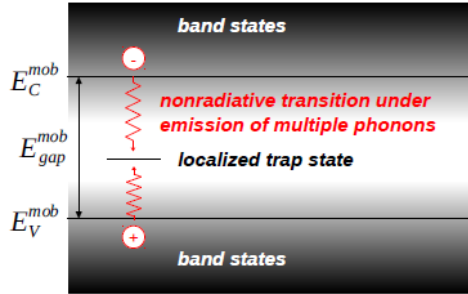


Figure 1.2: Shockley-Read-Hall recombination in amorphous silicon. Under emission of one or multiple phonons, an electron and a hole close to the mobility edge ($E_{v/c}^{mob}$) fall into a localized state deep inside the mobility gap (E_{gap}^{mob}), where they are trapped and recombine.

solar cell (Fig. 1.1). A basic solar cell consists of a p-n-junction, i.e., an interface between a p-doped and an n-doped semiconductor, and contacts on the front and the back surface. Upon absorption of a photon in one of the semiconductor layers – the absorber – an electron-hole pair is generated, meaning that an electron is excited into the conduction band, leaving a hole in the valence band. The generated carriers move through the semiconductor and are separated at the p-n-junction, which serves as a selective barrier, letting electrons only pass in one direction, and holes only in the other direction. If the carriers reach the surface before recombining, they are collected at the contacts and contribute to the photo current.

The total number of electrons being collected in relation to the number of incident photons is called the external quantum efficiency (EQE), which, among other factors, drives the overall solar cell efficiency. It depends on the rate of photons absorbed and the rate of carriers recombining. Microscopically, the rate of photon absorption depends on the absorption coefficient of the absorber material, and in particular on its optical gap, i.e., the photon energy that is at least required to excite an electron from the valence into the conduction band. Bulk recombination is driven by three different mechanisms: radiative, Auger, and Shockley-Read-Hall (SRH) recombination. As radiative and Auger recombination strongly depend on the doping density, the dominant recombination mechanism in intrinsic (undoped) amorphous semiconductors is the SRH recombination. The latter, as visualized in Fig. 1.2, occurs via trap states, which are spatially localized and energetically situated inside the gap. The recombination rate therefore depends on the (local) density of gap states, as well as their energies and capture cross sections, i.e., the probabilities of capturing an electron or a hole.

In addition to bulk recombination, the EQE is limited by recombination at the surface contacts, i.e., by electrons reaching the positive contact or holes reaching the negative contact instead of being swept over the p-n-junction. The SHJ cell solves this problem by embedding the c-Si absorber in a-Si:H passivation layers. The larger gap of the a-Si:H induces band offsets at the interfaces that provide selective barriers for the charge carriers (Fig. 1.3), preventing them from recombining at the surface. Therefore, these offsets, in combination with the band bending induced by doped layers (field-effect passivation), determine the surface recombination rate, as well as the charge transport through the interfaces. Additionally, the larger optical gap of the

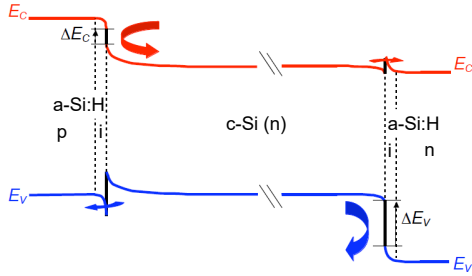


Figure 1.3: Band diagram of a basic silicon-heterojunction cell. The c-Si absorber is embedded in two a-Si:H passivation layers. The band offsets $\Delta E_{v/c}$ at the interfaces give rise to selective barriers, preventing electrons from reaching the positive contact (left) and holes from reaching the negative contact (right), while allowing the respective other type of carrier to tunnel through. [4]

passivation material acts as a window for incident light, which means that its value controls the absorption losses in the front passivation layer. Another passivation mechanism attributed to the intrinsic a-Si:H layers is the passivation of dangling bonds (chemical passivation), which is supposed to be related to the hydrogen concentration in the intrinsic layer.

The accurate description of the microscopic structure of the a-Si:H/c-Si interface first requires to find a suitable model structure of a-Si:H, which can then be combined with c-Si to model the interface. This is why, in the first step, we analyze model structures of bulk a-Si:H with respect to their ability to describe the actual experimental properties of a-Si:H, before moving on to the interface structure. This approach also allows us to detect the impact of computational artifacts that limit the accuracy of the calculations, without the disruptive influence of surfaces, interfaces, and defects.

Both the modeling of bulk a-Si:H and the a-Si:H/c-Si interface follows the same procedure. In the first step, atomic configurations are generated using ab initio molecular dynamics. This step was not performed within this thesis, but the respective structures were provided as part of a collaboration with the ENEA Casaccia Research Center. In the second step, the electronic structure is calculated using density functional theory. In the third step, various methods are applied to obtain the microscopic and macroscopic material properties. The simulation flow is visualized in Fig. 1.4.

This thesis consists of three main parts. In the first part, all the theory and methods that came to use within this work are introduced. Following this, the results are presented and discussed, where the second part deals with bulk a-Si:H, and the third part covers the a-Si:H/c-Si interface. Parts of this work have been pre-published in the form of conference proceedings and journal articles [2, 5–7].

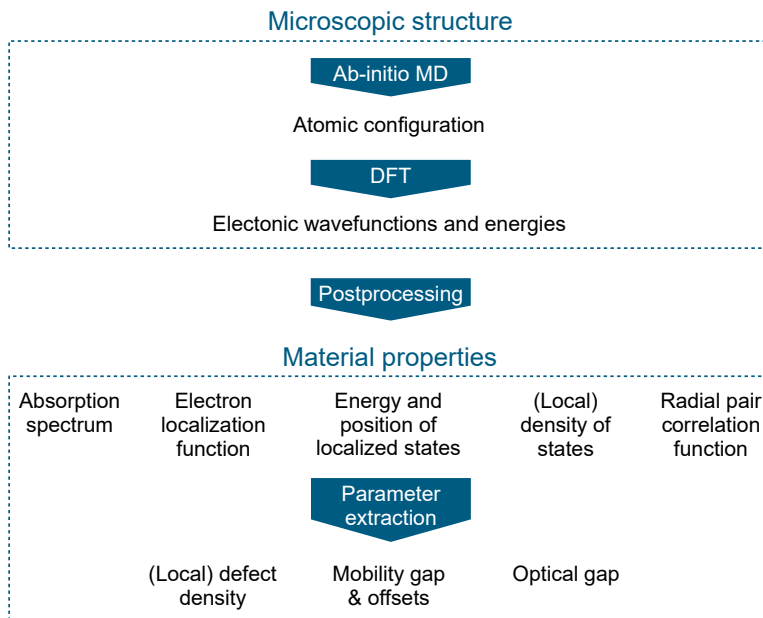


Figure 1.4: Simulation flow for the modeling of a-Si:H and a-Si:H/c-Si interfaces.

2 Theory and Methods

This chapter describes the computational methods employed in the course of this work and explains the underlying theory. The first section is dedicated to the density functional theory (DFT), which is used to calculate the electronic structure of all the a-Si:H and a-Si:H/c-Si configurations, and forms the basis of all further calculations. The second section deals with the quasiparticle corrections, which serve the purpose of improving the results obtained with DFT. The third section finally introduces all the methods used for the structural, electronic, and optical characterization of the previously calculated configurations. In order to keep the notation as simple as possible, atomic units are used throughout the whole chapter.

2.1 Density functional theory

Density functional theory (DFT) is one of the most widely used electronic-structure methods in theoretical condensed-matter physics and computational material science. It allows, in principle, to calculate all ground-state properties of a many-particle system, based only on the knowledge of the atomic structure. This section is supposed to provide a short overview over the basic theorems and equations that form the foundation of DFT, and is restricted to the zero-temperature and spin-independent case, as all calculations within this thesis have been performed under these conditions. For a more detailed treatment of DFT the reader is referred to the large amount of literature covering this topic, e.g., the books of Martin [8] or Kohanoff [9].

2.1.1 The many-particle Hamiltonian

A many-particle system consisting of electrons and nuclei is described by the Hamiltonian

$$H = T + U + V + W \quad (2.1)$$

with the kinetic-energy operator

$$T = -\frac{1}{2} \sum_i \nabla_i^2, \quad (2.2)$$

where ∇_i is the gradient with respect to the spatial coordinates \mathbf{r}_i of the i th electron, the Coulomb energy of the electrons

$$U = \frac{1}{2} \sum_{i \neq j} \frac{1}{|\mathbf{r}_i - \mathbf{r}_j|}, \quad (2.3)$$

the energy of the electrons in the nuclear potential $v(\mathbf{r})$,

$$V = \sum_i v(\mathbf{r}_i) = - \sum_{i,I} \frac{Z_I}{|\mathbf{r}_i - \mathbf{R}_I|}, \quad (2.4)$$

where \mathbf{R}_I and Z_I are the position and charge of the I th nucleus, and the Coulomb energy of the nuclei

$$W = \frac{1}{2} \sum_{I \neq J} \frac{Z_I Z_J}{|\mathbf{R}_I - \mathbf{R}_J|} . \quad (2.5)$$

If the electronic and nuclear degrees of freedom are assumed to be decoupled (Born-Oppenheimer approximation), then the electronic ground state is obtained by solving the Schrödinger equation for the many-electron wave function Ψ ,

$$(T + U + V) \Psi (\{ \mathbf{r}_i \}) = E \Psi (\{ \mathbf{r}_i \}) , \quad (2.6)$$

in which the nuclear degrees of freedom appear only in the static potential $v(\mathbf{r})$. T and U are universal operators, i.e., they do not depend on the kind of system under consideration. Hence, if the nuclear positions $\{ \mathbf{R}_I \}$ and therefore the potential $v(\mathbf{r})$ are known, (2.6) can, in theory, be solved, providing all ground-state properties of the system. In practice, however, for any real material the number of degrees of freedom is of the order of 10^{23} , which makes the calculation of the many-electron wave function impossible. The key idea behind DFT is therefore to map the interacting many-electron system onto an effective system of non-interacting electrons moving in a mean field, such that the many-electron wave function $\Psi(\{ \mathbf{r}_i \})$ can be replaced by a set of single-electron wave functions $\psi_i(\mathbf{r})$ without losing any information. The theoretical foundation of this idea is provided by the Hohenberg-Kohn theorem.

2.1.2 The Hohenberg-Kohn theorem

The Hohenberg-Kohn theorem [10] consists of two central statements:

1. The non-degenerate many-electron ground state Ψ_0 is a unique functional of the ground-state electron density $n_0(\mathbf{r})$, i.e.,

$$\Psi_0 (\{ \mathbf{r}_i \}) = \Psi [n_0(\mathbf{r})] \quad (2.7)$$

2. For any given potential $v(\mathbf{r})$ there exists an energy functional $E_v[n]$, such that

$$E_v [n_0] \leq E_v [n] \quad \forall n , \quad (2.8)$$

i.e., n_0 minimizes the energy functional and yields the ground-state energy.

The Hohenberg-Kohn theorem thus states that all the information contained in the N -electron wave function, which is a function of $3N$ variables, is also contained in the ground-state density, being a function of only three variables. From this it follows that also the ground-state expectation value of any operator A can be calculated as an implicit functional of n_0 :

$$A_0 = \langle \Psi [n_0] | A | \Psi [n_0] \rangle = A [n_0] . \quad (2.9)$$

Moreover, the ground-state density can theoretically be found by minimizing the energy functional

$$E_v [n] = \langle \Psi [n] | T + U + V | \Psi [n] \rangle = T[n] + U[n] + V[n] \quad (2.10)$$

with respect to n under the constraint

$$\int d\mathbf{r} n(\mathbf{r}) = N \quad (2.11)$$

(conservation of particle number). In practice, however, only $V[n]$ is known as an explicit functional of n ,

$$V[n] = \int d\mathbf{r} v(\mathbf{r})n(\mathbf{r}) , \quad (2.12)$$

whereas the explicit dependence of the universal functionals $T[n]$ and $U[n]$ on the density is in general unknown and has to be approximated.

2.1.3 The Kohn-Sham formalism

In order to find explicit expressions for the functionals $T[n]$ and $U[n]$, the Kohn-Sham approach [11] substitutes the interacting many-particle system by a system of non-interacting electrons, using the fact that, according to the Hohenberg-Kohn theorem, the interacting system can be substituted by any auxiliary system that has the same ground-state density n_0 , without losing any information. The many-particle wave function is then given by a product of single-particle wave functions ψ_i , which obey the Schrödinger equation

$$\left(-\frac{1}{2}\nabla^2 + v_s[n](\mathbf{r}) \right) \psi_i(\mathbf{r}) = \epsilon_i \psi_i(\mathbf{r}) , \quad (2.13)$$

where $v_s[n]$ is a (yet unknown) effective potential. The total kinetic energy of this system is given by the sum of the kinetic energies of the electrons,

$$T_s = -\frac{1}{2} \sum_i^{\text{occ}} \int d\mathbf{r} \psi_i^*(\mathbf{r}) \nabla^2 \psi_i(\mathbf{r}) , \quad (2.14)$$

and the interaction energy is given by the electrostatic Hartree energy,

$$U_H[n] = \frac{1}{2} \int \int d\mathbf{r} d\mathbf{r}' \frac{n(\mathbf{r})n(\mathbf{r}')}{|\mathbf{r} - \mathbf{r}'|} , \quad (2.15)$$

which is an explicit functional of the density

$$n(\mathbf{r}) = \sum_i^{\text{occ}} |\psi_i(\mathbf{r})|^2 . \quad (2.16)$$

Since the set $\{\psi_i\}$ are themselves functionals of n , as they depend on $v_s[n]$, also T_s is an implicit functional of n : $T_s[n] = T_s[\{\psi_i[n]\}]$. The total energy functional can now be written as

$$E_v[n] = T_s[n] + U_H[n] + V[n] + E_{\text{xc}}[n] , \quad (2.17)$$

where

$$E_{\text{xc}}[n] = (T[n] - T_s[n]) + (U[n] - U_H[n]) \quad (2.18)$$

is the exchange-correlation (xc) energy, containing all terms arising from the fact that the interacting wave function Ψ_0 is in fact not just a product of single-particle wave functions. Even though these terms are not known in practice, (2.17) is formally exact and therefore, according to the Hohenberg-Kohn theorem, its minimization will yield the exact ground-state density n_0 . To account for the fact that T_s is known explicitly only as a functional of $\{\psi_i\}$, the minimization with respect to n is recast into a minimization with respect to $\{\psi_i\}$, using (2.13), which yields the set of equations

$$\frac{\delta}{\delta\psi_i^*(\mathbf{r})} \left(T_s[n] + U_H[n] + V[n] + E_{xc}[n] - \mu_i \int d\mathbf{r} n(\mathbf{r}) \right) = 0 \quad (2.19)$$

$$\Rightarrow \left(-\frac{1}{2}\nabla^2 + v_H[n](\mathbf{r}) + v(\mathbf{r}) + v_{xc}[n](\mathbf{r}) \right) \psi_i(\mathbf{r}) = \mu_i \psi_i(\mathbf{r}) , \quad (2.20)$$

where μ_i are the Lagrange multipliers,

$$v_H[n](\mathbf{r}) = \int d\mathbf{r}' \frac{n(\mathbf{r}')}{|\mathbf{r} - \mathbf{r}'|} \quad (2.21)$$

is the Hartree potential, and

$$v_{xc}[n](\mathbf{r}) = \frac{\delta E_{xc}}{\delta n(\mathbf{r})} \quad (2.22)$$

is the xc-potential. Comparison with (2.13) shows that

$$v_s[n](\mathbf{r}) = v_H[n](\mathbf{r}) + v(\mathbf{r}) + v_{xc}[n](\mathbf{r}) \quad (2.23)$$

is the effective potential in which the non-interacting electrons move, and the Lagrange multipliers μ_i give the single-particle energies ϵ_i . Consequently, solving the non-interacting Schrödinger equation (2.13) is equivalent to solving the minimization problem (2.19) for the interacting system and will therefore yield the same ground-state density n_0 . Equations (2.13), (2.16), and (2.23) are known as the Kohn-Sham equations and have to be solved self-consistently. They replace the problem of finding the N -particle wave function Ψ_0 with the much easier problem of finding a set of N one-particle wave functions. However, while the two problems are formally equivalent, in practice the Kohn-Sham equations can only be formulated approximately due to the unknown form of the xc-functional. The accuracy of DFT is therefore fundamentally dependent on the choice of this functional, which will be further discussed in section 2.1.4.

Another common approximation, even though not inherent in DFT, is to interpret the eigenvalues ϵ_i of the auxiliary system as the actual electron binding energies. This interpretation is in principle not correct, because, even though DFT in theory reproduces all ground-state properties exactly, this does not hold for the band structure, since the single-electron energies ϵ_i are not observables of the original many-body system. Nevertheless, in many cases the independent-particle picture approximates the actual system well enough to yield very good agreement between the DFT and the experimental band structure for the occupied states. Excitation energies on the other hand suffer from the fact that they are still calculated from the ground-state density, i.e., the effects of adding or removing an electron on the effective potential are not taken into account. These many-body effects lead to a systematic underestimation of the band gap in DFT and will be discussed in section 2.2.

2.1.4 The exchange-correlation functional

As explained before, the exchange-correlation (xc) energy takes into account all many-electron interactions beyond the Hartree energy. It is therefore the difference in energy arising from replacing the product of one-particle wave functions by a more general Ansatz for the many-body wave function Ψ_0 . As the former will, according to the Hohenberg-Kohn theorem, yield an energy higher than the ground-state energy, it follows that $E_{xc} \leq 0$. Descriptively this means that xc-interactions lead to a repulsion between the electrons, such that E_{xc} can be formally written as

$$E_{xc}[n] = \frac{1}{2} \int \int d\mathbf{r} d\mathbf{r}' \frac{n(\mathbf{r})n_{xc}(\mathbf{r}, \mathbf{r}')}{|\mathbf{r} - \mathbf{r}'|}, \quad (2.24)$$

with the so-called xc-hole $n_{xc}(\mathbf{r}, \mathbf{r}')$, fulfilling

$$\int d\mathbf{r}' n_{xc}(\mathbf{r}, \mathbf{r}') = -1, \quad (2.25)$$

which describes the reduced probability of finding another electron in the vicinity of an electron at position \mathbf{r} . Even though a number of other exact properties of the xc-functional are known [12], an explicit expression for $E_{xc}[n]$ can only be given approximately. As this, however, usually constitutes only a small part of the total energy functional, DFT can still yield accurate results, especially compared to methods that completely neglect either exchange (Thomas-Fermi approximation [13, 14]) or correlation (Hartree-Fock approximation [15, 16]). In the case of strongly correlated materials such as transition metal oxides however, i.e., when the correlation term becomes comparable in magnitude to the other terms of the energy functional, the approximation breaks down.

A common and intuitive approach to approximating $E_{xc}[n]$ is the local density approximation (LDA), which takes the xc-energy density $e_{xc}^{\text{hom}}(n)$ of a homogeneous electron gas with density n , and uses its value at $n = n(\mathbf{r})$ as a local approximation for e_{xc} , i.e.,

$$e_{xc}^{\text{LDA}}(\mathbf{r}) = e_{xc}^{\text{hom}}(n) \Big|_{n=n(\mathbf{r})} \quad (2.26)$$

$$\Rightarrow E_{xc}^{\text{LDA}}[n] = \int d\mathbf{r} e_{xc}^{\text{hom}}(n(\mathbf{r})). \quad (2.27)$$

Thereby, the exchange part of e_{xc}^{hom} is exactly known to be [12]

$$e_x^{\text{hom}}(n) = -\frac{3}{4} \left(\frac{3}{\pi} \right)^{1/3} n^{4/3}. \quad (2.28)$$

The correlation part is not known exactly, but very good parameterizations [17, 18], based on highly precise Quantum Monte Carlo calculations [19], exist nowadays. The drawback of the LDA is that it does not account for the non-locality of e_{xc} [20], and therefore, in principle, should only work in the limiting case of a slowly varying density [11]. The reason why LDA has still proven successful for a wide range of systems, is the systematic cancellation of errors between the exchange and the correlation term for typical valence electron densities [20]. Nevertheless, improvement can often be reached by taking into account non-locality in the

form of the local change $\nabla n(\mathbf{r})$ to the density, which is known as the generalized gradient approximation (GGA) [21]. Functionals of this type have the form

$$E_{\text{xc}}^{\text{GGA}}[n] = \int d\mathbf{r} e_{\text{xc}}^{\text{GGA}}(n(\mathbf{r}), \nabla n(\mathbf{r})) . \quad (2.29)$$

As opposed to the LDA, there is a lot of freedom in the construction of GGA functionals, which is why there exists a large variety of them, each emphasizing different exact constraints, and each optimized for different kinds of systems [21–25]. Detailed comparisons of the many different functionals can be found in literature [26–28].

2.1.5 The plane-wave pseudopotential method

The numerical solution of the Kohn-Sham equations requires the choice of a basis in which the wave functions and operators are expanded, transforming the problem of solving the Schrödinger equation into an eigenvalue problem that can be solved with standard linear-algebra tools. In case of periodic boundary conditions, plane waves are a natural choice, since the potential $v_s(\mathbf{r})$ is invariant under translation by any lattice vector \mathbf{R} , and can therefore be expanded in a Fourier series

$$v_s(\mathbf{r}) = \sum_{\mathbf{G}} V_{\mathbf{G}} e^{i\mathbf{G}\cdot\mathbf{r}} , \quad (2.30)$$

where \mathbf{G} are the reciprocal lattice vectors. According to the Bloch theorem, the solutions of the Kohn-Sham equations then have the form

$$\psi_{n\mathbf{k}}(\mathbf{r}) = \sum_{\mathbf{G}} C_{\mathbf{G}}^{n\mathbf{k}} e^{i(\mathbf{G}+\mathbf{k})\cdot\mathbf{r}} , \quad (2.31)$$

which are called Bloch waves. They are labeled by the wave vector \mathbf{k} , which lies in the first Brillouin zone, and the band index n , and are orthonormal in both:

$$\langle \psi_{n\mathbf{k}} | \psi_{n'\mathbf{k}'} \rangle = \delta_{nn'} \delta_{\mathbf{k}\mathbf{k}'} . \quad (2.32)$$

Using the plane-wave representation of the kinetic energy operator,

$$T_{\mathbf{G}\mathbf{G}'}(\mathbf{k}) = \frac{1}{2}(\mathbf{k} + \mathbf{G})^2 \delta_{\mathbf{G}\mathbf{G}'} , \quad (2.33)$$

and of the potential,

$$v_{s\mathbf{G}\mathbf{G}'}(\mathbf{k}) = V_{\mathbf{G}-\mathbf{G}'} , \quad (2.34)$$

equation (2.13) in the plane-wave basis thus assumes the very simple form

$$\sum_{\mathbf{G}'} \left(\frac{1}{2}(\mathbf{k} + \mathbf{G}')^2 \delta_{\mathbf{G}\mathbf{G}'} + V_{\mathbf{G}-\mathbf{G}'} \right) C_{\mathbf{G}'}^{n\mathbf{k}} = \varepsilon_{n\mathbf{k}} C_{\mathbf{G}}^{n\mathbf{k}} . \quad (2.35)$$

\mathbf{k} is a continuous parameter, but is in practice replaced by a discrete mesh of \mathbf{k} -points sampling the first Brillouin zone. Since the accuracy of the ground-state density depends on the number N_k of \mathbf{k} -points taken into account, i.e., the resolution in \mathbf{k} -space, this number has to be found

by a convergence check, for example of the total energy. This leaves us with a discrete number of eigenvalue equations for the coefficient vectors ($C_{\mathbf{G}}^{\mathbf{m}\mathbf{k}}$), which are, however, still infinite-dimensional in the index \mathbf{G} . In order to make these eigenvalue equations finite-dimensional, the plane-wave basis is truncated at a finite \mathbf{G} , using a cut-off energy E_{cut} , such that

$$\frac{1}{2}(\mathbf{k} + \mathbf{G})^2 < E_{\text{cut}} \quad (2.36)$$

for all basis states. This is justified since the coefficients $C_{\mathbf{G}}^{\mathbf{m}\mathbf{k}}$ always vanish when $\frac{1}{2}(\mathbf{k} + \mathbf{G})^2$ becomes much larger than the considered energies $\varepsilon_{n\mathbf{k}}$, as a rearrangement of (2.35) shows:

$$C_{\mathbf{G}}^{\mathbf{m}\mathbf{k}} = \frac{\sum_{\mathbf{G}'} V_{\mathbf{G}-\mathbf{G}'} C_{\mathbf{G}'}^{\mathbf{m}\mathbf{k}}}{\varepsilon_{n\mathbf{k}} - \frac{1}{2}(\mathbf{k} + \mathbf{G})^2}. \quad (2.37)$$

E_{cut} is thus a convergence parameter that can be determined for example by converging the total energy to the desired accuracy. Increasing the basis size leads to a better approximation to the solutions of the Kohn-Sham equations and thus to the ground-state density n_0 , which, recalling the variational nature of the problem of finding n_0 , always results in a lower total energy.

How large E_{cut} has to be chosen depends basically on the shape of the potential v_s , as can be also seen from (2.37). The larger the short-wavelength contributions to the potential are, i.e., the faster varying it is, the larger are also the short-wavelength components of the wave functions, and the higher E_{cut} has to be chosen. This is problematic since the potential near the nuclei is typically strongly attracting, which means that the wave functions are strongly oscillating and a huge number of basis states would be needed to capture their relevant features. A way to avoid this, which is commonly employed in combination with a plane-wave basis, is the use of pseudopotentials. A pseudopotential v^{PP} consist of the bare nuclear potential v and an effective potential generated by the core states, and replaces the nuclear potential inside a cut-off radius r_c around the nuclei. Consequently, the core states are not explicitly taken into account in the DFT calculation any more, which means that the Kohn-Sham equations have to be solved only for the valence electrons, whereas the core electrons only enter through their contribution to the pseudopotential, which significantly reduces the computational costs. This is reasonable since the core states are essentially atomic orbitals, which are hardly effected by the surrounding atoms. The other advantage is that, due to the screening by the core electrons, the pseudopotential is much softer, i.e., varying more slowly, than the bare nuclear potential, thus allowing to use a much smaller basis set.

To be of practical use, the pseudopotential method should approximately reproduce the electronic properties of the all-electron method. Therefore, in order to construct a pseudopotential, an all-electron reference calculation is performed first for a given atomic configuration, i.e., the radial Schrödinger equation

$$\left(-\frac{1}{2} \frac{d^2}{dr^2} + \frac{l(l+1)}{2r^2} + v_s[n](r) \right) r R_{nl}(r) = \varepsilon_{nl} r R_{nl}(r) \quad (2.38)$$

is solved, yielding the radial part R_{nl} of the all-electron atomic wave functions and the all-electron energies ε_{nl} . Then, for each angular momentum l , a normalized, nodeless pseudo wave function R_l^{PP} is constructed, which fulfills

$$R_l^{\text{PP}}(r) \propto R_l(r) \quad \text{for } r \geq r_c, \quad (2.39)$$

where R_l denotes the lowest-lying valence state R_{vl} with angular momentum l , i.e., the state with the energy $\varepsilon_l = \min_v \varepsilon_{vl}$, where the index v refers to valence states. Finally, the pseudopotential is constructed such that the pseudo wave functions R_l^{PP} are eigenstates of the pseudo Hamiltonian to the eigenvalues ε_l , i.e., the energies of the all-electron calculation are reproduced. This is done by simply inverting the radial Schrödinger equation, giving

$$(v_s^{\text{PP}})_l(r) = \varepsilon_l - \frac{l(l+1)}{2r^2} + \frac{1}{2rR_l^{\text{PP}}(r)} \frac{d^2}{dr^2} (rR_l^{\text{PP}}(r)) . \quad (2.40)$$

$(v_s^{\text{PP}})_l$ are the angular components of the screened pseudopotential, from which we still have to subtract the Hartree and exchange-correlation potentials generated by the valence density n_v :

$$v_l^{\text{PP}}(r) = (v_s^{\text{PP}})_l(r) - v_H[n_v](r) - v_{\text{xc}}[n_v](r) . \quad (2.41)$$

The total pseudopotential is then obtained by summing over the angular components,

$$v^{\text{PP}}(r) = \sum_l \sum_{m=-l}^l v_l^{\text{PP}}(r) |lm\rangle \langle lm| , \quad (2.42)$$

where $|lm\rangle$ are spherical harmonics. Unlike the all-electron potential, this operator is non-local, as it acts differently on the different angular-momentum components of a wave function.

The freedom in the choice of the cut-off radius r_c and in the shape of the pseudo wave function inside r_c gives rise to a large variety of pseudopotentials, each focusing on a different property, such as softness, accuracy, and transferability. Whereas, for example, ultra-soft pseudopotentials [29, 30] allow to use a particularly small plane-wave basis, but do not reproduce the all-electron valence density outside r_c , norm-conserving pseudopotentials [31–35] do so, due to the condition

$$\int_0^{r_c} dr r^2 R_l^{\text{PP}}(r)^2 = \int_0^{r_c} dr r^2 R_l(r)^2 , \quad (2.43)$$

which turns the proportionality in (2.39) into an equality. Even though this equality is true by definition only for the eigenvalue ε_l , the norm-conserving property (2.43) actually implies that it still holds to first-order in $\varepsilon - \varepsilon_l$ [9, 36]. This ensures high transferability between different systems, such as the crystalline and amorphous phase of a material, because a small distortion of the eigenvalue spectrum due to the environment does not lead to large errors in the pseudo wave functions.

More detailed information on the different kinds of pseudopotentials, their properties, and how they are generated, can be found for example in the book of Kohanoff [9].

2.2 Quasiparticle corrections

DFT is an independent-particle theory, which means that it does not take into account many-body effects. The most striking result of this shortcoming is the severe under-estimation of the

band gap in insulators and semiconductors, for example in silicon, where the value obtained with GGA-DFT is about 0.5 eV too small. A way to overcome this problem and obtain accurate excitation spectra is to use many-body perturbation theory in the GW approximation, which eventually provides corrections to the Kohn-Sham energies, the so-called quasiparticle corrections.

2.2.1 Quasiparticles

In DFT, the Kohn-Sham energies $\varepsilon_i^{\text{KS}}$ are usually interpreted as the binding energies of single electrons, thus suggesting that the electrons are independent and the injection of an electron or hole into the system does not affect the remaining particles. As opposed to that, the concept of quasiparticles takes into account the fact that the electrons are correlated via the Coulomb interaction. Therefore, electrons repel other electrons in their vicinity and are thus surrounded by a positively charged region, called Coulomb hole. This entity of an electron and its surrounding Coulomb hole is called a quasiparticle. The injection or ejection of a quasiparticle into or from a many-body system changes the state and the energy of the whole system. Consequently, in many-body perturbation theory the single particle states $\varepsilon_i^{\text{KS}}$ are replaced by the quasiparticle energies

$$\varepsilon_i^{N-1} = E_0^N - E_i^{N-1} \quad (2.44)$$

$$\varepsilon_i^{N+1} = E_i^{N+1} - E_0^N \quad (2.45)$$

and the single particle states $\psi_i^{\text{KS}}(\mathbf{r})$ by the quasiparticle states

$$\psi_i^{N-1}(\mathbf{r}) = \langle \Psi_i^{N-1} | \hat{\psi}(\mathbf{r}) | \Psi_0^N \rangle \quad (2.46)$$

$$\psi_i^{N+1}(\mathbf{r}) = \langle \Psi_0^N | \hat{\psi}(\mathbf{r}) | \Psi_i^{N+1} \rangle, \quad (2.47)$$

where $\hat{\psi}(\mathbf{r})$ is the field operator in second-quantization formulation of quantum mechanics that describes the annihilation of an electron at position \mathbf{r} , $|\Psi_0^N\rangle$ is the N -particle ground state with energy E_0^N , and $|\Psi_i^{N\pm 1}\rangle$ are the excited $(N \pm 1)$ -particle states with energies $E_i^{N\pm 1}$, where the superscript $N + 1$ compares to an electron excitation and $N - 1$ to a hole excitation in the independent-particle picture. These superscripts will be omitted from now on in order to improve readability. Analogously to the one-particle Schrödinger equation in DFT, the quasiparticle states and energies obey a quasiparticle equation

$$h_0(\mathbf{r})\psi_i(\mathbf{r}) + \int d\mathbf{r}' \Sigma(\mathbf{r}, \mathbf{r}'; \varepsilon_i)\psi_i(\mathbf{r}') = \varepsilon_i\psi_i(\mathbf{r}), \quad (2.48)$$

where h_0 is the single-particle Hamiltonian for an electron in a mean-field system defined as

$$h_0(\mathbf{r}) = -\frac{\nabla^2}{2} + V_{\text{ext}}(\mathbf{r}) + \int d\mathbf{r}' \frac{n(\mathbf{r}')}{|\mathbf{r} - \mathbf{r}'|} \quad (2.49)$$

$$n(\mathbf{r}) = \sum_i |\psi_i(\mathbf{r})|^2 \Theta(\mu - \varepsilon_i), \quad (2.50)$$

where Θ is the Heaviside step function and μ is the chemical potential. The eigen functions $\psi_i^0(\mathbf{r})$ and energies ε_i^0 of h_0 are not the Kohn-Sham states obtained from DFT because the

mean field (2.49) consists only of the external and the Hartree potential, and does not contain the exchange-correlation term. Instead, all many-body exchange and correlation effects beyond the Hartree potential are contained in the non-local, energy-dependent self-energy operator Σ . Once this is known, the quasiparticle energies can be calculated by solving (2.48), (2.49), and (2.50) self-consistently. However, in general the self-energy is not known exactly and therefore has to be approximated. This is commonly done by means of the GW approximation, which is introduced in the next section.

2.2.2 GW approximation

The GW method provides an approximation for the many-body self-energy operator Σ . Formally, it is given by the first iteration of Hedin's equations [37], a set of integro-differential equations whose self-consistent solution, in principle, solves the many-body problem exactly, but which, in practice, cannot be solved numerically. In the GW approximation, the self energy in the time domain has the form

$$\Sigma^{GW}(\mathbf{r}, \mathbf{r}'; \tau) = iG_0(\mathbf{r}, \mathbf{r}'; \tau)W(\mathbf{r}, \mathbf{r}'; \tau + \eta) \quad (2.51)$$

($\eta > 0$ is an infinitesimal constant), which, in the energy domain, transforms to

$$\Sigma^{GW}(\mathbf{r}, \mathbf{r}'; E) = \frac{i}{2\pi} \int_{-\infty}^{\infty} dE' G_0(\mathbf{r}, \mathbf{r}'; E - E')W(\mathbf{r}, \mathbf{r}'; E')e^{-iE'\eta} . \quad (2.52)$$

Here, $G_0(E) = (E - h_0)^{-1}$ is the non-interacting one-particle Green function, which in spatial domain can be written as

$$G_0(\mathbf{r}, \mathbf{r}'; E) = \sum_i \frac{\psi_i^0(\mathbf{r})\psi_i^{0*}(\mathbf{r}')}{E - \varepsilon_i^0 + \text{sgn}(\varepsilon_i^0 - \mu)i\eta} . \quad (2.53)$$

$W(\mathbf{r}, \mathbf{r}'; E)$ is the dynamically screened interaction, which describes the effective potential at \mathbf{r} generated by a quasiparticle at \mathbf{r}' , and is therefore the summed Coulomb potential of the electron and the Coulomb hole, represented by an induced charge density $n_{\text{ind}}(\mathbf{r}'', \mathbf{r}'; E)$:

$$W(\mathbf{r}, \mathbf{r}'; E) = v_c(\mathbf{r}, \mathbf{r}') + \int d\mathbf{r}'' v_c(\mathbf{r}, \mathbf{r}'')n_{\text{ind}}(\mathbf{r}'', \mathbf{r}'; E) , \quad (2.54)$$

where $v_c(\mathbf{r}, \mathbf{r}') = 1/|\mathbf{r} - \mathbf{r}'|$ is the bare Coulomb potential. In matrix representation this reads

$$W(E) = v_c + v_cn_{\text{ind}}(E) . \quad (2.55)$$

In linear response theory, the change n_{ind} of the charge density n of a system due to the presence of a perturbative potential V is given by

$$n_{\text{ind}} = \chi V , \quad (2.56)$$

with the response function

$$\chi = \left. \frac{\delta n}{\delta V} \right|_{V=0} . \quad (2.57)$$

n_{ind} generates a Coulomb potential $v_c n_{\text{ind}}$, resulting in an effective potential

$$V_{\text{eff}} = V + v_c n_{\text{ind}} = V + v_c \chi V = \epsilon^{-1} V , \quad (2.58)$$

where

$$\epsilon^{-1} = \left. \frac{\delta V_{\text{eff}}}{\delta V} \right|_{V=0} = \mathbb{1} + v_c \chi \quad (2.59)$$

is the inverse of the microscopic dielectric matrix, relating local changes in V to local changes in V_{eff} . Defining the polarizability

$$P = \frac{\delta n}{\delta V_{\text{eff}}} \quad (2.60)$$

we can rewrite (2.57) as

$$\chi = \left. \frac{\delta n}{\delta V_{\text{eff}}} \frac{\delta V_{\text{eff}}}{\delta V} \right|_{V=0} = P \epsilon^{-1} , \quad (2.61)$$

which, combined with (2.59), gives

$$v_c P \epsilon^{-1} = \epsilon^{-1} - \mathbb{1} \quad (2.62)$$

$$\Rightarrow \epsilon = \mathbb{1} - v_c P . \quad (2.63)$$

If we identify in (2.54) the Coulomb potential of an electron at \mathbf{r}' as the perturbation V , and the screened interaction W as the resulting potential V_{eff} , we obtain

$$W(\mathbf{r}, \mathbf{r}'; E) = \int d\mathbf{r}'' \epsilon^{-1}(\mathbf{r}, \mathbf{r}''; E) v_c(\mathbf{r}'', \mathbf{r}') \quad (2.64)$$

$$\epsilon(\mathbf{r}, \mathbf{r}'; E) = \delta(\mathbf{r} - \mathbf{r}') - \int d\mathbf{r}'' v_c(\mathbf{r}, \mathbf{r}'') P(\mathbf{r}'', \mathbf{r}'; E) . \quad (2.65)$$

In the first iteration of Hedin's equations, the polarizability in the time domain is given by

$$P(\mathbf{r}, \mathbf{r}'; \tau) = -i G_0(\mathbf{r}, \mathbf{r}'; \tau) G_0(\mathbf{r}', \mathbf{r}; -\tau) , \quad (2.66)$$

which is known as the random phase approximation (RPA) [38–40]. Fourier transformation yields

$$\begin{aligned} P(\mathbf{r}, \mathbf{r}'; E) &= -\frac{i}{2\pi} \int dE' G_0(\mathbf{r}, \mathbf{r}'; E + E') G_0(\mathbf{r}', \mathbf{r}; E') \quad (2.67) \\ &= \sum_{vc} \psi_v^0(\mathbf{r}) \psi_c^{0*}(\mathbf{r}) \psi_v^{0*}(\mathbf{r}') \psi_c^0(\mathbf{r}') \left(\frac{1}{E + \varepsilon_v^0 - \varepsilon_c^0 + i\eta} - \frac{1}{E - \varepsilon_v^0 + \varepsilon_c^0 - i\eta} \right) , \quad (2.68) \end{aligned}$$

where (2.53) was used. The index v refers to valence band states and the index c to conduction band states. Equations (2.52), (2.64), (2.65), and (2.66) constitute the GW approximation, which, together with (2.48), leads to the quasiparticle states and energies. These could be used to construct a new Green function, from which a new iteration of Σ^{GW} could be calculated. This process could be repeated until convergence is reached, which is known as self-consistent GW. However, due to the high computational costs, one normally stops after one iteration. These so-called G_0W_0 or one-shot GW calculations give sufficiently accurate results already for many semiconductors and insulators, and are therefore widely used [41–44]. Any additional approximations made during the practical calculation of the quasiparticle corrections are discussed in the next section.

2.2.3 Practical calculation

In principle, in order to obtain G_0 , one first has to calculate the non-interacting single-particle states, i.e., the eigenstates of h_0 . However, in practice, GW calculations are often performed on top of a mean-field calculation, such as DFT. This means that a set of single-particle states already exists, in case of DFT in the form of the Kohn-Sham states. It is therefore more efficient to calculate the mean-field Green function G_0^{KS} from the Kohn-Sham wave functions ψ_i^{KS} and energies $\varepsilon_i^{\text{KS}}$, and use it instead of the non-interacting Green function G_0 , which are connected to each other via

$$G_0^{\text{KS}} = G_0 + G_0 V_{\text{xc}} G_0^{\text{KS}} = (G_0^{-1} - V_{\text{xc}})^{-1}, \quad (2.69)$$

where V_{xc} is the energy-independent local exchange-correlation operator from DFT. This corresponds to using $\Sigma^0 = V_{\text{xc}}$ instead of $\Sigma^0 = 0$ as a starting point for the self-energy in the GW calculation, which potentially results in a better approximation Σ^{GW} . This is true particularly if the difference $\Sigma - V_{\text{xc}}$ is small. In this case, as the comparison of the Kohn-Sham equation (2.13) and the quasiparticle equation (2.48) shows, the term $\Sigma(\varepsilon_i) - V_{\text{xc}}$ can be treated as a perturbation to the Kohn-Sham potential, and the quasiparticle states can be obtained using perturbation theory. In first order we have

$$\psi_i(\mathbf{r}) \approx \psi_i^{\text{KS}}(\mathbf{r}), \quad (2.70)$$

which turns out to be true for many systems, including those where the quasiparticle wave functions are known exactly [41, 45]. The first order energy correction is given by

$$\varepsilon_i \approx \varepsilon_i^{\text{KS}} + \langle \psi_i^{\text{KS}} | \Sigma(\varepsilon_i) - V_{\text{xc}} | \psi_i^{\text{KS}} \rangle. \quad (2.71)$$

This saves us the self-consistent solution of the quasiparticle equation, but the non-linear equation (2.71) still has to be solved self-consistently due to the term $\Sigma(\varepsilon_i)$, which requires the knowledge of the full energy dependence of the self-energy. In order to avoid this, we can use the linear expansion

$$\Sigma(\varepsilon_i) \approx \Sigma(\varepsilon_i^{\text{KS}}) + \left. \frac{d\Sigma}{dE} \right|_{\varepsilon_i^{\text{KS}}} (\varepsilon_i - \varepsilon_i^{\text{KS}}) \quad (2.72)$$

where the derivative can be evaluated numerically by calculating $\Sigma(E)$ on a grid of energy points, using the fact that Σ is often an almost linear function of E [42]. This leads to

$$\varepsilon_i \approx \varepsilon_i^{\text{KS}} + Z_i \langle \psi_i^{\text{KS}} | \Sigma(\varepsilon_i^{\text{KS}}) - V_{\text{xc}} | \psi_i^{\text{KS}} \rangle \quad (2.73)$$

with the quasiparticle renormalization factor

$$Z_i = \left(1 - \left\langle \psi_i^{\text{KS}} \left| \left. \frac{d\Sigma}{dE} \right|_{\varepsilon_i^{\text{KS}}} \right| \psi_i^{\text{KS}} \right\rangle \right)^{-1}. \quad (2.74)$$

Thanks to the linear expansion we can restrict the calculation of the self energy to a finite number of energy points. However, each of the calculations is still computationally very expensive due to the energy integral in (2.52), which requires the calculation and inversion of the dielectric matrix at a high number of energies. This can be avoided if $\varepsilon^{-1}(E)$ is instead approximated by an analytic function, a so-called plasmon-pole model, which uses the fact

that $\epsilon^{-1}(E)$ has a peaked structure. In the generalized plasmon-pole (GPP) approximation [42], ϵ^{-1} in the plane-wave basis is given by

$$\epsilon_{\mathbf{G}\mathbf{G}'}^{-1}(\mathbf{q}; E) = \delta_{\mathbf{G}\mathbf{G}'} - \frac{1}{2} \frac{\Omega_{\mathbf{G}\mathbf{G}'}^2(\mathbf{q})}{\tilde{\omega}_{\mathbf{G}\mathbf{G}'}(\mathbf{q})} \left(\frac{1}{\tilde{\omega}_{\mathbf{G}\mathbf{G}'}(\mathbf{q}) + E - i\eta} + \frac{1}{\tilde{\omega}_{\mathbf{G}\mathbf{G}'}(\mathbf{q}) - E + i\eta} \right), \quad (2.75)$$

which results in

$$\Im \epsilon_{\mathbf{G}\mathbf{G}'}^{-1}(\mathbf{q}; E) = \frac{\pi}{2} \frac{\Omega_{\mathbf{G}\mathbf{G}'}^2(\mathbf{q})}{\tilde{\omega}_{\mathbf{G}\mathbf{G}'}(\mathbf{q})} [\delta(E - \tilde{\omega}_{\mathbf{G}\mathbf{G}'}(\mathbf{q})) - \delta(E + \tilde{\omega}_{\mathbf{G}\mathbf{G}'}(\mathbf{q}))] \quad (2.76)$$

$$\Re \epsilon_{\mathbf{G}\mathbf{G}'}^{-1}(\mathbf{q}; E) = \delta_{\mathbf{G}\mathbf{G}'} + \frac{\Omega_{\mathbf{G}\mathbf{G}'}^2(\mathbf{q})}{E^2 - \tilde{\omega}_{\mathbf{G}\mathbf{G}'}^2(\mathbf{q})}. \quad (2.77)$$

The poles $\tilde{\omega}_{\mathbf{G}\mathbf{G}'}(\mathbf{q})$ are obtained from the requirement that the model reproduces $\epsilon^{-1}(E=0)$ exactly:

$$\tilde{\omega}_{\mathbf{G}\mathbf{G}'}^2(\mathbf{q}) = \frac{\Omega_{\mathbf{G}\mathbf{G}'}^2(\mathbf{q})}{\delta_{\mathbf{G}\mathbf{G}'} - \epsilon_{\mathbf{G}\mathbf{G}'}^{-1}(\mathbf{q}; 0)}. \quad (2.78)$$

$\Omega_{\mathbf{G}\mathbf{G}'}(\mathbf{q})$ is called the effective bare plasma frequency and is obtained from the generalized f -sum rule [42], relating the imaginary part of ϵ^{-1} to the charge density n :

$$\Omega_{\mathbf{G}\mathbf{G}'}^2(\mathbf{q}) = \omega_p^2 \frac{(\mathbf{q} + \mathbf{G}) \cdot (\mathbf{q} + \mathbf{G}')}{|\mathbf{q} + \mathbf{G}|^2} \frac{n(\mathbf{G} - \mathbf{G}')}{n(\mathbf{0})}, \quad (2.79)$$

where $\omega_p = 4\pi n(\mathbf{0})$ is the plasma frequency. The GPP approximation allows the analytic evaluation of the convolution in (2.52), and requires the calculation and inversion of the dielectric matrix only at $E=0$, while still taking into account the effects of dynamical screening. This yields an accuracy similar to a full-frequency calculation for many semiconductors, including c-Si [42, 44], while significantly reducing the computational effort.

Both the calculation of the static dielectric matrix and of the self energy require a summation over unoccupied bands, which in practice has to be truncated. The same holds for the plane-wave basis, for which, analogously to the procedure in DFT, a cut-off energy E_{cut} is used. $N_{\text{bands}}^\epsilon$, N_{bands}^Σ , and E_{cut} are convergence parameters that have to be chosen by checking the convergence of the quasiparticle corrections with respect to all three of them simultaneously.

2.2.4 Scissors shift

In many materials the main effect of the quasiparticle corrections consists in a widening of the band gap by rigidly shifting the single-particle energies [46, 47]. The quasiparticle energies can therefore often be obtained from the Kohn-Sham energies approximately by a linear shift of both the valence and the conduction band,

$$\epsilon_{v/c} = \epsilon_{v/c}^{\text{KS}} + a_{v/c} \left(\epsilon_{v/c}^{\text{KS}} - E_{v/c}^0 \right) + E_{v/c}^{\text{s}}, \quad (2.80)$$

which is known as a scissors shift. $E_{v/c}^0$ is a reference energy, which can for example be the valence and conduction band edge, or the Fermi level. The shifting parameters $a_{v/c}$ and $E_{v/c}^{\text{s}}$ can either be obtained from the experimental band structure, or from a previous GW calculation.

2.3 Characterization methods

In order to characterize the generated configurations and compare them to real materials, we analyze their structural, electronic, and optical properties. The structural characterization answers the question how the atoms are distributed in relation to each other, measured by the radial pair correlation function, and how they are bonding. The electronic characterization aims on the one hand at extracting macroscopic quantities such as the electronic band gap or mobility gap, respectively, but on the other hand also at analyzing the contribution of individual states, in particular those of localized nature. The optical characterization answers the question how different kinds of states couple optically and thus contribute to absorption, and thereby yields a measure for the optical gap.

2.3.1 Radial pair correlation function

The radial pair correlation function $g_{\alpha\beta}(r)$ is a measure for the probability of finding an atom of species α at a distance r from an atom of species β . It is defined as

$$g_{\alpha\beta}(r) = \frac{V}{4\pi r^2 N_\alpha N_\beta} \sum_{I=1}^{N_\alpha} \sum_{J=1}^{N_\beta} \delta(r - |\mathbf{R}_I - \mathbf{R}_J|), \quad (2.81)$$

where V is the super-cell volume, $N_{\alpha/\beta}$ are the numbers of atoms of the respective atomic species in the super cell, and $\{\mathbf{R}_I\}$ are the atomic positions. If $\alpha = \beta$, this becomes

$$g_{\alpha\alpha}(r) = \frac{V}{4\pi r^2 N_\alpha (N_\alpha - 1)} \sum_{\substack{I,J=1 \\ I \neq J}}^{N_\alpha} \delta(r - |\mathbf{R}_I - \mathbf{R}_J|). \quad (2.82)$$

In a crystalline material, $g(r)$ shows sharp peaks at the equilibrium atomic distances, whereas with increasing disorder the peaks smear out. The radial pair correlation function gives a good first impression of how well a model configuration describes a real amorphous material, because it captures both the average inter-atomic distances and the degree of disorder.

2.3.2 Bonding and the ELF

Apart from the geometrical properties of an atomic structure, i.e., those that can be directly extracted from the atomic positions, the other important microscopic structural property is the coordination number, i.e., the number of bonds that each atom forms. In order to calculate this number, a criterion for the identification of bonds is required. We will introduce such a criterion here, which is based on the electron localization function (ELF), and compare it to an often-used geometrical criterion.

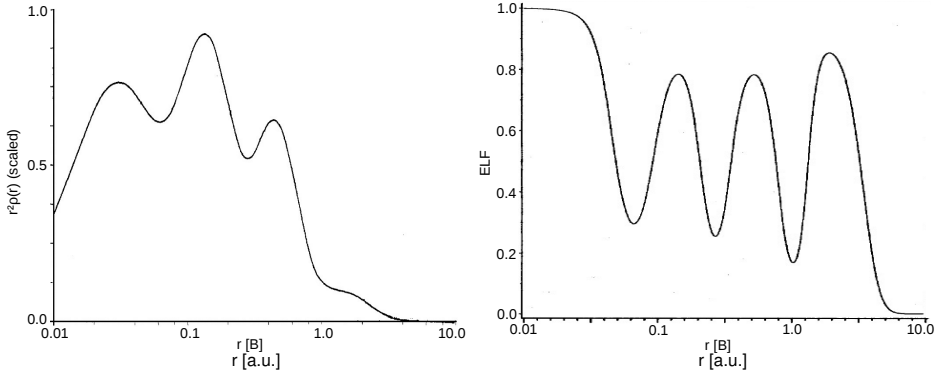


Figure 2.1: Comparison of radial electron density (left) [49] and ELF (right) [48] for the Krypton atom. As opposed to the electron density, the ELF clearly distinguishes all four shells.

ELF

The electron localization function $\text{ELF}(\mathbf{r})$ provides a measure for how strongly electrons are localized in a point \mathbf{r} . It was introduced in 1990 by Becke and Edgecomb as a means of visualizing atomic shells, bonds, and ion pairs in the form of a spatial function [48], for which the charge density alone is not sufficient, as the example of Krypton illustrates (Fig. 2.1). Whereas the ELF clearly brings out all four orbitals as distinct peaks, the maxima of the radial electron density are much less pronounced, and only three shells can be identified.

The definition of the ELF is based on the Pauli principle, which results in a repulsion of electrons with identical spin σ . To measure the localization of an electron at point \mathbf{r} we can therefore use the conditional probability of a second electron being located at a point \mathbf{r}' near \mathbf{r} [50]:

$$P_{\text{cond}}^{\sigma\sigma}(\mathbf{r}, \mathbf{r}') = n_{\sigma}(\mathbf{r}') - \frac{|\rho_{\sigma\sigma}(\mathbf{r}, \mathbf{r}')|^2}{n_{\sigma}(\mathbf{r})}, \quad (2.83)$$

where $n_{\sigma}(\mathbf{r})$ is the spin-resolved electron density and

$$\rho_{\sigma\sigma}(\mathbf{r}, \mathbf{r}') = \sum_{i:\sigma_i=\sigma} \psi_i^*(\mathbf{r})\psi_i(\mathbf{r}') \quad (2.84)$$

is the spin-resolved one-particle density matrix for a system of independent particles with one-particle wave functions ψ_i . In order to obtain a measure for the localization that only depends on \mathbf{r} , we consider the average conditional probability $P_{\text{cond}}^{\sigma\sigma}(\mathbf{r}, s)$ on a sphere with radius s centered about \mathbf{r} . For small s this is to second order given by [51]

$$P_{\text{cond}}^{\sigma\sigma}(\mathbf{r}, s) = \frac{1}{3} \left(\sum_{i:\sigma_i=\sigma} |\nabla\Phi_i(\mathbf{r})|^2 - \frac{1}{4} \frac{|\nabla n_{\sigma}(\mathbf{r})|^2}{n_{\sigma}(\mathbf{r})} \right) s^2. \quad (2.85)$$

Localization at \mathbf{r} is obviously the stronger, the smaller $P_{\text{cond}}^{\sigma\sigma}(\mathbf{r}, s)$ is for any s . The quantity

of interest, which only depends on \mathbf{r} , is therefore the term

$$D_\sigma(\mathbf{r}) = \sum_{i:\sigma_i=\sigma} |\nabla\Phi_i(\mathbf{r})|^2 - \frac{1}{4} \frac{|\nabla n_\sigma(\mathbf{r})|^2}{n_\sigma(\mathbf{r})}. \quad (2.86)$$

In a semiconductor, where every state is occupied by one spin-up and one spin-down electron, we have

$$n_\sigma(\mathbf{r}) = \frac{1}{2}n(\mathbf{r}) \quad (2.87)$$

and

$$\sum_{i:\sigma_i=\sigma} |\nabla\Phi_i(\mathbf{r})|^2 = \frac{1}{2} \sum_i^N |\nabla\Phi_i(\mathbf{r})|^2 \equiv \tau(\mathbf{r}), \quad (2.88)$$

where $\tau(\mathbf{r})$ is the kinetic energy density. Using this we can write (2.86) in a spin-independent form as

$$D(\mathbf{r}) = \tau(\mathbf{r}) - \frac{1}{8} \frac{|\nabla n(\mathbf{r})|^2}{n(\mathbf{r})}. \quad (2.89)$$

In order to obtain a normalized quantity, which is the bigger the stronger the localization is, we finally define the electron localization function

$$\text{ELF}(\mathbf{r}) = \frac{1}{1 + \left(\frac{D(\mathbf{r})}{D_0(\mathbf{r})}\right)^2}, \quad (2.90)$$

where

$$D_0(\mathbf{r}) = \frac{3}{10} (3\pi^2)^{2/3} n^{5/3}(\mathbf{r}) \quad (2.91)$$

is the value of D for the homogeneous electron gas. The ELF assumes the value 1 in points of maximum localization, and vanishes where no charge is localized.

Bonding

As explained before, the ELF indicates where valence charge is localized within the structure. It can therefore be used to identify covalent and dangling bonds based on the fact that a covalent bond is formed by overlapping atomic orbitals, which results in an accumulation of charge between the bonded atoms. This accumulation shows as a broad maximum in the ELF along the bonding axis for non-polar covalent semiconductors such as Silicon and Germanium, for which it reaches a value of 0.95 and 0.9, respectively (Fig. 2.2) [52]. As the bond breaks, charge is no longer localized between the atoms but in atomic orbitals instead, which shows as peaks in the ELF near the atomic positions, forming a minimum in the center (Fig. 2.3(a) - dotted line). The same applies to Si-H bonds despite the different shape of the ELF displayed there (Fig. 2.3(a) - dash-dotted line), which arises from neglecting core electrons of Si that causes the ELF to drop to zero near the Si, but not near the H atoms.

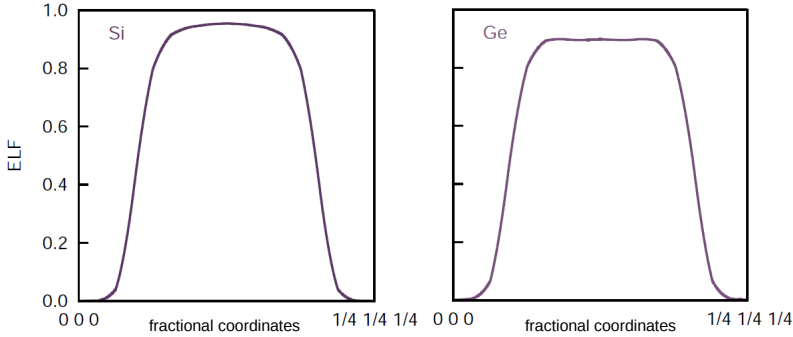


Figure 2.2: ELF along the bonding axis for crystalline Silicon (left) and Germanium (right) [52]. The bond is visible in form of a broad maximum.

The change in the behavior of the ELF along the axes between neighboring atoms upon bond breaking can be used to distinguish whether a bond exists or not. As the different shape also goes along with a distinctly different value of the ELF in the center between the atoms, we can alternatively use this value as a simple criterion for identifying a dangling bond. Even though the values of the maxima and minima vary in amorphous semiconductors, a value of 0.8 has been found reasonable to separate the maxima from the minima for all analyzed Si-Si and Si-H bonds in a-Si:H, and is therefore used as a threshold throughout this work.

Even though the method introduced here still requires the choice of a threshold value to decide whether a bond exists or not, and some uncertainty in the detection of bonds therefore remains, it is physically more meaningful than the standard method using cut-off radii, as it accounts for the actual process of covalent bonding. In particular it respects the fact that atoms can form only a limited number of bonds irrespective of the number of neighboring atoms, meaning that even atoms close to each other do not necessarily bond. On the other hand, in the a-Si:H structures investigated, we found that in rare cases even atoms at a distance of up to 2.95 Å can form a bond. Consequently, the use of cut-off radii, which are commonly chosen between 2.75 and 2.85 Å for Si-Si bonds, and between 1.70 and 1.78 Å for Si-H bonds [6, 53, 54], will result in some bonds being erroneously detected and some being erroneously disregarded. This is illustrated in Fig. 2.3(b), where, based on analyzing all Si-Si pairs (41190) and all Si-H pairs (1102) in all configurations investigated throughout our work, the statistical probability of two atoms forming a bond is shown as a function of their distance. The curve described by the data points is not a step function, which is the assumption behind the use of cut-off radii, but exhibits a significant broadening. Fitting a Fermi function $1/[1 + \exp((x - x_0)/\delta)]$ to both data sets results in $x_0 = 2.65$ Å and $\delta = 0.07$ Å for Si-Si bonds and $x_0 = 1.74$ Å and $\delta = 0.03$ Å for Si-H bonds.

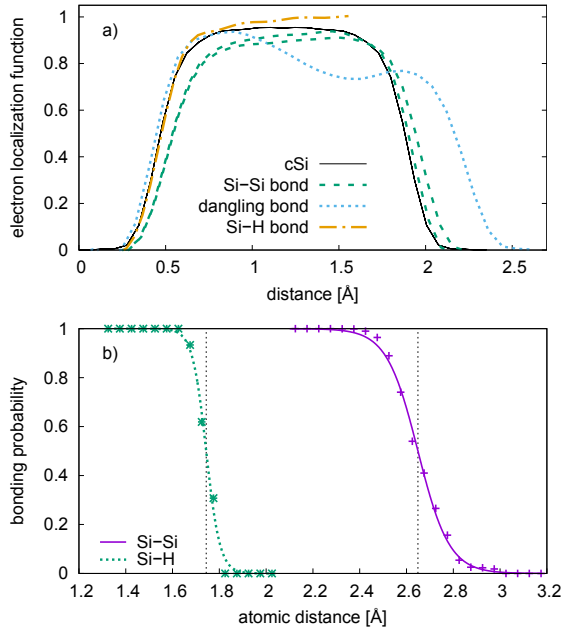


Figure 2.3: (a) Analysis of bonds by means of the Electron localization function (ELF). This example shows the ELF along the bonding axes for a three-fold bonded Si atom in a-Si:H. A maximum in the center between two atoms exceeding a threshold value of 0.8 indicates a bond. A minimum indicates a broken bond. One can distinguish two Si-Si bonds (dashed), one dangling bond (dotted), and one Si-H bond (dash-dotted). The ELF in c-Si is shown as a reference (solid). (b) Statistical probability of two atoms being bonded (according to the ELF criterion) as a function of their distance. The data points result from all configurations investigated throughout our work. The solid and dotted line, respectively, are Fermi functions fitted to the data points. The vertical dotted lines mark the distances where 50% of the Si-Si and Si-H pairs, respectively, form a bond. [7]

2.3.3 Density of states

In crystalline semiconductors the electronic band structure is the primary tool in electronic characterization, as it largely determines the macroscopic electronic properties of the material. In amorphous semiconductors, where the definition of a band structure becomes meaningless due to the absence of periodicity, this role is taken by the electronic density of states (DOS). It is defined as

$$\rho(E) = \sum_i \delta(E - \varepsilon_i) , \quad (2.92)$$

where ε_i are the single electron (Kohn-Sham) energies, and yields the number of electrons in the system with a given energy E . Additional information on the origin of electronic features can be obtained by spatially resolving the DOS, which defines the local density of states (LDOS)

$$\rho(E, \mathbf{r}) = \sum_i |\psi_i(\mathbf{r})|^2 \delta(E - \varepsilon_i) , \quad (2.93)$$

with the Kohn-Sham orbitals ψ_i . If we are interested particularly in the progression of the DOS along one spatial direction, say z (as it is the case for the a-Si:H/c-Si interface), we use the layer-resolved DOS instead, which is obtained by simply integrating the LDOS over layers perpendicular to the direction of interest:

$$\rho_z(E, z) = \int_{L_x, L_y} dx dy \rho(E, \mathbf{r}) . \quad (2.94)$$

For the case that we are not interested in the full DOS, but only in the DOS generated by a subset P of all Kohn-Sham states (e.g., only localized states), we define the partial density of states (PDOS)

$$\rho_P(E) = \sum_{i \in P} \delta(E - \varepsilon_i) . \quad (2.95)$$

2.3.4 Electronic localization

Motivation and definition of the spread

In case of a finite system, a natural and intuitive way of measuring the localization of a wave function ψ is to calculate the variance σ^2 of the probability distribution $|\psi(\mathbf{r})|^2$,

$$\sigma^2 = \langle \mathbf{r}^2 \rangle - \langle \mathbf{r} \rangle^2 = \int_V d\mathbf{r} |\psi(\mathbf{r})|^2 \mathbf{r}^2 - \left(\int_V d\mathbf{r} |\psi(\mathbf{r})|^2 \mathbf{r} \right)^2 , \quad (2.96)$$

where $|\psi(\mathbf{r})|^2$ is normalized in the integration volume V , i.e., $\psi(\mathbf{r})$ goes to zero at the boundaries of V . If periodic boundary conditions are imposed, the integration volume V has to be replaced

by the super-cell volume Ω , which is however not uniquely defined, meaning that σ^2 depends in general on the choice of the integration boundaries. We will therefore write $\sigma^2[\Omega]$ in the following to account for that dependence. In the case that the periodic images of the system are isolated from each other (for example by a vacuum layer), such that $\psi(\mathbf{r})$ vanishes in between, the only physically meaningful way of choosing the integration volume is such that $\psi(\mathbf{r}) = 0$ at the integration boundaries, which produces the same result for σ^2 as if a finite system was considered. If the system is truly periodic on the other hand, there exists no unique choice for Ω , and we have to define our measure of localization more precisely.

In order to do this we consider for simplicity a 1D system with periodicity a . Then the integration volume Ω is the interval $[x_0, x_0 + a]$, defined by the parameter x_0 , and the variance reads

$$\sigma^2[x_0] = \int_{x_0}^{x_0+a} dx |\psi(x)|^2 x^2 - \left(\int_{x_0}^{x_0+a} dx |\psi(x)|^2 x \right)^2. \quad (2.97)$$

If ψ is maximally delocalized, i.e., a plane wave, then $|\psi(\mathbf{r})|^2 = 1/a$ and $\sigma^2[x_0] = a^2/12$ irrespective of the choice of x_0 . In order for our definition of localization to be meaningful, every other ψ that is not a plane wave, and hence is localized to some extent, must result in a lower value of $\sigma^2[x_0]$. This will be our first assumption. The second assumption is that the integration volume should be centered about the center of mass $\langle \mathbf{r} \rangle$ of $|\psi(\mathbf{r})|^2$, i.e., in the 1D case,

$$x_0 + \frac{a}{2} = \langle x \rangle, \quad (2.98)$$

which agrees with the intuitive way of defining the cell boundaries in case of a localized wave function (see Fig. 2.4). As $\langle x \rangle$ depends however itself on x_0 , this does not define x_0 uniquely. In fact, each value of x_0 fulfilling (2.98), corresponds to a minimum or maximum of $\sigma^2[x_0]$, as can be seen by differentiating σ^2 with respect to x_0 :

$$\frac{d\sigma^2}{dx_0} = \frac{d}{dx_0} \left[\int_{x_0}^{x_0+a} dx |\psi(x)|^2 x^2 - \left(\int_{x_0}^{x_0+a} dx |\psi(x)|^2 x \right)^2 \right] \quad (2.99)$$

$$= |\psi(x_0)|^2 ((x_0 + a)^2 - x_0^2) - 2 \left(\int_{x_0}^{x_0+a} dx |\psi(x)|^2 x \right) |\psi(x_0)|^2 a \quad (2.100)$$

$$= |\psi(x_0)|^2 (a^2 + 2x_0 a) - 2 \langle x \rangle |\psi(x_0)|^2 a \quad (2.101)$$

$$= 2a |\psi(x_0)|^2 \left(\frac{a}{2} + x_0 - \langle x \rangle \right). \quad (2.102)$$

Inserting (2.98) yields $d\sigma^2/dx_0 = 0$. $\sigma^2[x_0]$ can have an arbitrary number of local maxima and minima, but, since it is periodic, must have at least one of each (unless it is constant), i.e., at least two values of x_0 fulfilling (2.98). However, only the absolute minimum is guaranteed to fulfill the condition that $\sigma^2 \leq a^2/12$, as the following considerations show. We use (2.98) to

rewrite the variance as

$$\sigma^2[x_0] = \int_{x_0}^{x_0+a} dx |\psi(x)|^2 (x - \langle x \rangle)^2 \quad (2.103)$$

$$= \int_{x_0}^{x_0+a} dx |\psi(x)|^2 \left(x - x_0 - \frac{a}{2}\right)^2 \quad (2.104)$$

$$= \int_{-a/2}^{a/2} dx \left| \psi\left(x + x_0 + \frac{a}{2}\right) \right|^2 x^2. \quad (2.105)$$

By integrating over x_0 we obtain the average value $\bar{\sigma}^2$:

$$\bar{\sigma}^2 = \frac{1}{a} \int_{-a/2}^{a/2} dx_0 \sigma^2[x_0] = \frac{1}{a} \int_{-a/2}^{a/2} dx_0 \int_{-a/2}^{a/2} dx \left| \psi\left(x + x_0 + \frac{a}{2}\right) \right|^2 x^2 \quad (2.106)$$

$$= \frac{1}{a} \int_{-a/2}^{a/2} dx \int_{-a/2}^{a/2} dx_0 \left| \psi\left(x + x_0 + \frac{a}{2}\right) \right|^2 x^2 \quad (2.107)$$

$$= \frac{1}{a} \int_{-a/2}^{a/2} dx x^2 \quad (2.108)$$

$$= \frac{a^2}{12}, \quad (2.109)$$

where we used the fact that $|\psi|^2$ is normalized. The absolute minimum of σ^2 must be smaller than the average, which however does not hold for the other local minima. From this result it follows that, in order to fulfill the condition $\sigma^2[x_0] \leq a^2/12$, x_0 must be chosen such that $\sigma^2[x_0]$ is minimized.

This result can be directly transferred to the 3D case of a tetragonal super cell with lattice constants a_1 , a_2 , and a_3 , using the fact that σ^2 can be separated into its cartesian components:

$$\sigma^2 = \sigma_x^2 + \sigma_y^2 + \sigma_z^2, \quad (2.110)$$

with

$$\sigma_x^2[\Omega] = \int_{\Omega} d\mathbf{r} |\psi(\mathbf{r})|^2 x^2 - \left(\int_{\Omega} d\mathbf{r} |\psi(\mathbf{r})|^2 x \right)^2 \quad (2.111)$$

and equivalently for σ_y and σ_z . By defining the integrated probability density

$$|\psi|_x^2(x) = \int_0^{a_2} dy \int_0^{a_3} dz |\psi(\mathbf{r})|^2 \quad (2.112)$$

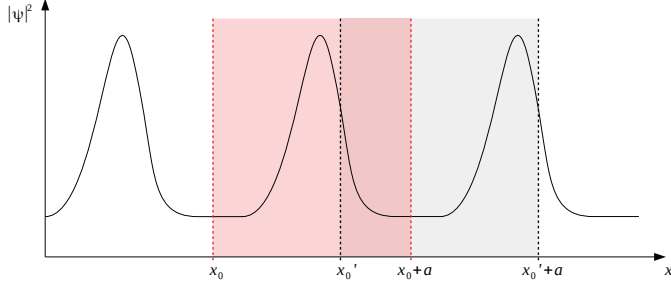


Figure 2.4: Definition of super cell in a 1D example. Both x_0 (red) and x'_0 (gray) are possible choices of the super cell boundaries. However, the intuitively reasonable choice is the red area, as it contains the peak as a whole, whereas in the gray area the peak is split in two parts. This intuitive definition of the super cell is equivalent to minimizing the variance of $|\psi|^2$ with respect to x_0 .

we can express this as

$$\sigma_x^2[x_0] = \int_{x_0}^{x_0+a_1} dx |\psi|_x^2(x) x^2 - \left(\int_{x_0}^{x_0+a_1} dx |\psi|_x^2(x) x \right)^2 \quad (2.113)$$

arriving at the same form as (2.97). This means that we can calculate the localization of a wave function in all three directions individually by minimizing the respective variance. We therefore define as a quantitative measure for the localization of a wave function in a periodic system the spread in x -direction

$$S_x = \min_{x_0} \sqrt{12 \sigma_x^2[x_0]} = \min_{x_0} \sqrt{12 \int_{-a_1/2}^{a_1/2} dx |\psi|_x^2 \left(x + x_0 + \frac{a_1}{2} \right) x^2}, \quad (2.114)$$

where the form (2.105) was used. This definition does not only yield the localization, but also a value for the mean position $\langle x \rangle = x_0 + a_1/2$ of an electron. The factor $\sqrt{12}$ restricts S_x to the interval $[0, a_1]$, i.e., $S_x = 0$ for a maximally localized ψ (a delta function) and $S_x = a_1$ for a maximally delocalized ψ (a plane wave). S_y and S_z are calculated analogously and the total spread is given by

$$S = \sqrt{\frac{1}{3} (S_x^2 + S_y^2 + S_z^2)}, \quad (2.115)$$

such that $0 \leq S \leq a$ for a cubic super cell with lattice constant a .

Calculation in reciprocal space

In plane-wave expansion the lattice periodic part of the Bloch function is given by

$$\psi(\mathbf{r}) = \frac{1}{\sqrt{\Omega}} \sum_{\mathbf{G}} C_{\mathbf{G}} e^{i\mathbf{G}\cdot\mathbf{r}} . \quad (2.116)$$

Integrating over the yz -plane yields

$$|\psi|_x^2(x) = \frac{1}{\Omega} \int_0^{a_2} dy \int_0^{a_3} dz \sum_{\mathbf{G}} e^{i\mathbf{G}\cdot\mathbf{r}} \sum_{\mathbf{G}'} C_{\mathbf{G}'}^* C_{\mathbf{G}+\mathbf{G}'} \quad (2.117)$$

$$= \frac{1}{a_1} \sum_{G_x} e^{iG_x x} \sum_{\mathbf{G}'} C_{\mathbf{G}'}^* C_{G_x \mathbf{e}_x + \mathbf{G}'} \quad (2.118)$$

and the variance in x -direction using (2.105) becomes

$$\sigma_x^2[x_0] = \frac{1}{a_1} \sum_{G_x} \int_{-a_1/2}^{a_1/2} dx \exp\left(iG_x\left(x + x_0 + \frac{a_1}{2}\right)\right) x^2 \sum_{\mathbf{G}'} C_{\mathbf{G}'}^* C_{G_x \mathbf{e}_x + \mathbf{G}'} \quad (2.119)$$

$$= \frac{1}{a_1} \left(\frac{a_1^3}{12} + \sum_{G_x \neq 0} \exp\left(iG_x\left(x_0 + \frac{a_1}{2}\right)\right) \frac{2a_1}{G_x^2} \exp\left(iG_x \frac{a_1}{2}\right) \sum_{\mathbf{G}'} C_{\mathbf{G}'}^* C_{G_x \mathbf{e}_x + \mathbf{G}'} \right) \quad (2.120)$$

$$= \frac{a_1^2}{12} + 2 \sum_{G_x \neq 0} \frac{\exp(iG_x x_0)}{G_x^2} \sum_{\mathbf{G}'} C_{\mathbf{G}'}^* C_{G_x \mathbf{e}_x + \mathbf{G}'} . \quad (2.121)$$

The spread is therefore given by

$$S_x = \min_{x_0} \sqrt{a_1^2 + 24 \sum_{G_x \neq 0} \frac{\exp(iG_x x_0)}{G_x^2} \sum_{\mathbf{G}'} C_{\mathbf{G}'}^* C_{G_x \mathbf{e}_x + \mathbf{G}'} } = \sqrt{a_1^2 - S_x^2} . \quad (2.122)$$

Since we established before that $S_x \in [0, a_1]$, the second term in the radicand must be negative and can therefore be written as

$$S_x^2 = -24 \sum_{G_x \neq 0} \frac{\exp(iG_x x_0)}{G_x^2} \sum_{\mathbf{G}'} C_{\mathbf{G}'}^* C_{G_x \mathbf{e}_x + \mathbf{G}'} , \quad (2.123)$$

with $S_x^0 \in [0, a_1]$.

Discussion

Whereas the inverse participation ratio (IPR) [55], which is commonly used as a measure of localization [56], uses projections onto atomic orbitals and therefore depends on the choice of these orbitals, the spread is uniquely defined. Also, as opposed to the IPR, the spread has the advantage that it can be decomposed in its x -, y -, and z -component, thus allowing to measure

the localization only in the direction of interest. Furthermore, this method allows us not only to identify localized states, but also to locate them in real space, which is extremely helpful for the characterization of the states in a composite structure such as the a-Si:H/c-Si interface. The interpretation of the mean position $\langle \mathbf{r} \rangle$ as the position where an electron is localized has to be handled with care however, as it does not make sense for delocalized states, and can be misleading in the case of very asymmetrically localized wave functions.

2.3.5 Mobility gap

The mobility gap of an amorphous semiconductor is defined as the energy region between the valence and the conduction band where no band transport occurs due to the absence of band states. It can therefore theoretically be determined as the energy range where all states are localized [57]. However, to do this in practice, we need to define a criterion for distinguishing localized from extended states. For this purpose we use the measure of localization defined above, the spread S , where, depending on whether our system is isotropic or whether we are interested in transport only in a select direction, we choose either the total spread or the respective spatial component. We then have to define a threshold for S that separates localized and extended states. This is done by using the fact that sufficiently far away from the Fermi energy almost all states are delocalized, and, ideally, have values of S that lie in a narrow band, as it is the case in the example in Fig. 2.5. From the figure, the lower edge of this band is determined to be roughly at 20.7 Å, which can then be used as a threshold value S_t . In the next step the energy range around the Fermi level where no states with $S > S_t$ exist can be determined. In the present example (Fig. 2.5) this leads to a value of $E_g^{\text{mob}} = 0.92$ eV.

The described procedure provides an easy way to obtain the mobility gap from the localization, but holds a number of problems:

1. The spread band in which states far away from the Fermi level are found does not have a sharp edge, which means that there is a certain ambiguity in the choice of the threshold S_t .
2. A small variation of S_t can trigger a large variation of E_g^{mob} .
3. E_g^{mob} is very sensitive to the behavior of single states, i.e., small changes in the energy or localization of a state can have a large impact on E_g^{mob} .

The first issue can be addressed by studying the distribution of the valence band states in S (Fig. 2.6), which reveals a kind of Gaussian shape with a low-spread tail. This representation allows a somewhat more accurate determination of the delocalization edge than Fig. 2.5, but still leaves an uncertainty of at least 0.1 Å.

The second and third problem occur due to the fact that with the given method the mobility edges are determined by isolated states with high spread, as Fig. 2.5 shows. If instead the mobility edges are defined as the energies where a high number of states start exceeding S_t , one obtains a significantly higher value for E_g^{mob} , which also will be less sensitive both to S_t

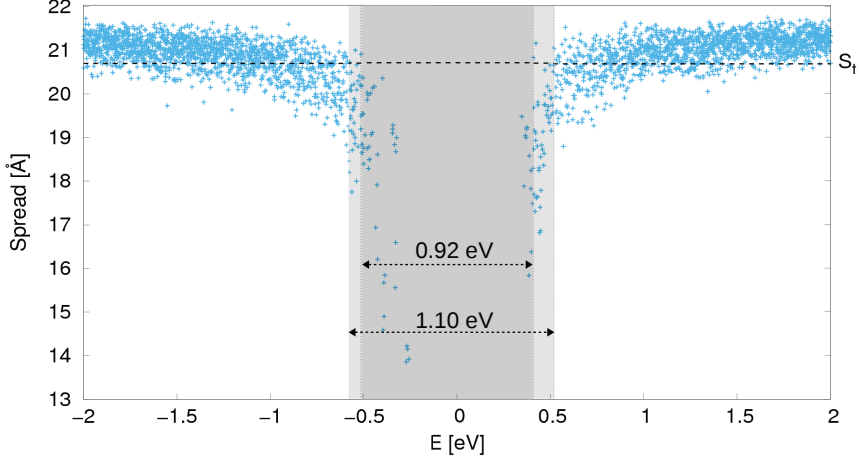


Figure 2.5: Determination of mobility gap in an a-Si:H configuration with lattice constant $a = 22.035 \text{ \AA}$. Each point represents one state. Far away from the Fermi level (0 eV) most states have a spread that lies in a narrow band close to a . The horizontal line at $S_t = 20.7 \text{ \AA}$ marks the approximate edge of this band, which separates localized from extended states. Defining the mobility gap as the range where no extended states exist at all (dark grey), gives $E_g^{\text{mob}} = 0.92 \text{ eV}$. Defining it instead as the range where no significant density of extended states exists (light grey), gives $E_g^{\text{mob}} \approx 1.10 \text{ eV}$.

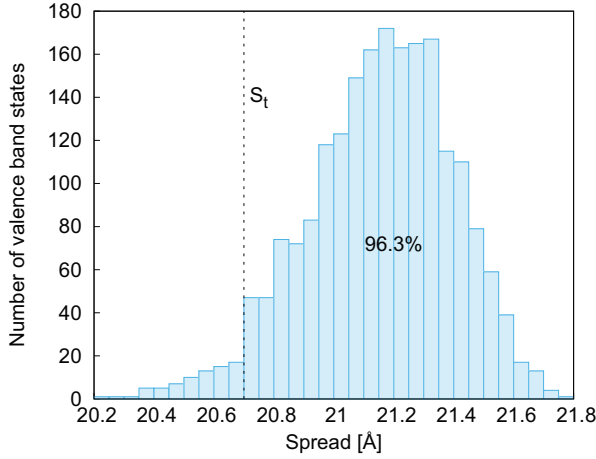


Figure 2.6: Histogram of spread for valence band states far away ($> 2 \text{ eV}$) from the Fermi level. The histogram has a Gaussian-like part and a low-spread tail, which are roughly separated by $S_t = 20.7 \text{ eV}$ (vertical line). At this value more than 95% of the states have a spread $S > S_t$. This analysis allows a more precise determination of the delocalization edge seen in Fig. 2.5.

and to single states. From the light grey area in Fig. 2.5 this value is determined to 1.10 eV, which appears to be a better approximation of the mobility gap than the dark grey area.

In order to formalize this modified definition of the mobility edges and obtain E_g^{mob} mathematically rather than visually, we first calculate the partial density of states (PDOS) of all states with $S > S_t$, and then determine the mobility edges as the energies where the PDOS reaches a threshold value D_t . This procedure requires the choice of a broadening parameter Γ used in the calculation of the PDOS, and of the threshold D_t . The advantage of introducing a broadening is to reduce the sensitivity to single states, and to smoothen the dependence of E_g^{mob} on S_t . On the other hand, it comes with the drawback of having to deal with two additional parameters.

In order to find the best choice of parameters, we use our example configuration to calculate E_g^{mob} as a function of S_t for all pairs of parameters from sets $\{\Gamma\}$ and $\{D_t\}$. Thereby, Γ is restricted to values below 0.1 eV, such that the broadening does not exceed the target accuracy, and D_t is limited to 0.02 eV^{-1} per electron, as higher values would result in unphysically high values of E_g^{mob} . The goal is to choose parameters such that E_g becomes a smooth function of S_t and D_t , while at the same time the dependence on D_t is minimized, and such that $E_g^{\text{mob}}(S_t = 20.7 \text{ \AA}) \lesssim 1.1 \text{ eV}$, in agreement with Fig. 2.5. As the results in Fig. 2.7 show, higher values of both Γ and D_t lead to a smoother dependence on S_t , whereas smaller values of Γ decrease the dependence dE_g^{mob}/dD_t . The broadening should therefore be chosen as small as possible while still obtaining a smooth curve. We can measure the smoothness by fitting E_g^{mob} vs S_t with an exponential function, which is a good approximation to the data points for sufficiently high Γ and D_t , as Fig. 2.8(a) shows. The root mean square of the residuals then indicates how much the data points deviate from a smooth fit. This is plotted in Fig. 2.8(b). The minimum Γ for which a good fit is obtained is $\Gamma = 0.06 \text{ eV}$ with $D_t = 0.02 \text{ eV}^{-1}$. These parameters however result in a value of $E_g^{\text{mob}} > 1.1 \text{ eV}$ and are therefore discarded. The same holds for $\Gamma = 0.07 \text{ eV}$. The smallest broadening that gives a satisfactory smooth curve and a physically reasonable value for E_g^{mob} is $\Gamma = 0.08 \text{ eV}$ together with $D_t \geq 0.014 \text{ eV}^{-1}$. The value for E_g^{mob} closest to 1.1 eV is reached at $D_t = 0.018 \text{ eV}^{-1}$, resulting in $E_g^{\text{mob}}(S_t = 20.7 \text{ \AA}) = 1.09 \text{ eV}$ (Fig. 2.9). We will therefore use a broadening of $\Gamma = 0.08 \text{ eV}$ and a threshold for the PDOS of $D_t = 0.018 \text{ eV}^{-1}$ per electron for determining the mobility gap throughout this work.

2.3.6 Optical characterization

Absorption

The propagation of an electromagnetic wave of energy E in a non-magnetic isotropic material is described by

$$\mathbf{E}(x, t) = \mathbf{E}_0 \exp\left(iE\left(\frac{x}{c} - t\right)\right), \quad (2.124)$$

with the phase velocity

$$c = \frac{c_0}{\sqrt{\epsilon}} \equiv \frac{c_0}{n}, \quad (2.125)$$

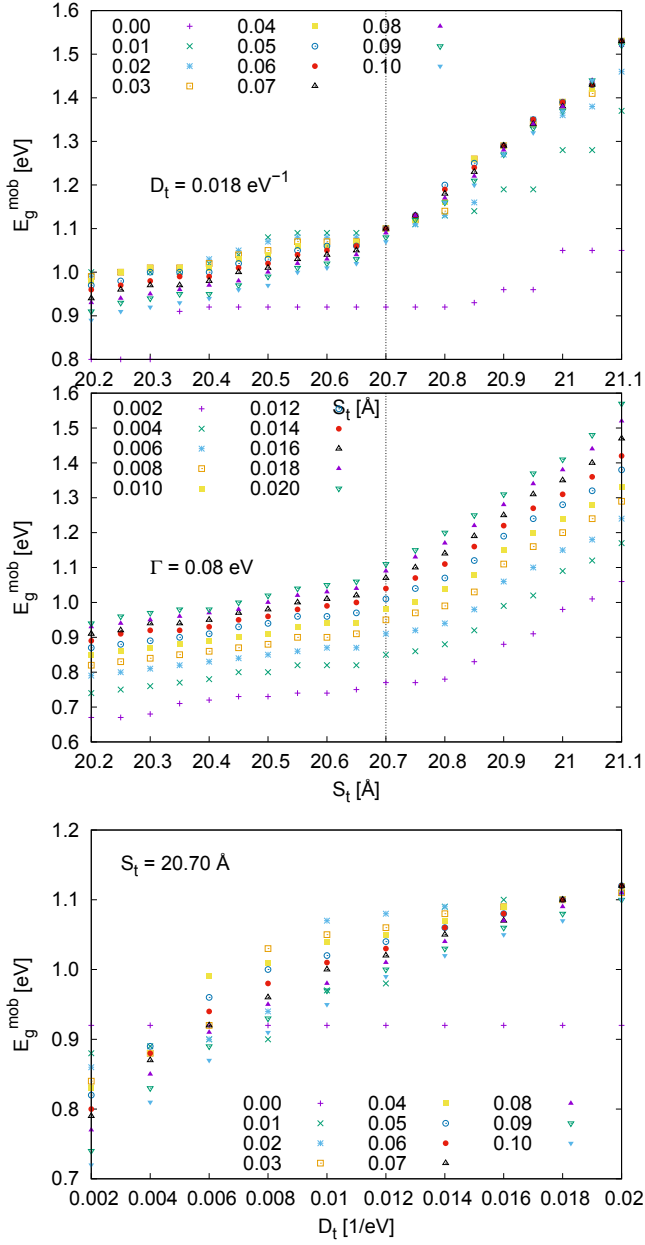


Figure 2.7: Dependence of E_g^{mob} on the parameters S_t , Γ , and D_t . One parameter is held fixed in each diagram. Increasing Γ and D_t smoothens the dependence on S_t , whereas decreasing Γ reduces dE_g^{mob}/dD_t .

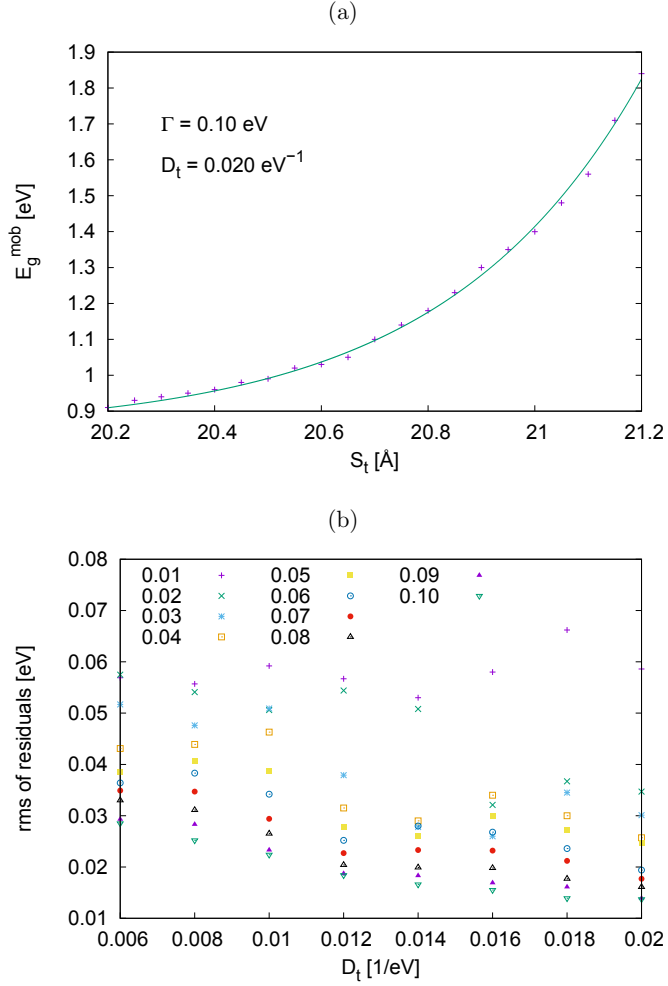


Figure 2.8: Exponential fit of E_g^{mob} as a function of S_t for $\Gamma = 0.1 \text{ eV}$ and $D_t = 0.02 \text{ eV}^{-1}$ (a). With the given parameters, E_g^{mob} is a relatively smooth function that is well described by the fit, which translates to a small value for the root mean square (rms) of the residuals. The same fitting is performed for all other parameter pairs, and the rms is measured (b). A smooth behavior leads to values close to 0.01 eV, whereas a steplike behavior leads to much higher values around 0.05 eV. Everything below 0.02 eV is considered sufficiently smooth.

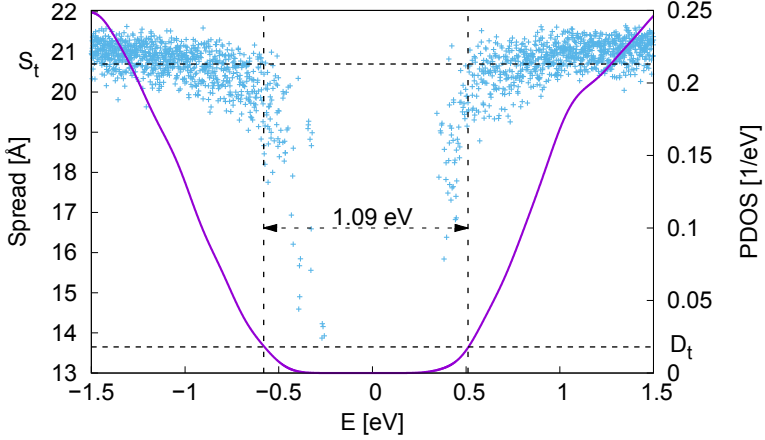


Figure 2.9: Mobility gap as obtained from the partial DOS (PDOS) of extended states with the final set of parameters $S_t = 20.7 \text{ \AA}$, $\Gamma = 0.08 \text{ eV}$, and $D_t = 0.018 \text{ eV}^{-1}$. The vertical lines indicate the mobility edges, which are obtained as the intersections of the horizontal line (D_t) with the PDOS. The spread of all states and the threshold S_t are plotted on the second y-axis.

which is a solution of the Maxwell equations under the assumptions of no excess charge and no free charge carriers. ϵ is here the macroscopic dielectric function, which in general is complex, such that we can write

$$n = \sqrt{\epsilon_1 + i\epsilon_2} \equiv n_0 + i\kappa, \quad (2.126)$$

where n_0 is called the refractive index and κ the extinction coefficient. The wave therefore consists of an oscillating and a decaying part,

$$\mathbf{E}(x, t) = \mathbf{E}_0 \exp\left(iE\left(\frac{n_0}{c_0}x - t\right)\right) \exp\left(-E\frac{\kappa}{c_0}x\right), \quad (2.127)$$

such that the intensity is given by

$$I(x) \propto |\mathbf{E}(x, t)|^2 = |\mathbf{E}_0|^2 \exp\left(-2E\frac{\kappa}{c_0}x\right) \equiv I_0 \exp(-\alpha x), \quad (2.128)$$

which defines the energy-dependent absorption coefficient

$$\alpha(E) = 2\frac{E\kappa}{c_0} = 2\frac{E}{c_0} \frac{\epsilon_2}{\Re\sqrt{\epsilon_1 + i\epsilon_2}}. \quad (2.129)$$

Macroscopic dielectric function

The absorption spectrum depends on the macroscopic dielectric function, which in this section we will call ϵ^M to distinguish it from the microscopic dielectric function defined in equation

(2.59). ϵ^M is in general a tensor, but becomes a scalar function in isotropic materials, which amorphous silicon can be treated as in good approximation. Analogously to the microscopic dielectric function, ϵ^M relates the macroscopic average of a perturbative potential V to the macroscopic average of the effective potential V_{eff} :

$$V^M(\mathbf{q}) = \epsilon^M(\mathbf{q})V_{\text{eff}}^M(\mathbf{q}) , \quad (2.130)$$

where

$$V^M(\mathbf{q}) = V_{\mathbf{G}=\mathbf{0}}(\mathbf{q}) \quad (2.131)$$

is the long-wavelength limit of V in plane-wave representation. \mathbf{q} is the wave vector in the first Brillouin zone, which will be omitted in the following for better readability. Assuming that the perturbation is varying slowly, i.e., has a wavelength much longer than the dimension of the super cell, which is always the case for light around the visible range, we can make the approximation

$$V_{\mathbf{G}} = V^M \delta_{\mathbf{G},\mathbf{0}} . \quad (2.132)$$

Then the macroscopic dielectric function can be related to the microscopic one by

$$\epsilon^M = \frac{V^M}{V_{\text{eff},\mathbf{G}=\mathbf{0}}} = \frac{V^M}{\sum_{\mathbf{G}} \epsilon_{\mathbf{0}\mathbf{G}}^{-1} V_{\mathbf{G}}} = \frac{1}{\epsilon_{\mathbf{0}\mathbf{0}}^{-1}} , \quad (2.133)$$

where (2.58) was used. The calculation of the spectrum $\epsilon^M(\mathbf{q}; E)$ thus requires the calculation and inversion of $\epsilon(\mathbf{q}; E)$ at a high number of frequencies, which is computationally very expensive. This can be avoided by making the additional approximation

$$V_{\text{eff},\mathbf{G} \neq \mathbf{0}} \approx 0 , \quad (2.134)$$

which is justified if local-field effects, i.e., local responses to the macroscopic potential, are assumed to be small. In this case

$$\epsilon^M = \frac{V_{\mathbf{G}=\mathbf{0}}}{V_{\text{eff}}^M} = \frac{\sum_{\mathbf{G}} \epsilon_{\mathbf{0}\mathbf{G}} V_{\text{eff},\mathbf{G}}}{V_{\text{eff}}^M} \approx \epsilon_{\mathbf{0}\mathbf{0}} , \quad (2.135)$$

which is significantly easier to calculate. Using (2.63) and the Fourier transform of the Coulomb interaction

$$v_{c\mathbf{G},\mathbf{G}'}(\mathbf{q}) = \frac{4\pi}{|\mathbf{G} + \mathbf{q}|^2} \delta_{\mathbf{G}\mathbf{G}'} , \quad (2.136)$$

we obtain

$$\epsilon^M(\mathbf{q}; E) = 1 - \frac{4\pi}{|\mathbf{q}|^2} P_{\mathbf{0}\mathbf{0}}(\mathbf{q}; E) , \quad (2.137)$$

with the polarizability P defined in (2.60). Fourier transformation of P in the random phase approximation (RPA), equation (2.68), yields

$$P_{\mathbf{0}\mathbf{0}}(\mathbf{q}; E) = \frac{1}{V} \sum_{vc} \langle \psi_c | e^{-i\mathbf{q}\cdot\mathbf{r}} | \psi_v \rangle \langle \psi_v | e^{i\mathbf{q}\cdot\mathbf{r}} | \psi_c \rangle \left(\frac{1}{E + \varepsilon_v - \varepsilon_c + i\eta} - \frac{1}{E - \varepsilon_v + \varepsilon_c - i\eta} \right) ,$$

(2.138)

where the index v refers to valence band states and the index c to conduction band states. Assuming the wave functions are Bloch waves $|v\mathbf{k}\rangle$ and $|c\mathbf{k}\rangle$, respectively, that are normalized on the volume $V = N_k\Omega$, where Ω is the unit cell volume and N_k the number of \mathbf{k} -points, we define the matrix elements $M_{vc}(\mathbf{k}, \mathbf{q})$ as

$$\langle v\mathbf{k}' | e^{i\mathbf{q}\cdot\mathbf{r}} | c\mathbf{k} \rangle = \sum_{\mathbf{G}\mathbf{G}'} \langle v\mathbf{k}' | \mathbf{G}' + \mathbf{k}' \rangle \langle \mathbf{G}' + \mathbf{k}' | e^{i\mathbf{q}\cdot\mathbf{r}} | \mathbf{G} + \mathbf{k} \rangle \langle \mathbf{G} + \mathbf{k} | c\mathbf{k} \rangle \quad (2.139)$$

$$= \sum_{\mathbf{G}\mathbf{G}'} \langle v\mathbf{k}' | \mathbf{G}' + \mathbf{k}' \rangle \langle \mathbf{G} + \mathbf{k} | c\mathbf{k} \rangle \delta_{\mathbf{G}\mathbf{G}'} \delta_{\mathbf{k}'=\mathbf{k}+\mathbf{q}} \quad (2.140)$$

$$= \langle v\mathbf{k} + \mathbf{q} | e^{i\mathbf{q}\cdot\mathbf{r}} | c\mathbf{k} \rangle \delta_{\mathbf{k}'=\mathbf{k}+\mathbf{q}} \quad (2.141)$$

$$\equiv M_{vc}(\mathbf{k}, \mathbf{q}) \delta_{\mathbf{k}'=\mathbf{k}+\mathbf{q}}, \quad (2.142)$$

which implies a \mathbf{k} -space selection rule for the coupling of valence and conduction states. We therefore obtain for the RPA dielectric function

$$\epsilon^M(\mathbf{q}; E) = 1 - \frac{4\pi}{N_k\Omega} \sum_{\mathbf{k}vc} \frac{|M_{vc}(\mathbf{k}, \mathbf{q})|^2}{|\mathbf{q}|^2} \left(\frac{1}{E + \varepsilon_{v\mathbf{k}+\mathbf{q}} - \varepsilon_{c\mathbf{k}} + i\eta} - \frac{1}{E - \varepsilon_{v\mathbf{k}+\mathbf{q}} + \varepsilon_{c\mathbf{k}} - i\eta} \right). \quad (2.143)$$

For the purpose of calculating the absorption of light we are interested in the long-wavelength limit $\mathbf{q} \rightarrow 0$. Using $\lim_{\mathbf{q} \rightarrow 0} e^{i\mathbf{q}\cdot\mathbf{r}} = 1 + i\mathbf{q} \cdot \mathbf{r}$ we obtain

$$\lim_{\mathbf{q} \rightarrow 0} \frac{M_{vc}(\mathbf{k}, \mathbf{q})}{|\mathbf{q}|} = \lim_{\mathbf{q} \rightarrow 0} \frac{\mathbf{q}}{|\mathbf{q}|} \cdot \langle v\mathbf{k} + \mathbf{q} | i\mathbf{r} | c\mathbf{k} \rangle \quad (2.144)$$

$$= \mathbf{e} \cdot \langle v\mathbf{k} | i\mathbf{r} | c\mathbf{k} \rangle \quad (2.145)$$

$$= \mathbf{e} \cdot \frac{\langle v\mathbf{k} | iH\mathbf{r} | c\mathbf{k} \rangle - \langle v\mathbf{k} | i\mathbf{r}H | c\mathbf{k} \rangle}{\varepsilon_{v\mathbf{k}} - \varepsilon_{c\mathbf{k}}} \quad (2.146)$$

$$= \mathbf{e} \cdot \frac{\langle v\mathbf{k} | \mathbf{v} | c\mathbf{k} \rangle}{\varepsilon_{v\mathbf{k}} - \varepsilon_{c\mathbf{k}}}, \quad (2.147)$$

where $\mathbf{v} = i[H, \mathbf{r}]$ is the velocity operator and \mathbf{e} the polarization vector of the incoming light. The macroscopic dielectric function in the limit $\mathbf{q} \rightarrow 0$ is therefore given by

$$\epsilon^M(E) = 1 - \frac{4\pi}{N_k\Omega} \sum_{\mathbf{k}vc} \frac{|\mathbf{e} \cdot \langle v\mathbf{k} | \mathbf{v} | c\mathbf{k} \rangle|^2}{(\varepsilon_{c\mathbf{k}} - \varepsilon_{v\mathbf{k}})^2} \left(\frac{1}{E + \varepsilon_{v\mathbf{k}} - \varepsilon_{c\mathbf{k}} + i\eta} - \frac{1}{E - \varepsilon_{v\mathbf{k}} + \varepsilon_{c\mathbf{k}} - i\eta} \right), \quad (2.148)$$

which, separated in real part ϵ_1 and imaginary part ϵ_2 and considering only the positive part of the energy spectrum, gives

$$\epsilon_1(E) = 1 - \frac{8\pi}{N_k\Omega} \sum_{\mathbf{k}vc} \frac{|\mathbf{e} \cdot \langle v\mathbf{k} | \mathbf{v} | c\mathbf{k} \rangle|^2}{\varepsilon_{c\mathbf{k}} - \varepsilon_{v\mathbf{k}}} \frac{1}{E^2 - (\varepsilon_{c\mathbf{k}} - \varepsilon_{v\mathbf{k}})^2} \quad (2.149)$$

$$\epsilon_2(E) = \frac{4\pi^2}{N_k\Omega} \frac{1}{E^2} \sum_{\mathbf{k}vc} |\mathbf{e} \cdot \langle v\mathbf{k} | \mathbf{v} | c\mathbf{k} \rangle|^2 \delta(\varepsilon_{c\mathbf{k}} - \varepsilon_{v\mathbf{k}} - E). \quad (2.150)$$

Optical Matrix elements

The elements of the sum in (2.150) correspond to Fermi's golden rule for the probabilities of valence band electrons being excited to a conduction state under photon absorption. These probabilities depend on the optical coupling between the initial and the final states, given by the optical transition matrix elements $v_{v\mathbf{c}\mathbf{k}} = \langle \mathbf{k}v | \mathbf{e} \cdot \mathbf{v} | \mathbf{c}\mathbf{k} \rangle$. By defining the average coupling strength

$$\langle v^2 \rangle (E) = \frac{\sum_{v\mathbf{c}\mathbf{k}} |v_{v\mathbf{c}\mathbf{k}}|^2 \delta(\varepsilon_{\mathbf{c}\mathbf{k}} - \varepsilon_{v\mathbf{k}} - E)}{\sum_{v\mathbf{c}\mathbf{k}} \delta(\varepsilon_{\mathbf{c}\mathbf{k}} - \varepsilon_{v\mathbf{k}} - E)}, \quad (2.151)$$

which describes the average transition probability for all transitions with a given energy E , the imaginary part of the dielectric function can be written as

$$\epsilon_2(E) \propto \frac{\langle v^2 \rangle (E) J(E)}{E^2}, \quad (2.152)$$

with the joint density of states (JDOS)

$$J(E) = \sum_{v\mathbf{c}\mathbf{k}} \delta(\varepsilon_{\mathbf{c}\mathbf{k}} - \varepsilon_{v\mathbf{k}} - E). \quad (2.153)$$

Equation (2.152) means that the energy dependence of both the DOS/JDOS and the coupling strength has to be analyzed in order to understand and model absorption in a-Si:H and to determine the optical band gap. (2.151) can also be generalized to calculate the average coupling strength as a function of any other property than the transition energy, such as the localization, or the initial or final energy. This is done by averaging over all transitions or states with the property of interest, instead of averaging over all transition with a given transition energy.

The numerical evaluation of the matrix elements is done in terms of finite differences, by calculating the valence states on a \mathbf{k} -point grid that is shifted by a small vector \mathbf{q} , and then using (2.147) to calculate

$$v_{v\mathbf{c}\mathbf{k}} \approx (\varepsilon_{v\mathbf{k}} - \varepsilon_{\mathbf{c}\mathbf{k}}) \frac{M_{vc}(\mathbf{k}, \mathbf{q})}{|\mathbf{q}|}. \quad (2.154)$$

This is necessary due the use of non-local pseudopotentials v^{PP} in the DFT calculation, which results in

$$\mathbf{v} = i[H, \mathbf{r}] = -i\nabla + i[v^{\text{PP}}, \mathbf{r}], \quad (2.155)$$

meaning that \mathbf{v} cannot be replaced by the momentum operator $\mathbf{p} = -i\nabla$, which would allow for an analytic evaluation of the matrix elements. In the case that quasiparticle corrections are applied, also the non-locality of the self-energy operator has to be taken into account, which modifies the matrix elements even if the quasiparticle wave functions are approximated by the Kohn-Sham wave functions. As can be seen directly from (2.154), the modification then consists of the renormalization

$$v_{v\mathbf{c}\mathbf{k}}^{\text{QP}} = \frac{\varepsilon_{v\mathbf{k}}^{\text{QP}} - \varepsilon_{\mathbf{c}\mathbf{k}}^{\text{QP}}}{\varepsilon_{v\mathbf{k}}^{\text{KS}} - \varepsilon_{\mathbf{c}\mathbf{k}}^{\text{KS}}} v_{v\mathbf{c}\mathbf{k}}^{\text{KS}}. \quad (2.156)$$

Optical gap

Whereas in crystalline semiconductors the absorption spectrum has a sharp onset at the direct band gap energy, the definition of the optical gap E_g in amorphous semiconductors is ambiguous due to the existence of localized gap states. The most commonly used definition, especially in experimental physics, is the so-called Tauc gap [58], where the linear regime of $\sqrt{\alpha E}$ is extrapolated and E_g is determined as the intersection of the extrapolated line with the energy axis. This method is based on three assumptions:

1. For band states, i.e., states that are not localized, The DOS increases as \sqrt{E} from the band edges, just as in a crystalline semiconductor, resulting in a quadratic energy dependence for the JDOS: $J(E) \propto (E - E_g)^2$
2. The optical coupling strength $\langle v^2 \rangle(E)$ is constant near E_g
3. The refractive index $n_0(E)$ is constant near E_g and therefore $\alpha(E) \propto E\epsilon_2(E)$.

From these assumptions it follows that $\alpha(E) \propto (E - E_g)^2/E$, and therefore $\sqrt{\alpha E}$ is linear near E_g and its onset yields the optical gap. Even though these assumptions do not strictly hold, the method still gives sensible results, which is due to the fact that the errors in the approximations for J , $\langle v^2 \rangle$, and n_0 can roughly compensate [59]. Another problem with this method of determining the optical gap is, however, that the linear regime cannot always be clearly identified, and the result of the extrapolation depends sensitively on the fitting range. Instead of determining the optical gap from the absorption spectrum, according to the first assumption we can also directly obtain E_g from the JDOS by linearly fitting $\sqrt{J(E)}$, which has usually a more pronounced linear regime, and therefore yields less ambiguous results. In addition, this method avoids making any assumptions on the coupling strength and the refractive index.

3 Hydrogenated amorphous silicon

This chapter presents an *ab initio* study of the structural, electronic, and optical properties of hydrogenated amorphous silicon (a-Si:H). The first section gives an overview over the properties and applications of a-Si:H, the challenges that are met when trying to model it, the progress in the field so far, and the goals of the present work. The second section describes the technical details of the computations. The following sections present the results, divided into structural, electronic, and optical properties, which are summarized and discussed in the final section.

3.1 Introduction

Hydrogenated amorphous silicon (a-Si:H) has been used as a cheap and efficient absorber material in silicon thin-film solar cells for more than 40 years [60], and has lately found another application in photovoltaics as a passivation layer in silicon-heterojunction cells. Understanding its microscopic structure in order to optimize its macroscopic properties for the application in photovoltaics has motivated several *ab-initio* studies of a-Si:H throughout the years [56, 61–66]. Two basic steps thereby need to be taken. First, a model atomic structure has to be generated that correctly reproduces certain experimental features of a-Si:H, such as the defect density, the radial pair correlation function, or the vibrational properties. Second, the electronic structure has to be calculated on a level that allows for the extraction of physically meaningful macroscopic properties. From the viewpoint of photovoltaics, special interest lies on the description of the optical properties and on the identification and characterization of localized defect states, which have a crucial impact on the device performance due to their role as recombination centers in non-radiative recombination [67].

The fundamental difference between the amorphous and the crystalline phase of silicon is that amorphous silicon (a-Si), unlike crystalline silicon (c-Si), does not have a well-defined atomic structure. Even though a tetrahedral short-range order is still maintained, the bond angles and lengths are distorted irregularly as compared to the diamond structure, leading to a complete loss of long-range order, and to the formation of defects in the form of dangling or floating bonds, i.e., atoms being less or more than fourfold coordinated. If seen as a perturbation of the crystalline structure, the disorder gives rise to a mixing of the crystalline Bloch states, such that the resulting states are not labeled by the \mathbf{k} -vector anymore. This also breaks up the \mathbf{k} -selection rule for optical transitions, which means that a-Si, unlike c-Si, behaves like a direct semiconductor. Another effect of the mixing is the emergence of weakly localized states near the band edges, which form a tail in the density of states decaying exponentially into the gap, and are therefore called tail states. Low-lying valence states and energetically high nearly-free electron states on the other hand retain their extended, band-like character and are thus referred to as band states. Since band and tail states cannot be cleanly separated, the concept of a sharp band gap is replaced by the concept of an optical gap, which, roughly speaking, refers to the energy range where no absorption occurs, and the mobility gap, where no transport takes place. The fact that, despite the strong disorder, a gap similar to that in c-Si exists at all in a-Si, is due to the existence of short-range order [68]. Where that order is broken, however, states arise in the middle of the gap, which are strongly localized near the

defect. These so-called mid-gap states are the third type of states found in a-Si. In photovoltaic applications they are unwanted as they have a negative impact on the device performance by enhancing recombination. Their number can, however, be largely decreased through hydrogen passivation, i.e., insertion of hydrogen atoms that bond with under-coordinated atoms and thus shift localized states out of the gap. This is the reason why a-Si:H instead of pure a-Si is used in photovoltaics. In addition, the hydrogen content modifies the optical and mobility gap, and can therefore be used as a means of band gap engineering [68].

The lack of long-range order in a-Si:H makes modeling it very challenging. First, there exists no rule or pattern for finding the atomic positions. On the other hand though, the atoms also cannot be placed completely randomly, because in reality the distortions and defects in the atomic structure, despite being locally random, follow certain statistics, which have to be reproduced by the model. Second, as opposed to c-Si, where only one unit cell needs to be considered that is repeated periodically, huge numbers of atoms are, in principle, required in a model a-Si:H structure. However, conventional ab-initio methods are currently still limited to maximum numbers of the order of 1000 atoms, which is orders of magnitude smaller than the number of atoms in a real sample. A structure of this size would suffer greatly from surface effects and would not be suitable to reproduce the experimental properties of the bulk material. This problem has to be avoided by constructing a super cell with periodic boundary conditions that is infinitely repeated, which however introduces an artificial periodicity, and therefore still needs to be large enough to suppress any interaction with periodic images. The third major problem is, that there exists not only one kind of a-Si:H with well-defined material properties, but instead, all macroscopic properties depend on the conditions (temperature, pressure, hydrogen concentration, ...) under which the material was produced, which makes the verification of numerical results by comparison with experimental data very difficult. This is true especially for the optical and mobility gap, where the additional difficulty emerges, that no sharp definition, neither for their experimental determination, nor their numerical calculation, exists.

Among the structural properties that have to be reproduced by a-Si:H models, the defect density is particularly delicate. In fact, structures containing only one defect need to have a size of at least 10^6 atoms to yield realistic defect densities [68], which is out of the range of current studies dealing with structure sizes of the order of 1000 atoms. Hence, while the generation of defective a-Si:H configurations is instructive for studying the origin and the nature of localized defect states, these configurations are not well suited for obtaining realistic macroscopic properties. The generation of defect-free configurations is therefore an important step towards a full ab-initio description of a-Si:H. However, for a long time defect-free configurations of a-Si and a-Si:H could be generated only with model approaches such as the Wooten-Winer-Weaire algorithm [69], the Bethe-lattice approach [61] or the Reverse Monte-Carlo approach [70]. Only recently, large-scale (~ 500 atoms) atomistic simulations of a-Si:H using a quench-from-a-melt approach [66, 71] combining both classical and ab-initio molecular dynamics (MD) have been reported to yield configurations of low defect density [56]. The same approach was used to generate low-defect and even defect-free a-Si:H configurations of 72 atoms within ab-initio MD [65]. This method was also used to generate the configurations analyzed in this work.

The calculation and analysis of the electronic structure and the optical properties of a-Si:H on the Density-Functional-Theory (DFT) level has been the subject of a number of recent works [56, 63–66]. The focus of interest in these works has been mainly on the origin of mid-gap

states and band tails, and on the effect of hydrogen concentration and structural features on the mobility gap and the optical gap respectively. Very little attention has however been paid to the effect of computational artifacts on the electronic and optical properties. In particular, two effects should be taken into account when trying to reproduce the experimental properties of a-Si:H, and are therefore investigated in this work: the effect of the super-cell size and the effect of many-body interactions. A recent work stated that finite size effects do not play any role for structures larger than 72 atoms [65], which will be revised here by comparing structures of different size. The incomplete description of many-body effects on the other hand is a well-known problem of standard DFT [72] (see section 2.1.3), and is the reason why the optical and mobility gaps are severely underestimated in previous studies using the local density approximation (LDA) or the generalized gradient approximation (GGA). Good values for the gaps have however been achieved recently with hybrid functionals [56]. In this work we try to incorporate many-body interactions systematically by explicitly calculating the quasiparticle corrections to the Kohn-Sham energies. These corrections are often described by a heuristic approach, termed scissors shift, where the electron energies are simply shifted to fit the experimental band gap. Since a distinct experimental value of the band gap of a-Si:H does however not exist, a set of shifting parameters can only be determined from a GW calculation, which will be demonstrated here.

3.2 Computational details

The a-Si:H configurations analyzed in this work were generated with a simulated annealing quench-from-a-melt protocol [66, 71, 73] with subsequent thermalization at 300 K, using Born-Oppenheimer molecular dynamics on the GGA-DFT level. Two types of configuration are studied, one consisting of 64 Si + 8 H atoms (Fig. 3.1(a)), which we will refer to as the small system, and one consisting of 512 Si + 64 H atoms (Fig. 3.1(b)), which we will refer to as the large system. The hydrogen concentration of about 11% is chosen as this is the nominal concentration used in experimental materials optimized for photovoltaic performance [53]. Both systems use a cubic super cell with periodic boundary conditions with a size of $a = 11.06 \text{ \AA}$ and $a = 22.12 \text{ \AA}$, respectively, resulting in a density of 2.214 g/cm^3 , which matches the experimental value at the chosen hydrogen concentration [74]. The generation of the atomic structures was not part of this work and is therefore not described in detail here. This information can however be found in a previous publication [6].

The electronic structure is calculated self-consistently within DFT with the plane-wave pseudopotential code PWscf from the Quantum ESPRESSO package [75, 76] using norm-conserving pseudopotentials and a PBE-GGA functional [24]. \mathbf{k} -point summations are carried out on a $4 \times 4 \times 4$ grid for the small system, and on a $2 \times 2 \times 2$ grid for the large system. The plane-wave cut-off energy is set to 52 Ry. These parameters were chosen by checking the convergence of the total energy of the system (Fig. 3.2), and are consistent with the assumptions that the cut-off energy should be independent of the system size, whereas the number of \mathbf{k} -points needed is inverse proportional to the system size.

Quasiparticle corrections to the Kohn-Sham energies for the small configuration are obtained by performing single-shot G_0W_0 calculations with the BerkeleyGW code [77] within the gener-

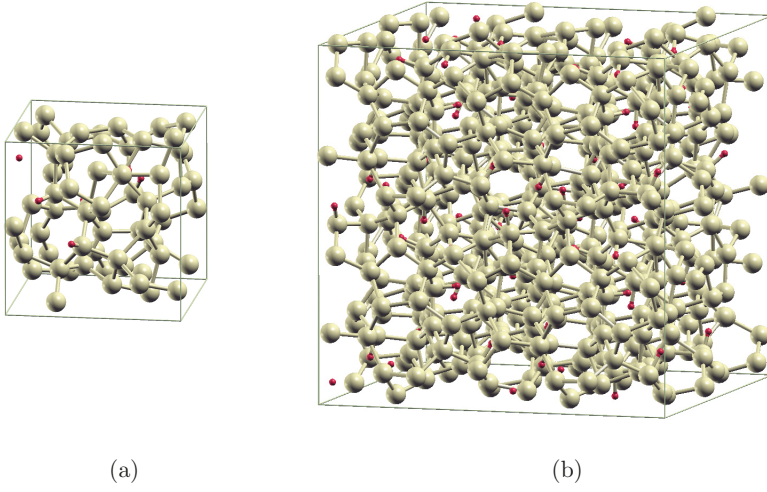


Figure 3.1: Small (a) and large (b) a-Si:H configuration in the simulation box. Si atoms are grey, H atoms are red. The super cells consist of 64 Si + 8 H atoms (small system), and 512 Si + 64 H atoms (large system), respectively. Periodic boundary conditions are used in all three directions.

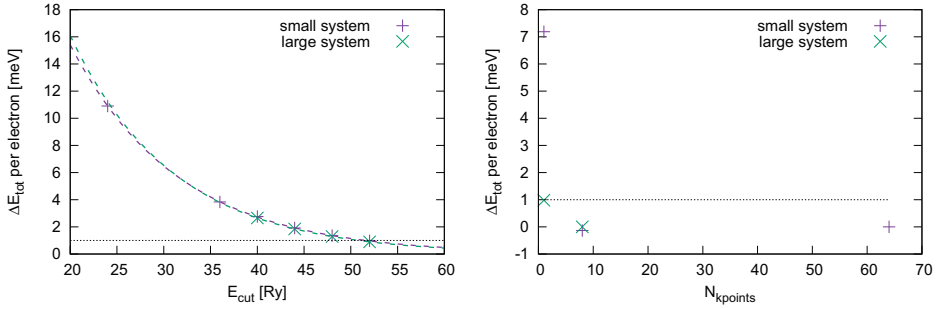


Figure 3.2: Convergence behavior of the total energy per electron w.r.t. the plane-wave cut-off E_{cut} (left) and the number of \mathbf{k} -points in the first Brillouin zone (right). W.r.t E_{cut} , the total energy converges exponentially, as indicated by the dashed lines, which represent exponential fits of the data points. The extrapolation to $E_{\text{cut}} \rightarrow \infty$ is used as the reference energy. At 52 Ry both systems are converged to this energy within 1 meV per electron (indicated by the horizontal line). For the \mathbf{k} -point convergence, the energy for the largest tested grid is used as reference. Convergence is assumed if the total energy per electron differs by less than 1 meV from the previous data point. This is the case at 64 ($4 \times 4 \times 4$) points for the small system, and at 8 ($2 \times 2 \times 2$) points for the large system.

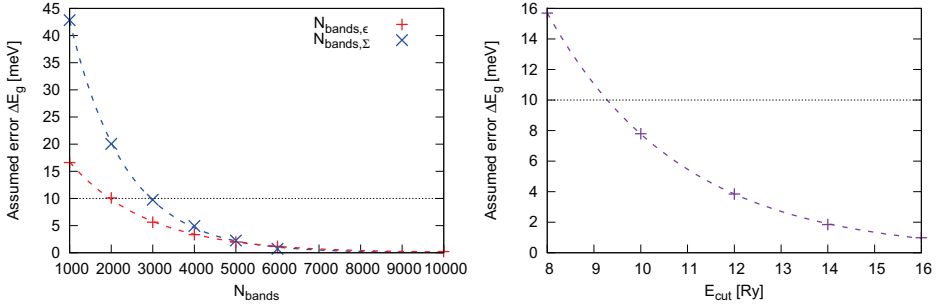


Figure 3.3: Convergence behavior of the assumed error ΔE_g of the LUMO-HOMO quasiparticle gap w.r.t. the number of bands included in the calculation of ϵ ($N_{\text{bands}}^\epsilon$) and Σ (N_{bands}^Σ), and w.r.t. the cut-off energy E_{cut} . The convergence w.r.t. each parameter is checked while setting the other two parameters to a high value, at which convergence is assumed, namely E_{cut} to 16 Ry, $N_{\text{bands}}^\epsilon$ to 10000, and N_{bands}^Σ to 6000. Exponential convergence is observed in all cases, and the reference values for E_g are obtained from exponential fits to the data points (dashed lines). A precision of 10 meV (horizontal line) is requested, which leads to $N_{\text{bands}}^\epsilon = N_{\text{bands}}^\Sigma = 3000$ and $E_{\text{cut}} = 10$ Ry. Calculating E_g with these parameters on a $2 \times 2 \times 2$ and a $4 \times 4 \times 4$ grid yields a difference of less than 2 meV.

alized plasmon-pole (GPP) approximation, using 3000 bands in the calculation of both ϵ and Σ , and a kinetic energy cut-off of 10 Ry. These values were chosen by checking the convergence of the LUMO-HOMO gap with respect to all three parameters simultaneously. In practice this means that two parameters are kept fixed at a sufficiently high value to assume convergence, while the third parameter is varied (Fig. 3.3). \mathbf{k} -point summations are performed on a $2 \times 2 \times 2$ grid. Using a $4 \times 4 \times 4$ grid changes the gap by less than 2 meV. The finite \mathbf{q} -shift needed for the numerical evaluation of $\lim_{\mathbf{q} \rightarrow 0} \epsilon_{00}(\mathbf{q}; E)$ is set to 0.0005 in crystal coordinates. The effect of this shift is found to be small by checking the convergence of the maximal error in $\epsilon_{00}(\mathbf{q}; E)$ with respect to \mathbf{q} (Fig. 3.4). The Kohn-Sham wave functions are retained as they are assumed to differ very little from the quasi-particle wave functions [42].

The BerkeleyGW code is also used for calculating the optical properties within linear-response theory using the random phase approximation (RPA) without local-field effects. The absorption spectra are calculated on a $2 \times 2 \times 2$ \mathbf{k} -point grid for both systems, with a gaussian broadening of 50 meV for the small, and 25 meV for the large configuration. Electron-hole interaction is disregarded as it is generally assumed to have no significant effect on the absorption spectra of amorphous semiconductors [68].

For the calculation of the density of states (DOS), the electron localization function (ELF), the spread, and the optical matrix elements, the electronic states are calculated on a $4 \times 4 \times 4$ grid for the small system, and on a $2 \times 2 \times 2$ grid for the large system, both with a plane-wave cut-off of 52 Ry. A gaussian broadening of 25 meV, which roughly corresponds to the thermal broadening at room temperature, is used for displaying the DOS.

The radial pair correlation functions are calculated with a gaussian broadening of 0.025 \AA .

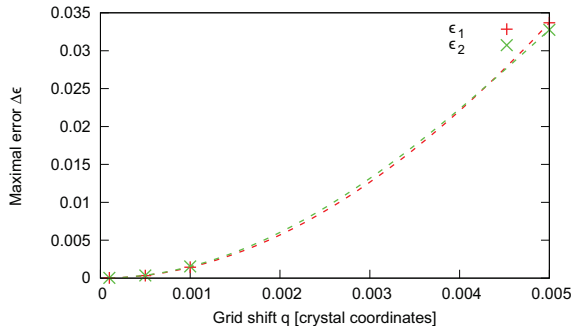


Figure 3.4: Maximal error $\Delta\epsilon = \max_E |\epsilon_{00}(\mathbf{q}; E) - \epsilon_{00}(0; E)|$ for the real part ϵ_1 and the imaginary part ϵ_2 made by replacing the limit $\mathbf{q} \rightarrow 0$ by a finite grid shift \mathbf{q} (small system). The reference value is obtained by extrapolation to $q = 0$, assuming the error to be of second order in q . The errors are very small, which means that the grid shift has no significant effect on the accuracy. A value of 0.0005 is chosen for the GW and absorption calculations.

3.3 Structural properties

In order to estimate the quality of the atomic configurations in terms of how closely they resemble real a-Si:H, we first investigate the radial pair correlation function $g(r)$. Fig. 3.5 shows $g_{\text{Si-Si}}(r)$ and $g_{\text{Si-H}}(r)$ both for the small and the large configuration. Except for the different smoothness of the curves, which is due to the different number of atom pairs, both systems show very similar behavior, indicating a similar structural quality. Both figures reveal sharp first nearest-neighbor peaks for Si-Si pairs, which are located at 2.32 Å (small system) and 2.38 Å (large system), respectively, close to the GGA value of 2.37 Å for c-Si [52]. This indicates a high degree of short-range order, with the small configuration being slightly more disordered than the large one according to the height of the peak. The second and higher nearest-neighbor peaks cannot be distinguished anymore, showing the characteristic loss of long-range order in amorphous silicon. For Si-H pairs there is a sharp peak at 1.51 Å (small system) and 1.53 Å (large system), respectively, meaning that most Si-H bonds have a bond length very close to these values.

In order to extract macroscopic properties, a configurational average, i.e. an average over multiple different configurations, should be taken. This is supposed to eliminate local features, for example due to defects, and thus allows for a better comparability with experiments. Therefore, in order to compare the calculated Si-Si radial pair correlation function with experimental data from neutron scattering [78], we average over 10 large configurations, extracted at different time steps of the molecular dynamics simulation, after thermalization was completed. The result is shown in Fig. 3.6, together with the curve for the single configuration and with the experimental data. The effect of the averaging is only a smoothing of the curve, whereas the overall behavior remains completely unchanged, meaning that the chosen configuration is representative for the ensemble. Comparison with the experiment shows excellent agreement at all all distances, indicating that our configurations model the structure of real a-Si:H very accurately.

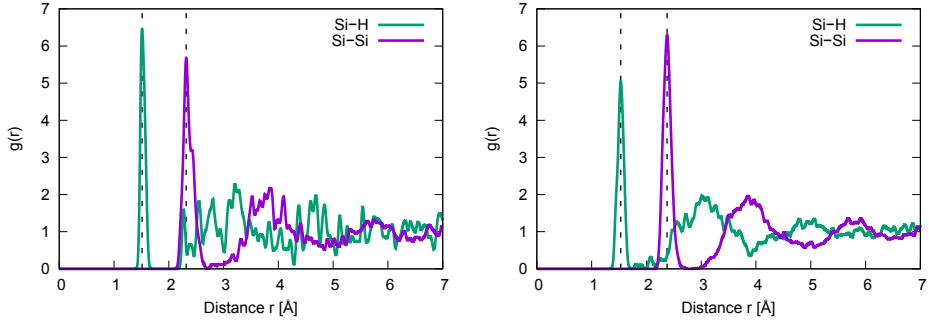


Figure 3.5: Radial pair correlation function $g(r)$ for Si-Si pairs and Si-H pairs in the small structure (left) and in the large structure (right). A gaussian broadening of 0.025 \AA was used. Except for the difference in smoothness due to the different number of atom pairs, both systems show similar behavior. For Si-Si pairs, the first nearest-neighbor peak is very pronounced, and is located at 2.32 \AA (small system) and 2.38 \AA (large system), respectively, which is close to the value of 2.37 \AA for c-Si in GGA-DFT. The second nearest-neighbor peak cannot be distinguished anymore, showing the loss of long-range order. Si-H pairs reveal a sharp peak at 1.51 \AA (small system) and 1.53 \AA (large system), respectively.

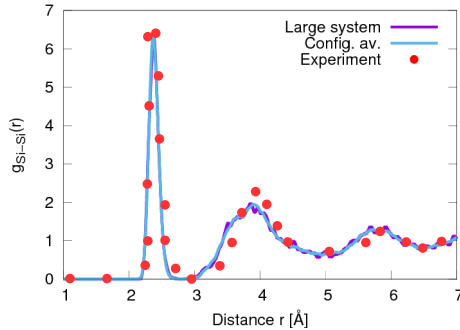


Figure 3.6: Comparison of Si-Si radial pair correlation function $g(r)$ in the large structure and in the configurational average with experimental data from neutron scattering [78]. The computational data is in excellent agreement with experiment. Taking the configurational average does not affect the main features but only leads to a smoothing of the curve.

Table 3.1: Coordination analysis for Si and H atoms in both a-Si:H systems. The coordination numbers are calculated with the ELF method. The small system is slightly more disordered than the large system, which is in fact defect-free. The small system has two dangling bonds, but no floating bonds are found in either system. The H atoms are all bonded to exactly one atom.

	Coordination number	Number of atoms	
		Small system	Large system
Si	1	0	0
	2	1	0
	3	0	0
	4	63	512
	5	0	0
H	0	0	0
	1	8	64
	2	0	0

The second measure for the structural quality of our configurations is the defect density, more precisely, the number of under- or overcoordinated atoms. These are determined by calculating the coordination number, i.e., the number of bonds formed, for each atom, using the ELF method described in sec. 2.3.2. The results are listed in Tab. 3.1.

The comparison shows that the small system is slightly more disordered, in agreement with the interpretation of the radial pair correlation function. As for the structural quality, the results of the ELF analysis show that the large configuration is completely defect-free, and should therefore be well suited to reproduce experimental properties of a-Si:H. The small configuration contains one atom with a coordination number of two, which means that it has two dangling bonds. This translates to a defect density of $1.5 \times 10^{21} \text{ cm}^{-3}$, which is about five orders of magnitude higher than experimentally measured values [79, 80], and therefore makes this configuration less comparable to real a-Si:H. It can, however, be used to study the effect of the defects on the electronic and optical properties. No floating bonds, i.e., over-coordinated atoms, are found in either configuration. The bonding analysis for the hydrogen shows that, as expected, all H atoms are bonded to exactly one Si atom, meaning that neither H_2 dimers, nor 'hydrogen bridges', i.e., H atoms bonded to two Si atoms, are found.

Even in the case of a defect-free configuration, which we have here, disorder in the form of stretched or shortened bonds exists and gives rise to tail or even gap states, as was argued by Khomyakov et al. [66]. The distribution of the bond lengths and the respective bond strengths, measured by the value of the ELF at the bond center, is shown in Fig. 3.7 for both configurations. The figures show that the bond lengths are distributed within roughly 0.4 \AA around a mean value of 2.37 \AA in the small system, and 2.38 \AA in the large system. The bond length and strength are weakly anti-correlated, with a correlation coefficient of -0.6 in the small system and -0.5 in the large system, but no monotonic dependence between the two

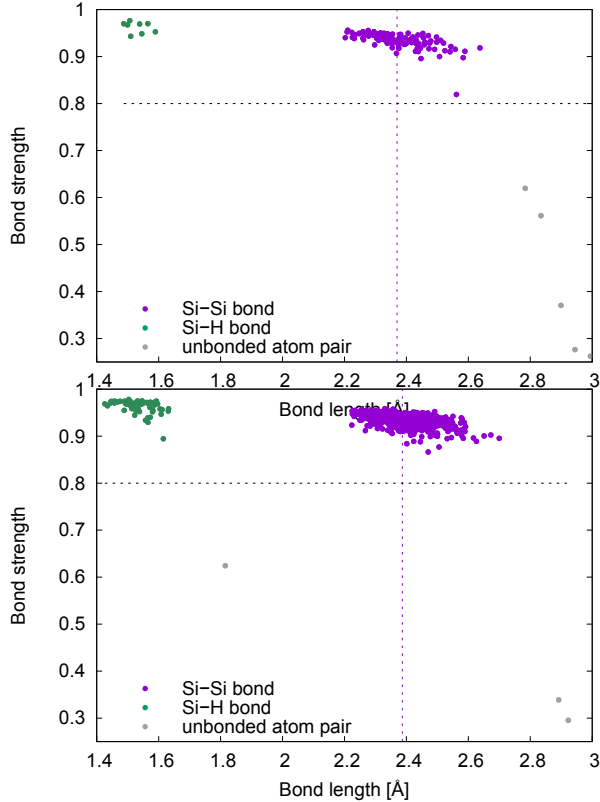


Figure 3.7: Distribution of bond lengths and respective bond strength for Si-Si bonds (purple points) and Si-H bonds (green points) in the small (top) and large (bottom) configuration. Unbonded atom pairs are represented by grey points. The bond strength is measured by the value of the ELF in the bond center. The threshold value of 0.8 for bonding is indicated by the horizontal line. The respective mean bond length for Si-Si bonds (2.37 Å in the small system, 2.38 Å in the large system) is marked by the vertical lines. In both systems, bonded and unbonded atom pairs can be clearly separated both in terms of the ELF and the atomic distance.

quantities exists. This explains the result that particularly stretched bonds, which are weaker on average, give rise to tail and gap states [66], but raises the question if conclusions about the electronic structure can be drawn from the geometry of the configuration only. In the case studied here, we can at least see that bonded and unbonded atom pairs can be clearly separated not only by the value of the ELF, but also by the distance. Consequently, applying for example a cut-off distance of 2.75 Å for Si-Si pairs and 1.70 Å for Si-H pairs, the bonding analysis with the geometrical method will here yield the same result as the ELF method. This is due to the strong short-range order present in these configurations, which makes it relatively easy to distinguish bonded from unbonded atoms.

3.4 Electronic properties

The electronic structure of both configurations is analyzed in terms of the density of states (DOS) and the electron localization, measured by the wave-function spread (Fig. 3.8). The analysis is restricted to an energy region of ± 3 eV around the Fermi level, since this is the region where transport, recombination, and absorption processes relevant for photovoltaics take place.

The DOS for the small configuration (Fig. 3.8(a)) reveals two distinct peaks inside the gap, which originate from localized states, i.e., states with low spread. Far away from the Fermi level, in the band region, the states become mostly delocalized, i.e., have a spread close to the dimension of the super cell. In between, a tail region with mostly semi-localized states can be identified, which is, however, not very pronounced, and is hard to distinguish from the band region. This is due to the relatively small difference in the spread of localized and extended wave functions, which makes an accurate definition of the mobility edges very difficult. In order to calculate the mobility gap with the method introduced in sec. 2.3.5, we chose a threshold value of $S_t = 10.0 \text{ \AA}$ for separating localized from extended states, ensuring that 95% of the valence band states (states more than 2 eV below the Fermi energy) exceed S_t . This way we obtain a mobility gap of $E_g^{\text{mob}} = 0.83 \text{ eV}$, which is very small compared to the experimental value of about 1.9 eV [57, 59]. Looking at the large configuration (Fig. 3.8(b)), we observe that the difference in the spread between localized and extended states is much larger, making it possible to clearly distinguish a band region with extended states, a tail region with semi-localized states, and a gap region with localized states. Representatives of each type of state are shown in (Fig. 3.8). Also, the relative difference in the spread of the band states is much smaller, making it easier to separate extended from localized states and thus to define the mobility edges. With a threshold of $S_t = 20.7 \text{ \AA}$ we obtain a value of $E_g^{\text{mob}} = 1.09 \text{ eV}$, and, averaging over 10 similar, defect-free configurations, a slightly higher value of 1.13 eV. This is still small compared to the experimental value, but significantly improved as compared to the small system. Also the density of localized states inside the gap in the large system is significantly lower than in the small system, supporting our previous statement that it is better suited to reproduce the properties of real a-Si:H.

The two peaks in the DOS of the small configuration generated by localized states can be clearly assigned to the two dangling bonds detected through the bonding analysis in the previous section. This can be seen in Fig. 3.9, where all localized states with a spread $S \leq 9.5 \text{ \AA}$ are plotted together with the atomic positions in the super cell. The position of the states thereby refers to the mean position (\mathbf{r}) of the electron, as defined in section 2.3.4. Almost all strongly localized states are localized directly at the site of the under-coordinated atom. All these states lie deep in the gap, i.e., have an energy close to the Fermi level. Occupied and unoccupied states are located at slightly different positions, and can therefore be related to the two different dangling bonds.

The existence of localized states in the large configuration can not be due to dangling bonds, as we established that this configuration is defect-free. Also, these states do not lie deep in the gap but close to the band edge, indicating that, very much like tail states, they origin from structural disorder rather than from defects. In order to demonstrate this, in Fig. 3.10, analogously to Fig. 3.9, localized states with a spread $S \leq 19 \text{ \AA}$ are plotted, in this case

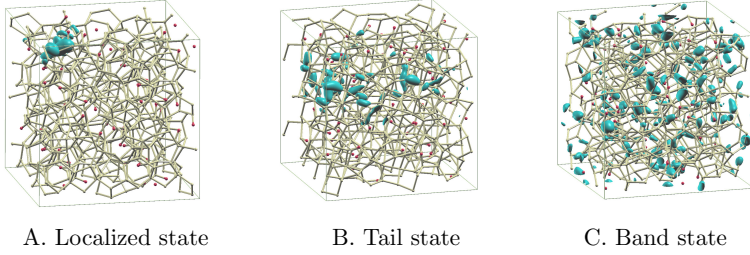
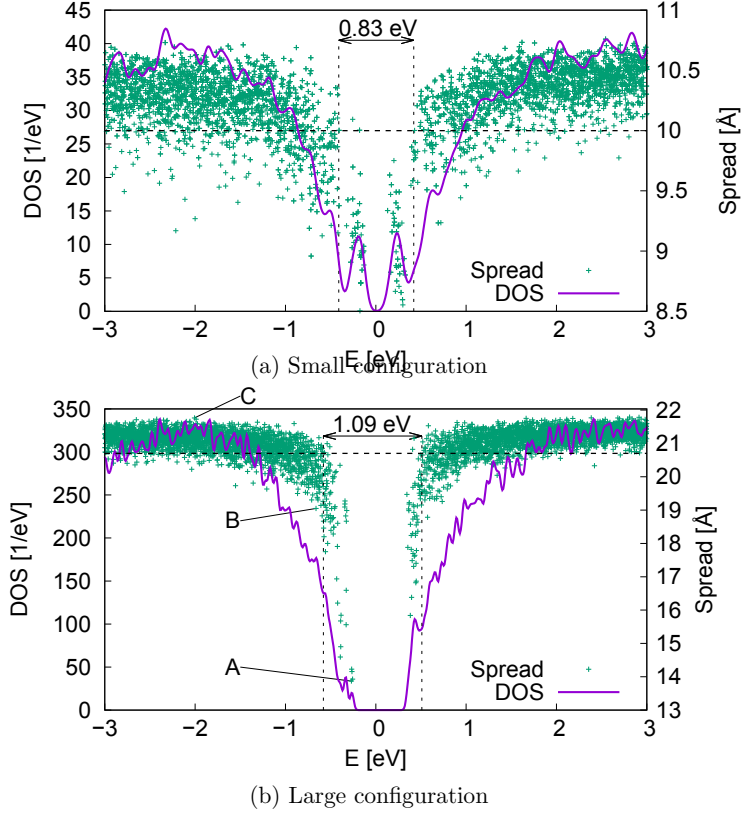


Figure 3.8: Density and spread of states in the vicinity of the Fermi energy (0 eV) for the small (a) and the large (b) configuration. Each dot represents the energy and the spread of one wave function. The mobility gap and edges (vertical lines) were obtained with a threshold of $S_t = 10.0 \text{ \AA}$ in the small, and $S_t = 20.7 \text{ \AA}$ in the large system, separating localized from extended states (horizontal lines). The value of $E_g^{\text{mob}} = 1.09 \text{ eV}$ obtained for the large configuration is much higher than the value of 0.83 eV in the small configuration. Also the different energy regions, gap, tail, and band, can be distinguished much more clearly in the large system. The different types of states, localized gap states, semi-localized tail states, and extended band states, are exemplarily labeled and plotted below in the form of isosurfaces of $|\psi|^2$.

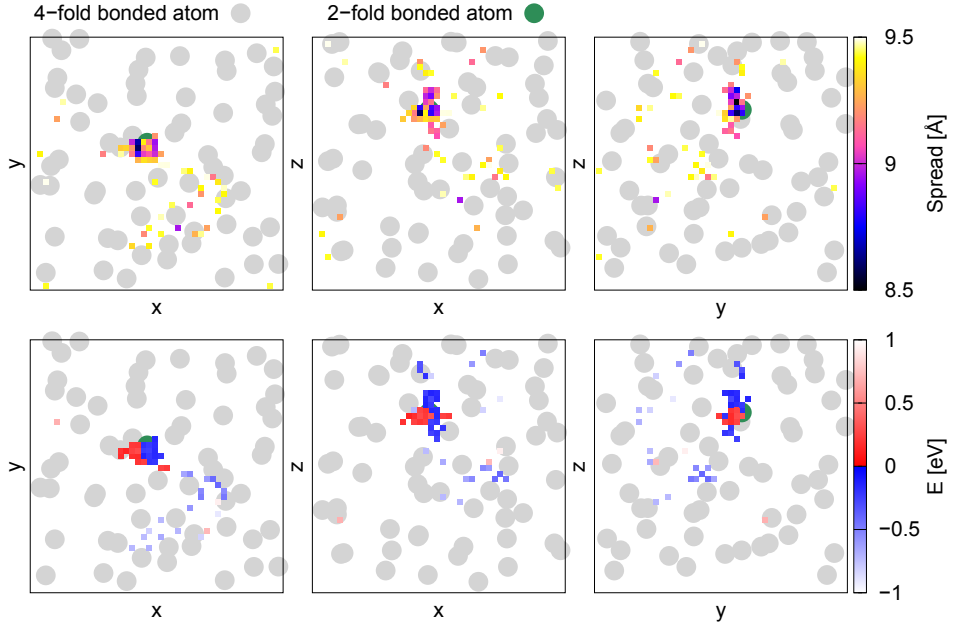


Figure 3.9: Distribution of localized states with $S \leq 9.5 \text{ \AA}$ in the super cell for the small system (projections onto the xy -, xz -, and yz -plane). Each dot represents one state, where the position indicates the mean position of the wave function, and the color denotes its spread (top) and its energy (bottom), respectively. The circles represent the Si atoms, where different colors stand for different coordination. Gap states both below and above the Fermi level (0 eV) are strongly localized at the under-coordinated atom, but are spatially separated and can therefore be assigned to two different dangling bonds. [6]

together with all Si-Si bonds in the super cell. The bonds are colored according to their strength, as defined in the previous section, and their length, respectively. This representation shows that strongly localized gap states can be found in the vicinity of particularly weak bonds (below-average bond strength), whereas strong bonds (above-average bond strength) do not affect localization. This is not surprising since, according to the LCAO (linear combination of atomic orbitals) model, a weaker bond will give rise to a smaller energy splitting between bonding and anti-bonding state, and thus push states towards the Fermi level. The length of the bonds on the other hand does not seem to have any direct effect on the electronic localization. In fact, no localized states can be found, both near some of the longest and near some of the shortest bonds. In conclusion, this means that localized states can exist even in the absence of dangling bonds, but knowledge of the structure only is not enough to make predictions about their existence and density. Also, their distinction from tail states is difficult, due to their position close to the band edge and their similar origin.

Whereas the different gap-state densities can be associated with the different defect structure of the two configurations, the overall difference in the behavior of the spread and, at least to some extent, also the different mobility gaps are clearly effects of the different super-cell size.

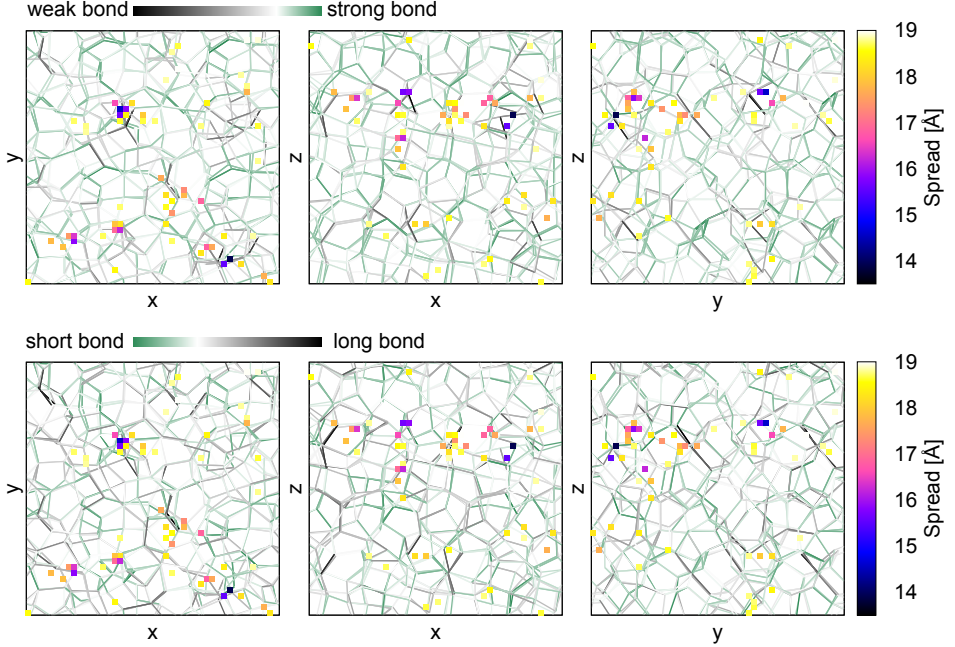


Figure 3.10: Distribution of localized states with $S \leq 19 \text{ \AA}$ in the super cell for the large system (projections onto the xy -, xz -, and yz -plane). Each dot represents one state, where the position indicates the mean position of the wave function, and the color denotes its spread. The lines represent the Si-Si bonds, and their color shows the strength (top) and their length (bottom), respectively. Localized states can be found in the vicinity of weak bonds (black lines, top), whereas the length of the bonds does not seem to affect localization.

This can be understood by considering that even the band states are not perfectly delocalized plane-waves but have regions of higher and lower probability density, leading to a spread smaller than the extension of the super cell. On the other hand, an exponentially localized tail state close to the mobility edge can have a spread that is of the order of the super-cell size, causing an underestimation of the mobility gap. However, when the size of the super cell is increased, the spread of an extended state will increase accordingly. This can be easily seen by considering a wave function ψ in a crystalline unit cell of dimension a , having a spread $S_1 = \sqrt{a^2 - S_0^2}$ according to equation (2.122), with $S_0 \in [0; a]$. Upon constructing a super cell out of n unit cells per dimension, $|\psi|^2$ and therefore also S_0^2 obviously remain invariant, and the spread becomes $S_n = \sqrt{n^2 a^2 - S_0^2} = n \sqrt{a^2 - S_0^2/n^2}$. This scales linearly with n for $n \rightarrow \infty$, while at the same time the relative difference between states with different S_0 vanishes. This is what we observe when increasing the super-cell size. The spread of an exponentially localized state, on the other hand, depends less on the cell size, as we also see by comparing the localized states in Fig. 3.8(a) and Fig. 3.8(b), and will converge to a finite value eventually. This separates tail and band states, and should lead to convergence of the mobility gap if the cell size is chosen large enough. Another effect of the finite size is a broadening of bands due

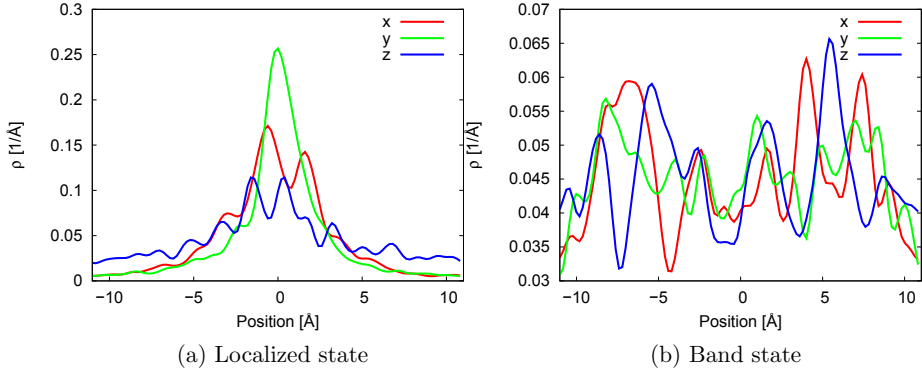


Figure 3.11: Probability density $\rho = |\psi|_i^2(x_i)$ along x , y , and z -direction for a localized (a) and a delocalized (b) wave function. The localized state shows almost perfect exponential localization only in y -direction, whereas it has multiple peaks along the other directions, and does not decay to zero at the z -boundaries. The band state is delocalized and shows some oscillating behavior inside the super cell, without however reproducing the crystalline periodicity.

to the interaction of semi-localized states with their periodic images, which could shift states out of the gap and therefore smear out the transition between band and tail states. Also this effect should vanish upon increasing the super-cell size. Even though the described finite-size effects are clearly visible in the calculations, it is very difficult to quantify them a priori. This is because neither are the band states perfect replications of crystalline Bloch waves, nor do localized states decay perfectly exponentially, but instead, all wave functions have a rather complicated shape, as can be seen from the examples in Fig. 3.11.

In addition to the error due to finite-size effects, the mobility gap calculated here suffers from the bad-gap problem of DFT caused by the incomplete description of many-body effects. In order to account for these effects, the mobility gaps are recalculated using quasiparticle corrected energy levels. These are obtained from a G_0W_0 calculation for the small configuration, and a scissors-shift correction for the large configuration, as described in the next section. The quasiparticle corrections improve the values of E_g^{mob} to 1.26 eV for the small, and 1.46 eV for the large system. It must however be stressed that only the energies are corrected whereas the wave functions and thus the spread remain the same. The values for E_g^{mob} are summarized in Tab. 3.3.

3.5 Optical properties

We investigate the optical properties of a-Si:H in terms of the absorption spectrum, which is one of the key quantities determining the solar cell efficiency in photovoltaics and is directly experimentally accessible, and in terms of its underlying microscopic quantities, the joint density of states (JDOS) and the optical matrix elements. A parameter that is commonly used

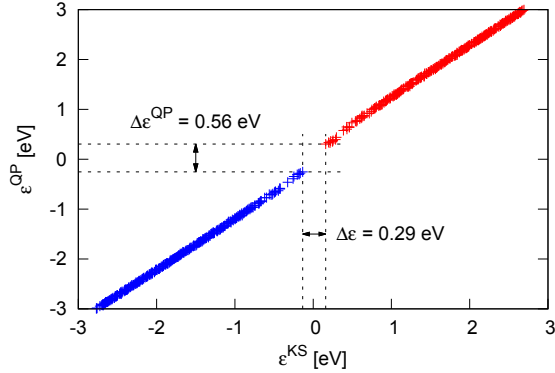


Figure 3.12: Quasiparticle corrected electron energies ϵ^{QP} vs uncorrected energies Kohn-Sham energies ϵ^{KS} . $\Delta\epsilon$ refers to the energy difference between the lowest unoccupied and the highest occupied state (LUMO-HOMO gap). The main effect of the corrections is a linear shift of the Kohn-Sham energies, which spreads the valence and conduction band by 0.27 eV. [6]

for the characterization of photovoltaic materials, and therefore well suited to compare our results to experiment, is the optical gap, which can be extracted from the spectral properties. As it is also subject to many-body effects, we apply quasiparticle corrections to the calculated DFT spectra in order to reach a better comparability with the experimental values.

3.5.1 G_0W_0 calculations

The G_0W_0 calculation for the small a-Si:H structure yields the quasiparticle corrected electron energies shown in Fig. 3.12. The results indicate that the effect of the quasiparticle corrections consists mainly in a linear shift of the Kohn-Sham energies, resulting in a spreading of valence and conduction band by approximately 0.27 eV. This suggests that the costly G_0W_0 calculation can be substituted by a simple scissors shift (see sec. 2.2.4). The respective shifting parameters $a_{v/c}$ and $E_{v/c}^s$ are obtained by a linear fit of the G_0W_0 results. The Fermi level is used as the reference energy, i.e., $E_v^0 = E_c^0 = E_F$. The choice of the right set of parameters depends on the energy range of interest. By using different energy ranges for fitting we obtain different parameter sets, which are listed in Tab. 3.2.

3.5.2 Absorption spectrum

The absorption spectrum of the small configuration calculated within the independent-particle (IP) approximation (i.e., with the uncorrected Kohn-Sham energies), the GW approximation, and the scissors-shift (SS) approximation is shown in Fig. 3.13(a). The IP spectrum shows two sub-gap absorption peaks at 0.34 eV and 0.60 eV. By comparison with the DOS the first peak

Table 3.2: Scissors shift parameters for a-Si:H obtained from a linear fit $\varepsilon_{v/c}^{\text{QP}} = \varepsilon_{v/c}^{\text{KS}} + a_{v/c}(\varepsilon_{v/c}^{\text{KS}} - E_F) + E_{v/c}^{\text{s}}$ of the quasiparticle energies obtained from the G_0W_0 calculation. The fitting ranges are given with respect to the Fermi level. Different fitting ranges result in different parameter sets and thus different LUMO-HOMO gaps. The resulting absorption spectra are plotted in Fig. 3.13(b). The first parameter set is best suited to reproduce the G_0W_0 absorption spectrum and LUMO-HOMO gap.

Fit. range [eV]	a_v	E_v^{s} [eV]	a_c	E_c^{s} [eV]	LUMO-HOMO [eV]
[-1 : 1]	0.088	-0.555	0.146	-0.329	0.56
[-2 : 2]	0.044	-0.587	0.064	-0.271	0.63
[-3 : 3]	0.025	-0.608	0.043	-0.244	0.67

can be related to absorption processes between two gap states, whereas the second peak arises from absorption processes between a gap state and a tail state. In order to estimate the optical gap we use a Tauc plot [58] (Fig. 3.15), which is the most common method for experimentally determining the optical gap of amorphous semiconductors. Since the spectrum is not smooth enough to allow for a reasonable fit, we increase the broadening to 200 meV. The resulting fit yields a Tauc gap of $E_g^{\text{T}} \approx 0.8$ eV, which is about 1 eV below the experimental values of approximately 1.7 to 1.8 eV [57, 59, 81]. The G_0W_0 correction modifies the absorption spectrum only in terms of a shift and a slight stretch, which results in a corrected Tauc gap of $E_g^{\text{T}} \approx 1.0$ eV. The figure shows that the G_0W_0 correction can be well approximated by a scissors shift, where the first parameter set in Tab. 3.2 was used. These parameters were chosen because they correctly reproduce the LUMO-HOMO gap, and because they best approximate the G_0W_0 absorption spectrum. This can be seen in Fig. 3.13(b), where the spectra for all three parameter sets are compared to the G_0W_0 spectrum.

After finding a suitable set of scissors shift parameters for a-Si:H, we use these parameters to calculate a quasi-particle corrected absorption spectrum also for the large configuration, for which a G_0W_0 calculation would be too costly. The result is shown in Fig. 3.14(a), together with the uncorrected spectrum. As compared to the small configuration, the sub-gap absorption decreased significantly. Moreover the optical gap obtained from the Tauc plot (Fig. 3.15) increased to 1.0 eV in the IP approximation, and to 1.3 eV with scissors-shift corrections. The relation between a larger super cell and a decreased sub-gap absorption can be easily understood in terms of the reduced defect density and the reduced spatial overlap of localized states. The difference in the Tauc gap can also be explained with the higher DOS inside the gap of the small configuration, giving rise to a higher JDOS at low energies. The super-cell size therefore seems to affect the optical gap only indirectly via the DOS inside the gap.

The spectra shown so far have limited physical significance, as they were obtained from single configurations, with super-cell sizes much smaller than the wavelength of visible light. In order to obtain a physically meaningful absorption spectrum of a-Si:H, i.e., a spectrum that can be compared to experimental data, the configurational average has to be taken. For that purpose we calculate spectra for 10 different large configurations and average over them. The result is shown in Fig. 3.14(b). While sub-gap absorption is still present in the averaged spectrum,

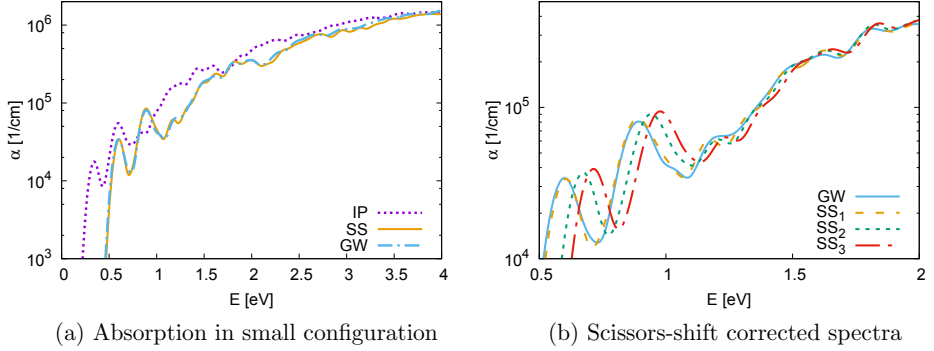


Figure 3.13: Absorption spectrum of the small configuration calculated in independent particle (IP), GW, and scissors-shift (SS) approximation (a). Qualitatively, all three spectra are similar, showing pronounced sub-gap absorption peaks. The quasiparticle corrections appear in the spectrum mainly as a shift of the onset. The SS spectrum was obtained with the first parameter set in Tab. 3.2, which was chosen because it best reproduces the GW spectrum, as can be seen by comparing the spectra generated by the three different parameter sets (b). [6]

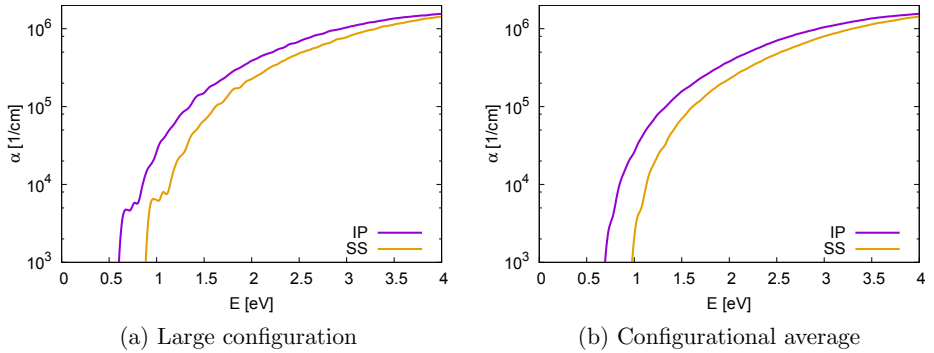


Figure 3.14: (a) Absorption spectrum of the large configuration calculated in IP and SS approximation, using the SS parameters obtained from the small system. Compared to the small configuration the Tauc gap is increased by 0.3 eV, whereas sub-gap absorption is reduced. (b) Absorption spectra averaged over 10 large configurations. The optical gap remains unaffected but the sub-gap peaks vanish. [6]

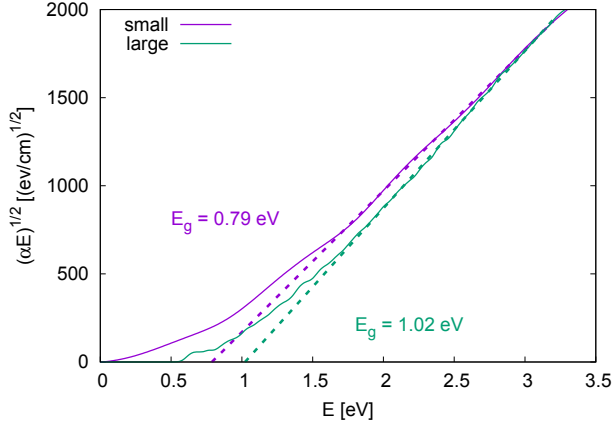


Figure 3.15: Tauc plot for the small and the large configuration in the IP approximation, yielding a Tauc gap of 0.8 eV and 1.0 eV, respectively. For the small system the broadening was increased to 200 meV in order to obtain a sufficiently smooth curve. The range for the fit was chosen from 1.7 to 3.2 eV.

the distinct peaks disappeared. This resembles more the experimental findings [81, 82], even though the contribution of sub-gap absorption is still overestimated. The value of the optical gap is not affected by the averaging (Tab. 3.3).

As compared to the experimental values, the optical gaps determined via Tauc plots are clearly too small, despite the application of quasiparticle corrections. The results are, however, consistent with the results obtained for the mobility gaps in the sense that the gap in the large system is about 0.2 to 0.3 eV larger than in the small system. Moreover, the Tauc gap is slightly smaller than the mobility gap for all cases, which agrees with the experimental findings (Tab. 3.3).

3.5.3 JDOS and optical matrix elements

On the microscopic level the optical properties are determined by the probabilities of valence band electrons being excited to a conduction state under photon absorption. These probabilities depend on the optical coupling between the initial and the final states, given by the optical transition matrix element v_{cv} . The probabilities of all transitions at a given energy E are summarized in the average coupling strength $\langle v^2 \rangle$ as defined in sec. 2.3.6, while their number is given by the JDOS. Both quantities together define the absorption spectrum and therefore have to be considered in the microscopic analysis of the absorption. This analysis is restricted to the large configuration, since the small configuration does not provide enough data to obtain reliable statistics.

To begin with, we investigate the JDOS, shown in Fig. 3.16. In the energy range up to 5 eV

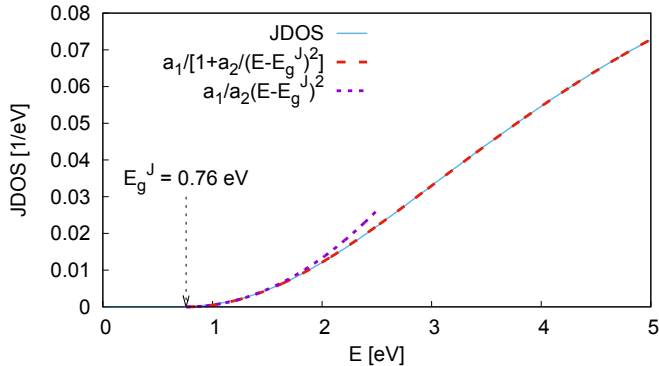


Figure 3.16: Normalized joint density of states (JDOS) for the large configuration. Fitting a function of the form $a_1/[1+a_2/(E-E_g^J)^2]$ (red dashed line) yields a value of $E_g^J = 0.76$ eV for the optical gap. Close to E_g^J (in a range of about 1 eV) the JDOS can be approximated quadratically (purple dotted line), which is the common assumption being made when determining the optical gap. [6]

displayed here, J can be well described by a function of the form

$$J(E) \approx \frac{a_1}{1 + a_2/(E - E_g^J)^2}, \quad (3.1)$$

where the a_i are fitting parameters. Fitting this function to the data yields a value of $E_g = 0.76$ eV for the optical gap, which, in distinction from the Tauc gap, we label E_g^J . Close to E_g^J the function becomes approximately $a_1/a_2(E - E_g^J)^2$. This agrees with the commonly made assumption that the density of band states increases as \sqrt{E} from the band edges [58], resulting in a quadratic energy dependence for the JDOS. The approximation however only holds in a small energy range of about 1 eV above the gap.

The average optical coupling strength is shown in Fig. 3.17. Above ≈ 0.9 eV, where transitions between localized states do not play a role, the data can be described by

$$\langle v^2 \rangle (E) \approx \frac{b_1}{(E - E_g^J)^3 + b_2/(E^2 + b_3)}, \quad (3.2)$$

where the b_i are fitting parameters. In the vicinity of E_g^J this function becomes $b_1/b_2(E^2 + b_3)$, where b_3 is of the order of 3 eV². This result clearly contradicts the common assumption that $\langle v^2 \rangle$ is constant at low energies [58]. This was disproven experimentally already by Jackson et al. [59], who however stated that instead $\langle v^2 \rangle \propto E^2$, which also disagrees with our results. However, the energy range in which an E^2 behavior is displayed in the experiment is rather small, which, combined with the comparably large error estimates in the fitting range, would allow also alternative interpretations of the measurement results. It therefore remains unclear if the disagreement in E dependence is due to an actual discrepancy between measurement and simulation, or arises rather from a different interpretation of the results. Good agreement with the experimental findings on the other hand is reached at high energies, where we find

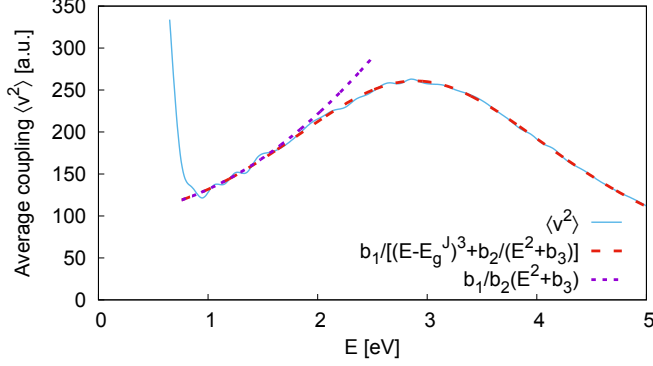


Figure 3.17: Average optical coupling strength $\langle v^2 \rangle$ as a function of the transition energy. Above ≈ 0.9 eV (i.e., at energies where transitions between localized states do not play a role) the average coupling can be described by a function of the form $b_1/[(E - E_g^J)^3 + b_2/(E^2 + b_3)]$ (red dashed line). This means that close to E_g^J (in a range of about 1 eV) the average coupling has the form $\langle v^2 \rangle(E) \propto E^2 + b_3$ (purple dotted line), then assumes a maximum at $E \approx 2.9$ eV, and falls off like $1/E^3$ at high energies. Below 0.9 eV the coupling is strongly increased due to transitions between localized states (cf. Fig. 3.20). [6]

that $\langle v^2 \rangle$ falls off like $1/E^3$. Also the position of the peak near the direct c-Si band gap, which is ≈ 2.6 eV in GGA-DFT, agrees with the experimental result.

We will now revisit the determination of the optical band gap. The assumptions behind the Tauc fit are $J(E) \propto (E - E_g)^2$ and $\langle v^2 \rangle$ constant near the gap, i.e., $\epsilon_2 \propto (E - E_g)^2/E^2$ and therefore $E\sqrt{\epsilon_2}$ becomes linear and yields the optical gap. From equations (3.1) and (3.2) we see however that $E\sqrt{\epsilon_2} \propto (E - E_g^J)\sqrt{E^2 + b_3}$ near E_g^J , which increases super-linearly (unless $b_3 \gg E_g^{J2}$, which is not the case here). As shown in Fig. 3.18, a linear fit to $E\sqrt{\epsilon_2}$ will therefore always yield a gap E_g^ϵ that is slightly larger than the value E_g^J obtained from the JDOS, where the difference increases with the fitting range. This is supported by the experimental results of Jackson et al. [59] who obtain 1.82 eV from fitting the DOS, and 1.86 eV from fitting $E\sqrt{\epsilon_2}$. The discrepancy between E_g^ϵ and our Tauc gap of 1.0 eV reported above can be explained with the fact that $\sqrt{\alpha E}$ is only approximately proportional to $E\sqrt{\epsilon_2}$ because the refractive index n in the formula for the absorption coefficient (2.129) is also energy dependent. Also, a larger fitting range of about 3 eV was used in the Tauc fit, which is problematic because the quadratic approximation for the JDOS holds only up to $\approx E_g^J + 1$ eV as stated before. The reason why it still gives sensible results is that the errors in the assumptions for J , $\langle v^2 \rangle$, and n approximately compensate [59]. Nevertheless, the problem of identifying the correct regime for the Tauc fit remains and imposes a large uncertainty on the determination of the Tauc gap. This is demonstrated in Fig. 3.19, where the Tauc gap is exemplarily determined for the IP spectrum in the configurational average, applying different fitting ranges. In each of the fitting ranges, $\sqrt{\alpha E}$ behaves in good approximation linear, but the resulting Tauc gaps differ by as much as 0.3 eV, where the highest value is only slightly higher than the value of E_g^T reported above, whereas the lowest value is as small as E_g^J . In addition, as mentioned before, a large broadening is needed to fit the absorption spectrum for small structures. As

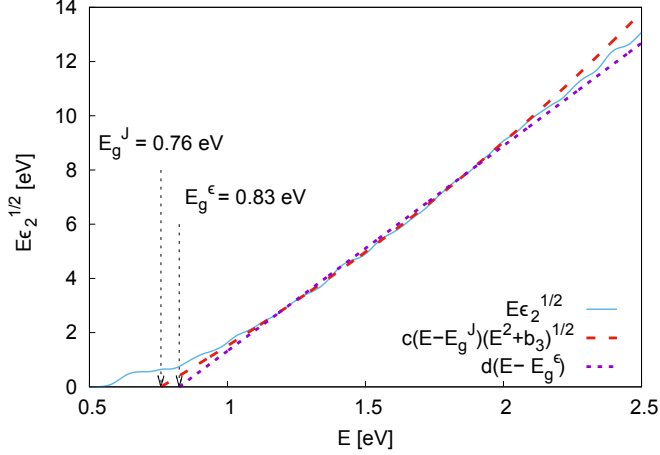


Figure 3.18: Determination of the optical gap from the dielectric function ϵ_2 . According to the fits of J (Fig. 3.16) and $\langle v^2 \rangle$ (Fig. 3.17), $E\sqrt{\epsilon_2}$ (blue solid line) assumes a form $\propto (E - E_g^J)\sqrt{E^2 + b_3}$ close to E_g^J (red dashed line). The determination of the optical gap from a linear fit, which implies $E\sqrt{\epsilon_2} \propto E - E_g$ (purple dotted line), therefore leads to a slightly larger value $E_g^\epsilon = 0.83$ eV. [6]

opposed to the Tauc fit, the proposed fit of the JDOS describes the data in the whole energy range of interest, making the result for E_g^J virtually independent of the fitting range, without increasing the broadening. This suggests that E_g^J is better suited to compare numerical results for the optical gap than E_g^T .

Another point of interest in the context of understanding and modeling absorption is the question, whether different types of transitions exhibit a different behavior, and if the transition probability also depends on the properties of the initial state. To address these issues, states are separated in localized and extended states, distinguished by a threshold of $S = 20.7 \text{ \AA}$ for the spread. $\langle v^2 \rangle$ is then calculated separately for each kind of transition: extended to extended, localized to extended and vice versa, and localized to localized. The result is shown in Fig. 3.20. We see that there is no qualitative difference for extended-extended and extended-localized transitions, in agreement with the experimental findings [59]. Localized-localized transitions however show a significantly higher coupling below ≈ 0.9 eV. As these transitions dominate at low energies, this also leads to a large increase of the total coupling, as can be seen in Fig. 3.17.

The anomalous energy dependence of the coupling between localized states, which is significantly enhanced, but only at low energies, suggests that the transition probability does not only depend on the energy of the transition, but also on the respective states. In order to investigate this dependence, we generalize the definition for the average coupling such that instead of taking the average over all transitions with a given transition energy E , we average over all transitions with any given property. As an example, $\langle v^2 \rangle$ is calculated as a function of the valence and the conduction state energy (Fig. 3.21). The plot shows that, even though brighter

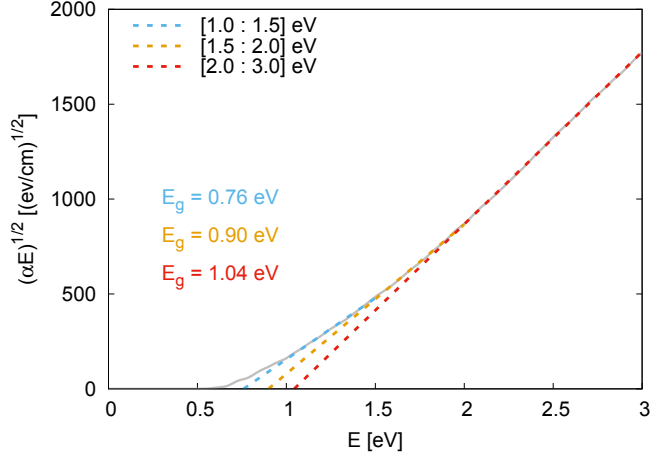


Figure 3.19: Tauc fit for the configurational average in the IP approximation. The different dotted lines refer to different fitting ranges, resulting in different values for the Tauc gap. The values vary between 0.76 and 1.04 eV, showing that E_g^T is highly sensitive to the choice of the fitting regime.

Table 3.3: Optical gaps (in eV) according to different definitions, obtained from fitting the JDOS, the imaginary part of the dielectric function, and the absorption spectrum. Each value is given without (IP) and with quasiparticle corrections in the GW and the scissors shift (SS) approximation, respectively. (Values in brackets were obtained with a very high broadening of 200 meV in order to have sufficiently smooth curves for fitting, and should therefore be taken with care.) Additionally, the mobility gaps are listed.

Fitted quantity	Fit function	Small system		Large system		Conf. avg.		Exp. [59]
		IP	GW	IP	SS	IP	SS	
JDOS	$c_1/[1 + c_2/(E - E_g)^2]$	0.51	0.88	0.76	1.06	0.76	1.06	1.82
$E\sqrt{\epsilon_2}$	$c \cdot (E - E_g)$	(0.56)	(0.79)	0.83	1.10	0.83	1.09	1.86
$\sqrt{\alpha E}$	$c \cdot (E - E_g)$	(0.79)	(1.04)	1.02	1.28	1.02	1.29	1.83
Mobility gap		0.83	1.26	1.09	1.46	1.13	1.51	1.93

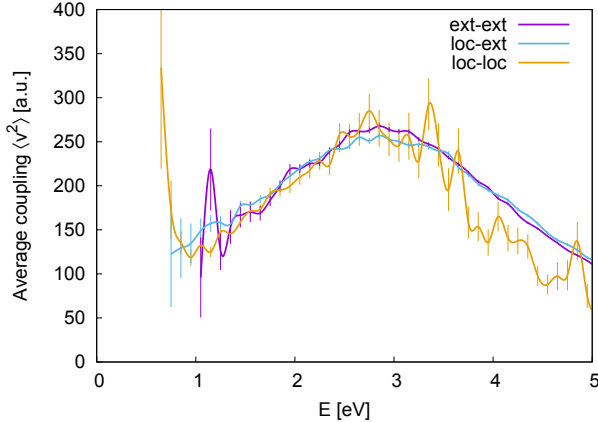


Figure 3.20: Average optical coupling strength $\langle v^2 \rangle$ resolved by type of state. A spread of $S = 20.7 \text{ \AA}$ is used to distinguish localized from extended states. The error bars indicate the standard deviation of the average. The plot shows no difference in the qualitative behavior for the coupling of two extended states, and the coupling between an extended and a localized state, respectively. The coupling between two localized states is significantly stronger only at $E \lesssim 0.9 \text{ eV}$ and is the sole reason for the increase of the total coupling seen in Fig. 3.17. [6]

spots do exist at the highest valence state, there is no general dependence on E_v and E_c , but only on the energy difference E . On the other hand, a correlation with the localization can be found when plotting $\langle v^2 \rangle$ as a function of the valence-state spread and the transition energy. For strongly localized valence states the coupling seems to be much stronger than for weakly localized and extended states, where $\langle v^2 \rangle (S_v)$ becomes approximately independent of S_v . Due to the small number of these states, this effect however becomes visible in the average $\langle v^2 \rangle (E)$ only at very low energies, where transitions involving strongly localized states dominate. The observation made above, that the probabilities for extended-extended and extended-localized transitions do not differ on average, therefore remains valid.

3.6 Conclusions

We used model configurations of a-Si:H with 72 and 576 atoms, respectively, generated with ab initio molecular dynamics, as a starting point for the electronic and optical characterization of a-Si:H from first principles. The structural, electronic, and optical properties of the present configurations were calculated on the DFT level and subsequently analyzed.

The structural characterization in terms of the radial pair correlation function and the bonding analysis, based on the electron localization function, revealed a high degree of short-range order. Especially the larger configurations, which were found to be defect-free, present a good approximation of real a-Si:H, qualifying them as a promising starting point for a full ab initio

description of a-Si:H that allows to reproduce the experimental properties.

The analysis of the density and localization of states confirmed the results of the structural analysis in the sense that a high number localized mid-gap states were found in the small configuration that could be clearly attributed to dangling bonds. On the other hand, only few localized states were present in the large configuration. These states exist even in the absence of dangling bonds and appear to be related to weakly bonded atoms, whereas the length of the bonds does not have a direct effect on the localization. This suggests that the geometry of the configuration alone does not allow conclusions about the existence and density of localized states.

For the purpose of obtaining macroscopic properties that can be used to compare our numerical results to experimental data, we calculated absorption spectra, as well as optical and mobility gaps. Qualitatively good spectra were obtained with taking the computational average over 10 large configurations, even though sub-gap absorption was overestimated due to a yet too high defect state density. The values for the optical and mobility gap obtained from DFT were, however, strongly underestimated, which could be partially related to finite-size effects. We found that the size of the super cell does not only affect the results indirectly, via the defect state density, but also has a direct effect on the localization and thus on the value and the uncertainty of the mobility gap. In particular, a larger super cell improved the values we calculated for the mobility gap and the optical gap by 0.2 to 0.3 eV.

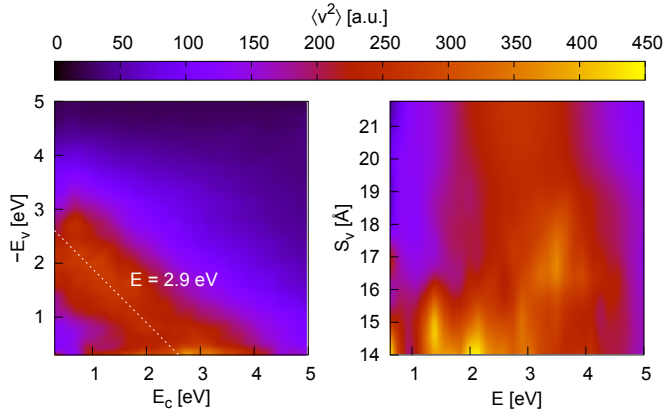


Figure 3.21: **Left:** $\langle v^2 \rangle$ as a function of the conduction state energy E_c and the valence state energy E_v (with respect to the Fermi level). The white diagonal indicates the line of constant transition energy E where $\langle v^2 \rangle(E)$ has a maximum. Along the lines of constant E the coupling does not vary much, showing that the coupling between two states does not depend significantly on the energies E_v and E_c , but mostly on the difference $E = E_c - E_v$. **Right:** $\langle v^2 \rangle$ as a function of the valence state spread S_v and the transition energy E . Coupling is particularly strong at all energies for strongly localized states, whereas for weakly localized and extended states it becomes almost independent from the localization. [6]

In an attempt to bridge the discrepancy between calculation and experiment we performed G_0W_0 calculations for the 72-atom a-Si:H configuration, finding that the quasiparticle corrections can be approximated by a scissors shift. This approximation makes calculations for larger - and thus physically more representative - configurations possible. The extracted set of scissors-shift parameters was used for calculating quasiparticle corrected absorption spectra and gaps for all configurations, which lead to an improvement by roughly 0.3 to 0.4 eV, but could not completely close the gap to the experimental values.

The discrepancy between the calculated and the experimental gaps is in contradiction to the good agreement of the structural properties, which suggests that it could be a computational artifact. One candidate for causing this are the finite size effects, which were demonstrated and discussed qualitatively, and which might be eliminated by making the super cell large enough. The other potential source of error is the negligence of quasi-particle effects on the wave functions in the G_0W_0 calculations, where only the energies are corrected. Quasiparticle corrections to the wave functions might change their localization and hence increase the mobility gap. Also the inclusion of higher-order energy corrections within a fully self-consistent GW calculation could further improve the results.

Finally, we analyzed the absorption in a-Si:H on the microscopic level in terms of the JDOS and the optical transition matrix elements. Our results agree with experiment in that the average transition probability decreases with $1/E^3$ at high energies, and that it does not differ for transitions between two extended states and transitions between a localized and an extended state, respectively. Nevertheless, strong localization does seem to increase the transition probability, but the effect is macroscopically not visible due to the small number of strongly localized states. Concerning the often discussed energy dependence of the matrix elements near the gap, we find a dependence $E^2 + c$ with some constant c . This disagrees with the common assumption of constant matrix elements, but also with the E^2 dependence suggested in the literature.

4 The a-Si:H/c-Si interface

In this chapter the structural and electronic properties of the amorphous/crystalline silicon (a-Si:H/c-Si) interface under high-temperature annealing are calculated and analyzed with *ab initio* methods. The first section provides an overview over the applications and resulting questions, the problems related to modeling the interface, the proceedings in the field so far, and the goals of the present work. The second section describes the technical details of the structures used and of the computations. The subsequent sections present the results, consisting of a detailed analysis of a single configuration, and an investigation of the effects of both the high-temperature annealing and the surface passivation on the key properties. The results are summarized and discussed in the final section.

4.1 Introduction

The silicon heterojunction (SHJ) technology holds the current efficiency record of 26.6% for silicon-based single junction solar cells [83] and shows great potential to become a future industrial standard for high-efficiency crystalline silicon cells. At the heart of this technology is the a-Si:H/c-Si interface, formed by a thin layer of hydrogenated amorphous silicon (a-Si:H) passivating the crystalline silicon (c-Si) surface. The physical processes occurring at this interface have crucial impact on the characteristics of the entire photovoltaic device. The key to improving the solar cell performance lies therefore in the optimization of the interface, in particular with respect to its transport and recombination properties. This optimization requires a profound understanding of the underlying physical mechanisms and of the structure-property relations, in order to accurately predict how changes in the atomic structure affect the microscopic electronic properties and, ultimately, the macroscopic cell characteristics.

In order to arrive at a predictive *ab initio* simulation of the a-Si:H/c-Si interface, essentially three steps have to be taken. First, a model atomic interface structure has to be generated that exhibits the experimentally observed structural features. Hence, this structure must be large enough to be physically representative and to eliminate finite-size effects as discussed in the previous chapter, while still being treatable with *ab initio* methods; it should be almost free of defects, since, due to the limited number of atoms in an *ab initio* calculation, already few defects lead to a strong overestimation of the gap-state density, possibly even resulting in metallic behavior; and furthermore, unphysical surface effects resulting from the very small layer thicknesses should be minimized. Second, the electronic structure has to be calculated and analyzed with focus on the identification and characterization of localized states at the interface, which have a crucial impact on the device performance due to their role as recombination centers [84–86]. For that purpose proper characterization tools need to be chosen and developed. Third, the relevant band parameters, such as band gaps and offsets, as well as local material properties associated with the carrier dynamics, such as mobility and lifetime, are to be extracted based on the microscopic information. The band offset describes the offset between the valence and conduction band edges, respectively, of the two materials, in this case c-Si and a-Si:H. It is one of the most important characteristics of a heterojunction for

application in photovoltaics, as it has a crucial influence on the transport and recombination properties of the interface.

Some advances have been made towards a full ab initio description of the a-Si:H/c-Si interface in the recent years [54, 71, 87–90]. Most of the structures in these works were however generated with classical or tight-binding molecular dynamics (MD), and suffered from high defect densities. Structures generated entirely with ab initio molecular dynamics have been reported only recently by Jarolimek et al. [54], who achieved low defect densities by applying a long high-temperature annealing. Using hybrid density functional theory (DFT), they also obtained reasonable values for the conduction and valence band offsets, however employing the bulk value for the c-Si band gap. Other studies focused on the analysis of the defect structure, in particular with respect to the surface orientation of the c-Si layer [71, 90]. Also the origin of localized states has been discussed [89, 90], although, to the best of our knowledge, a quantitative description of electron localization exists so far only for bulk a-Si:H [6, 56, 65].

The interface structures used in this work were composed from bulk c-Si and a-Si:H using ab initio MD. The problem of generating a physically realistic bulk a-Si:H structure has been discussed in the previous chapter, whereas here we will focus on the description of the interface as a whole. The interface structure is annealed at different temperatures ranging from 300 to 900 K, resulting in a configuration with almost no defect states inside the gap. Throughout the annealing process, we monitor the evolution of the relevant structural and electronic properties, such as the defect distribution, the density of states, and the band gaps. In this way, insight is gained on how and why these properties change under high-temperature annealing, which apparently plays an important role in reducing defect densities. Also the role of hydrogen passivation both at the interface and the surface is investigated. Among all the calculated configurations the one with the lowest density of gap states is identified. On this configuration, a detailed analysis of the electronic structure is performed, including a classification of individual electronic states in terms of their energy, localization, and location. This classification also gives rise to an alternative method of determining the band gaps and offsets directly from the interface structure without the need to resort to bulk values.

4.2 Computational details

The a-Si:H/c-Si structures analyzed in this work consist of two parts, one layer of crystalline silicon (c-Si) and one layer of hydrogenated amorphous silicon (a-Si:H). The crystalline part was obtained by first generating a c-Si layer with a Si(001) surface and an equilibrium lattice constant of $a_0 = 5.47 \text{ \AA}$ (Fig. 4.1(a)), and then replacing the ideal surface by a reconstructed symmetric $p(2 \times 1)$ surface, which emerges from surface atoms forming pairs, thus reducing the number of dangling bonds by half (Fig. 4.1(b)). Relaxation of the top four layers resulted in relative changes of the layer spacings d_{ij} between layers i and j by $\Delta_{12} = -21.4\%$, $\Delta_{23} = 0.21\%$, and $\Delta_{34} = 0.13\%$ with respect to the bulk spacing $d_0 = a_0/4$. The amorphous part was obtained by cutting the 576-atom a-Si:H structure described in the previous chapter to match the surface area of the c-Si layer. The two layers were then placed together in the simulation cell to form an a-Si:H/c-Si interface, where the c-Si side of the interface is constituted of the reconstructed surface. The distance between the two layers thereby corresponds to the total

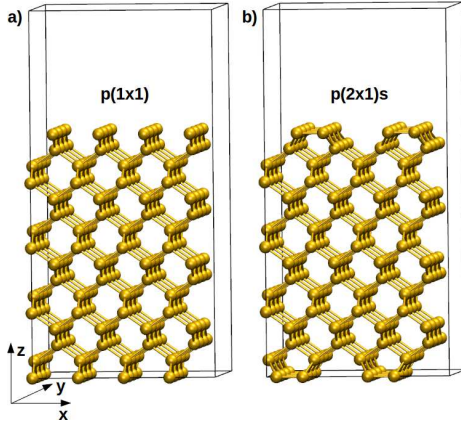


Figure 4.1: (a) The unreconstructed (ideal) Si(001) surface and (b) the reconstructed symmetric $p(2 \times 1)$ Si(001) surface in the simulation box. The reconstructed surface is obtained by dimer formation of the surface atoms, and subsequent relaxation of the spacing between the top four layers. The simulation cell is tetragonal and consists of 256 Si atoms and a 10 Å vacuum layer. Periodic boundary conditions are used in all three directions. [7]

energy minimum. The crystalline part consists of 192 Si atoms, and the amorphous part of 128 Si and 16 H atoms. A void region of 10 Å in z -direction was inserted to suppress the interaction between the periodic images. In order to avoid surface effects, the free surface of the c -Si layer is passivated with 32 H atoms. The total length of the system is $L_z = 38.66$ Å, while in the x - and y -direction the system has an extent of $L_x = L_y = 15.46$ Å. Periodic boundary conditions are imposed in all directions.

The interface configuration constructed in this way was used as a starting point for Born-Oppenheimer molecular dynamics simulations on the GGA-DFT level at constant volume and constant temperature (NVT), where the first four layers of c -Si atoms were kept fixed to impose a bulk-like behavior to the c -Si part of the system. The system was first thermalized at 300 K for ~ 37 ps (Fig. 4.2), before being subjected to a high-temperature annealing consisting of 60 ps at 300 K, and 40 ps each at 500 K, 700 K, and 900 K. At the end of this, the a -Si:H surface was passivated with an additional 10 H atoms, followed by another annealing at 1100 K.

The generation and annealing of the interface configuration was not part of this work and is therefore not described in detail here. The respective information can however be found in a previous publication [7].

The electronic structure is calculated within density functional theory (DFT) using the PWscf code of the Quantum ESPRESSO package [75, 76] with norm-conserving pseudopotentials and a PBE-GGA functional [24]. The Brillouin-zone integration for the self-consistent calculation of the charge density is carried out on a $2 \times 2 \times 1$ k -point grid and with a Gaussian smearing of 0.01 Ry. This smearing is necessary to reach convergence due to the existence of defect states at the Fermi level. The plane wave cut-off energy is set to 30 Ry in all calculations. All the

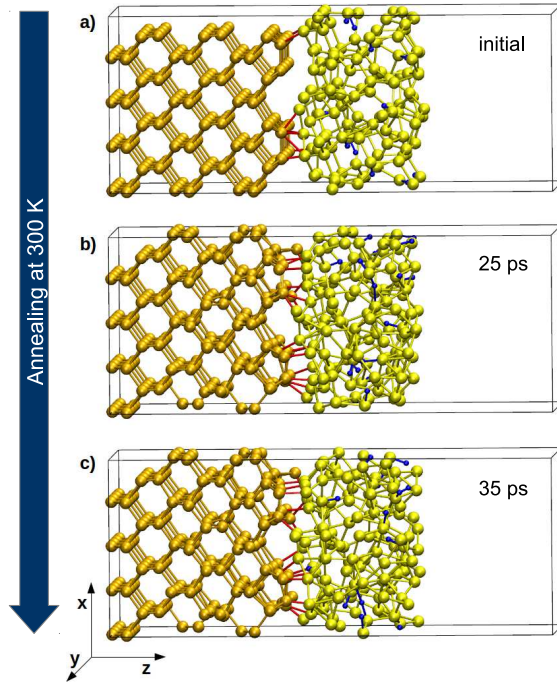


Figure 4.2: Snapshots of the c-Si/a-Si:H interface in the simulation box. The structure consists of a crystalline part with 192 Si atoms, an amorphous part with 128 Si and 16 H atoms, and a vacuum layer of about 10 Å, in a super cell with periodic boundary conditions. H atoms and bonds with Si atoms are blue, Si atoms and their bonds are dark yellow in the c-Si part, and light yellow in the a-Si:H part. Bonds connecting the c-Si and the a-Si:H part are red. Shown is the initial configuration (a), and the configuration after 25 ps (b) and 35 ps (c) of annealing at 300 K. Throughout the annealing the atoms at the interfaces move closer together and form bonds between the c-Si and the a-Si:H part. [7]

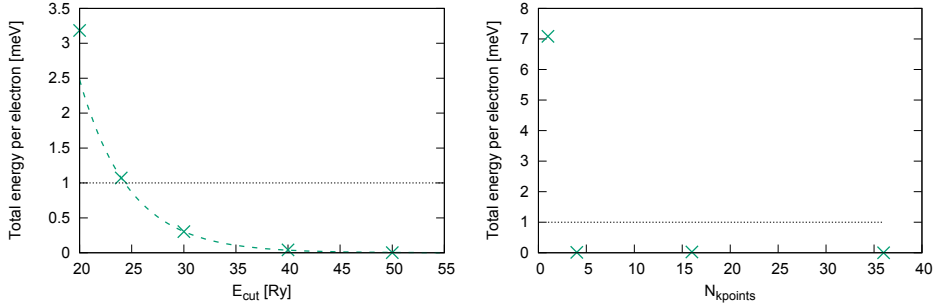


Figure 4.3: Convergence behavior of the total energy per electron w.r.t. the plane-wave cut-off E_{cut} (left) and the number of \mathbf{k} -points in the first Brillouin zone (right). W.r.t E_{cut} , the total energy converges exponentially, as indicated by the dashed line, which represents an exponential fit of the data points. The extrapolation to $E_{\text{cut}} \rightarrow \infty$ is used as the reference energy. At 30 Ry the system is converged to this energy within 1 meV per electron (indicated by the horizontal line). For the \mathbf{k} -point convergence, the energy for the largest tested grid is used as reference. Convergence is assumed if the total energy per electron differs by less than 1 meV from the previous data point. This is the case for four ($2 \times 2 \times 1$) points.

parameters were chosen by checking the convergence of the total energy of the system (Fig. 4.3). The non-self-consistent calculation of the electronic states is performed on a $4 \times 4 \times 1$ \mathbf{k} -point grid, which was found to yield a sufficiently accurate representation of the relevant quantities, such as density of states (DOS), electron localization function, and spread. A gaussian broadening of 50 meV is used for displaying the layer-resolved DOS.

4.3 Structural and electronic properties

This section describes the characterization of the atomic and electronic structure of the a-Si:H/c-Si interface and the extraction of the band gaps and offsets from the microscopic structure. As an example we use the configuration obtained at the end of the 700 K annealing, which was found to be the configuration with the lowest defect-state density.

4.3.1 Atomic structure

The atomic structure after annealing at 700 K is shown in Fig. 4.4(a). Despite the distortion of the crystalline structure near the interface, which makes the transition from the crystalline to the amorphous part less sharp, the two parts can still be easily distinguished. Moreover, the $p(2 \times 1)$ character of the crystalline side of the interface is still recognizable due to the fact that each atom on the crystalline side forms only one bond with the amorphous side.

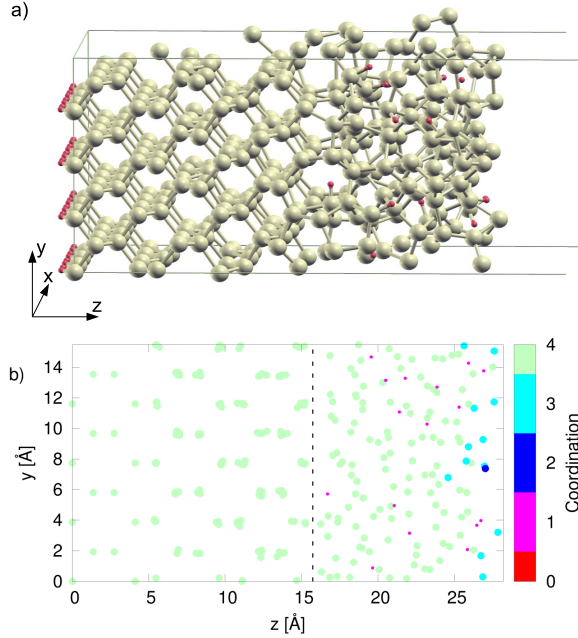


Figure 4.4: (a) Atomic structure in the simulation cell after 40 ps of annealing at 700 K. Si atoms are beige, H atoms red. The crystalline side of the interface retained its $p(2 \times 1)$ character but became increasingly disordered, smearing out the transition between c-Si and a-Si:H. (b) Projection of the atomic positions onto the yz -plane. The color indicates the coordination number according to the ELF criterion. All Si atoms (big dots) in the crystalline part and at the interface (dashed line) are four-fold coordinated. Dangling bonds exist only at the free a-Si:H surface. All H atoms (small dots) are bonded to exactly one Si atom. [7]

Whereas for the drawing of the bonds in Fig. 4.4(a) a simple cut-off radius was applied, a more sophisticated analysis of the bonding using the method described in sec. 2.3.2 was performed in Fig. 4.4(b), where the coordination numbers of all atoms in the configuration are visualized. The plot shows that the interface is completely defect free, and that under-coordinated Si atoms can be found only at the free surface of the a-Si:H layer. The analysis of the Si-H bonds shows that all H atoms are bonded to exactly one Si atom, in agreement with the expectation on physical grounds.

4.3.2 Density of states and band offsets

In order to calculate the band offsets at the interface we first need to obtain the valence and conduction band edges for the two layers. This requires the choice of a definition for the gap both in the a-Si:H layer, where a classical band gap does not exist, and in the c-Si layer, where the crystalline band structure is distorted due to the symmetry breaking in z -direction.

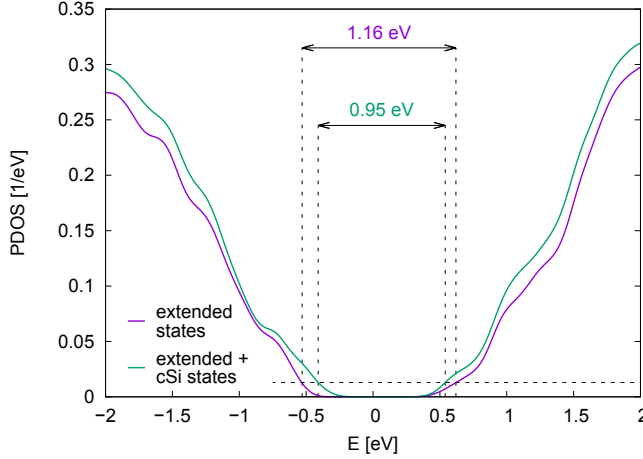


Figure 4.5: Partial density of states (PDOS) at the end of the 700 K simulation. E_g^{mob} is determined from the extended states ($S_z > 26.1 \text{ \AA}$) only (purple line), as described in sec. 2.3.5, and E_g is determined from the states localized in the c-Si layer ($\langle z \rangle < 13 \text{ \AA}$, green line). From the intersections of the PDOS with the threshold D_t (horizontal line), we obtain $E_g^{\text{mob}} = 1.16 \text{ eV}$ and $E_g = 0.95 \text{ eV}$. The valence band offset is 0.13 eV and the conduction band offset 0.08 eV, in qualitative agreement with experimental observations [91] and hybrid DFT calculations [54].

A method suggested in the literature [54], where the local DOS is integrated over the crystalline and amorphous layer, respectively, and is then used to extract the c-Si band gap and the Tauc gap [58], was tested and was found to have two major drawbacks. First, due to the rather low thickness of the layers, localized states decaying into the neighboring layer can strongly affect the results for the gaps. Second, a Tauc fit works only if the DOS is sufficiently smooth, which requires either a very high broadening, distorting the results, or an averaging over a large number of configurations. Even then, the result was found to be highly sensitive to the fitting ranges applied, as already discussed for bulk a-Si:H in the previous chapter.

Here we employ an alternative method that determines the offsets from the mobility gap, being the more relevant quantity in the context of charge transport, and the band gap, both defined via the partial density of states. This method allows for the determination of the gaps of an individual configuration without the need for averaging, and it ensures that the value of E_g is not affected by localized interface or a-Si:H states decaying into the c-Si layer.

The mobility gap E_g^{mob} is determined via the spread according to the procedure described in sec. 2.3.5, with the only difference that here we are interested in the mobility across the interface, and therefore only the spread S_z in z -direction is considered. The threshold S_t for separating extended and localized states depends on the extent of the structure, which may vary, and therefore has to be defined individually for each configuration. This is done such that 95% of the valence band states between 2 and 4 eV below the Fermi level (to exclude tail and low lying localized states) exceed S_t , which in this case gives $S_t = 26.1 \text{ \AA}$. The resulting

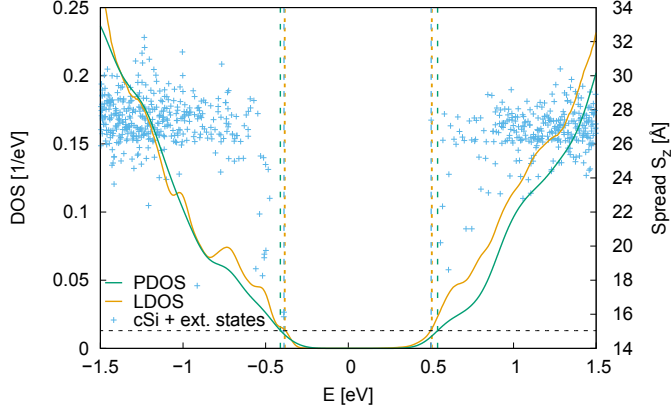


Figure 4.6: Determination of the c-Si band gap inside the crystalline layer. The points represent the energy and spread of extended states ($S_z > 26.1 \text{ \AA}$) and states localized inside the crystalline layer ($\langle z \rangle < 13 \text{ \AA}$). The partial DOS (PDOS) generated by these states is shown by the green line. The orange line shows the local density of states (LDOS) integrated over the third and fourth atomic layer. Both densities are normalized. The green and orange vertical (dashed) lines indicate the band edges obtained from the intersections of the respective DOS with the threshold D_t (horizontal line). The blue vertical (dashed) lines indicate the highest occupied and lowest unoccupied state in the c-Si layer.

density of extended states is shown in Fig. 4.5.

The band gap E_g of the crystalline part of the structure is determined the same way, but including in the partial density of states (PDOS) also states localized inside the c-Si layer, defined by $\langle z \rangle < 13 \text{ \AA}$, where $\langle z \rangle$ is the mean position of the electron. The resulting PDOS is shown in Fig. 4.5. In order to compare this definition of the band gap with other possible definitions, Fig. 4.6 shows the PDOS together with the relevant states and with the local DOS (LDOS) integrated over the third and fourth atomic layer, i.e., far away from the interface. Both densities are very similar for the valence states, giving the same valence band edge. For the conduction states, however, the LDOS is slightly higher, resulting in a lower conduction band edge. This is due to interface states extending far into the crystalline part (cf. Fig. 4.7), which is a problem of the small thickness of the c-Si layer. The exclusion of interface states tries to minimize this effect, but depends on the correct classification of states. Using the PDOS instead of simply taking the energy difference between the lowest unoccupied and the highest occupied c-Si state reduces the sensitivity of the band gap to wrong classifications and small changes in the electronic structure, while giving a slightly higher value ($\sim 0.1 \text{ eV}$) for E_g .

From Fig. 4.5 the c-Si band gap is found to be $E_g = 0.95 \text{ eV}$, and the a-Si:H mobility gap to be $E_g^{\text{mob}} = 1.16 \text{ eV}$. The valence band offset is $\Delta E_v = 0.13 \text{ eV}$ and the conduction band offset $\Delta E_c = 0.08 \text{ eV}$. The values for both gaps are higher than the bulk values obtained in GGA-DFT calculations, which are about 0.6 eV in c-Si [52], and between 0.8 and 1.1 eV in a-Si:H, as reported in the previous chapter. They however underestimate the experimental

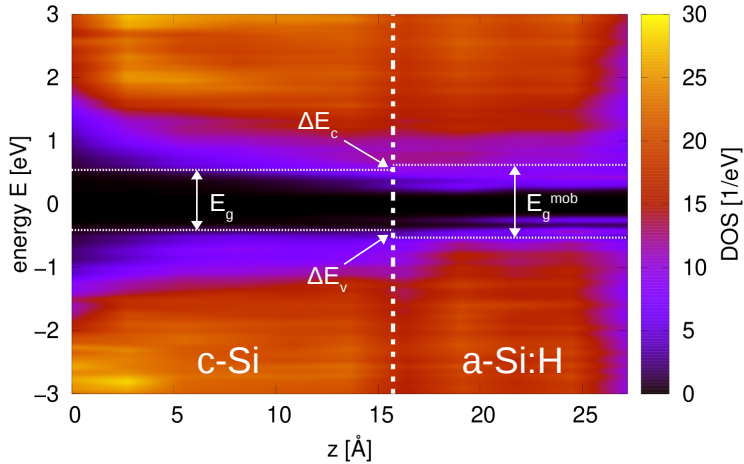


Figure 4.7: Local DOS integrated over layers parallel to the interface at the end of the 700 K simulation. The vertical dashed line marks the approximate position of the interface, the horizontal lines indicate the band edges. Localized states inside the mobility gap can be seen in the a-Si:H layer and near the interface, partially extending also into the c-Si layer, in particular close to the conduction band edge. At the left end the gap slightly widens due to the H-passivation of the back surface.

values, which are 1.1 eV for c-Si [92] and about 1.9 eV for a-Si:H [57, 59]. The discrepancy is higher for E_g^{mob} , which also results in an underestimation of the band offsets. Nevertheless, the finding that ΔE_v is larger than ΔE_c is in agreement with experiments, reporting valence band offsets between 0.27 and 0.40 eV [91, 93, 94] and conduction band offsets between 0.15 and 0.28 eV [91, 95], and with recent hybrid DFT calculations, finding $\Delta E_v = 0.29$ eV and $\Delta E_c = 0.17$ eV [54]. It must however be noted that the band offsets and their difference are of the same order of magnitude as the uncertainty in determining the band and mobility gap, which is approximated to ~ 0.1 eV. This makes the qualitative and quantitative comparison of the values with the experiment, but also with other calculations having probably similar error margins, very difficult.

In Fig. 4.7 the band edges and offsets are shown together with the layer-resolved DOS, which is obtained by integrating the local DOS over layers parallel to the interface. Left from the interface (represented by a vertical line), for $5 \text{ \AA} \leq z \leq 12 \text{ \AA}$, the DOS shows an approximately uniform crystalline behavior with a defined band gap. However, close to the conduction band edge there are states decaying into the c-Si layer, which explains the difference between the integrated LDOS and the PDOS that we noted before. As opposed to that, the gap near the valence band edge is completely free of states. In the vicinity of the interface, states start emerging also deep inside the gap. These localized states partially fill the mobility gap in the a-Si:H layer, giving a distinctly different picture of the DOS than in the c-Si layer. Also below the valence band edge the DOS is significantly increase as compared to the c-Si part, suggesting that there exists confinement also in the valence band. The widening of the gap at $z < 5 \text{ \AA}$ is an artifact of the H-passivation of the back surface.

4.3.3 Localized states

The existence, position, both energetical and spatial, and origin of localized states in the a-Si:H/c-Si interface is highly relevant in the context of photovoltaics due to their role in transport and as recombination centers. For a better understanding of their contribution to the electronic structure we analyze all states with a spread $S_z < 26$ Å in terms of their energy, the z -component of their mean position $\langle z \rangle$, and their spread S_z , which are plotted in Fig. 4.8. From this representation we see that localized and semi-localized states exist in all parts of the structure, but do not necessarily affect transport or recombination as they have energies far outside the gap. Localized gap states exist mainly inside the a-Si:H layer, but also close to the interface, where they lie energetically below the conduction band edge, supporting our previous findings. Also the existence of confined valence states both in the c-Si and the a-Si:H layer can be seen here. By closer inspection of individual states, different species of localized and semi-localized states can be distinguished, which are exemplarily labeled A to G and drawn in Fig. 4.8(b). More precisely, the figure shows for each wave function ψ the distribution of the probability density $|\psi|^2$ integrated over x and y along the z axis. In the following, these states shall be discussed one by one.

State **A** is an H-atom induced surface state. The wave function is strongly localized at the crystalline surface. The H-passivation of the surface atoms moves the surface states out of the gap and deep into the valence band, such that they do not affect the electronic structure near the Fermi level. State **B** is localized in the crystalline part and lies energetically right below the c-Si valence band edge. As it however lies inside the a-Si:H mobility gap, it can not extend into the a-Si:H and is therefore confined to the c-Si. The period length of the maxima and minima of the probability density ρ is double that of the crystal lattice, meaning that ρ has alternating maxima and minima at the atomic layers. The same can be seen in **C**, where the maxima and minima are however shifted by one atomic layer as compared to B. This leads to a small shift in energy, pushing the state below the mobility edge, and thus allowing it to extend into the a-Si:H and significantly increasing the spread. State **D** lies inside the valence band and is weakly localized right at the interface (vertical line). The wave function is rather delocalized over the whole structure but has peaks close to the interface. This could be a resonance effect due to the shape of the potential: in Fig. 4.9 it can be seen that the Kohn-Sham potential, averaged over the xy -plane, has a barrier at the interface. This barrier occurs due to the initial condition of a reconstructed surface, which leads to a reduced atomic density at the interface (cf. Fig. 4.4(a)). Even though the barrier is not high enough to induce confinement at energies higher than about -8.2 eV, it nevertheless does affect the electronic structure near the Fermi level. Another form of interface effects are intrinsic interface states, which, unlike interface resonances, have energies lying inside the gap, and are therefore, very much like dangling bond states, exponentially localized. Examples of these are the states **E** and **F**, which lie both deep inside the mobility gap, and have peaks at the interface, decaying roughly exponentially into both the c-Si and the a-Si:H layer. Since it was shown before that there are no dangling bonds at the interface (cf. Fig. 4.4(b)), these states are most probably intrinsic interface states. This means that even in the total absence of defects, localized states that can act as traps for non-radiative recombination can exist, only due to the symmetry breaking at the interface. Dangling bond states like **G**, which can clearly be associated with under-coordinated atoms, can be found only near the free a-Si:H surface. These states are strongly localized and lie deep inside the mobility gap. State **H** represents an extended state, which is delocalized over the

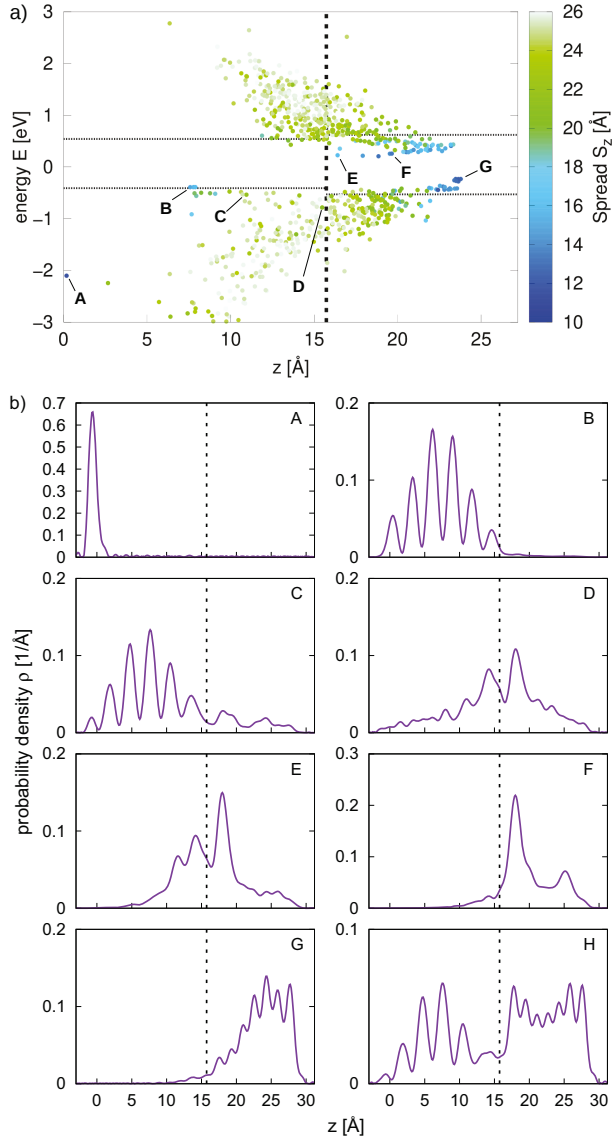


Figure 4.8: (a) Energy and localization of states with $S_z < 26 \text{ \AA}$ at the end of the 700 K simulation. Each dot marks the energy and the z -position of the center of one wave function, whereas the color represents its spread. The vertical dashed line marks the approximate position of the interface, the horizontal lines indicate the band edges. Different types of states can be distinguished, which are exemplarily labeled and drawn in Fig. 4.8(b). (b) Probability density along the z -direction integrated over the xy -plane for selected states indicated in Fig. 4.8(a). A: Surface state induced by H passivation. B: Confined c-Si state. C: c-Si state extending into amorphous part. D: Interface resonance. E and F: Intrinsic interface states. G: Dangling bond state. H: Delocalized state (not indicated in Fig. 4.8(a)). [7]

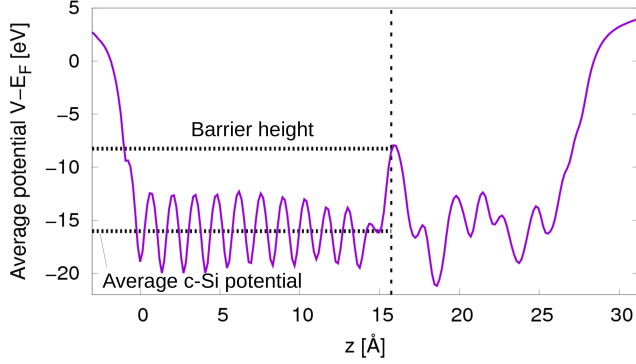


Figure 4.9: Kohn-Sham potential w.r.t. the Fermi level averaged over the xy -plane at the end of the 700 K simulation. The periodicity of the crystalline structure is clearly visible and vanishes only close to the interface (indicated by the vertical dashed line), where a potential barrier forms 8.2 eV below the Fermi level. The height of the barrier w.r.t. the average potential in the c-Si layer is 7.8 eV, indicated by the horizontal dashed lines. The barrier does not only cause confinement at low energies, but can also lead to interface resonances at energies above the barrier (cf. Fig. 4.8). [7]

whole structure. It does not appear in Fig. 4.8(a) because it cannot be assigned a position. The wave function consists of a c-Si part, showing the same periodicity as state **C**, and an a-Si:H part with almost homogeneous distribution. The minimum at the interface is due to the potential barrier.

4.4 Evolution upon high-temperature annealing

After introducing the relevant quantities characterizing the a-Si:H/c-Si interface structure on the example of a single configuration, we will now investigate how these quantities evolve upon the high-temperature annealing. This analysis will help to understand what happens to the defects in the annealing process, which role the hydrogen plays for the evolution of the defect density, and what is the effect on the electronic structure, in particular with respect to the band gaps and the gap states.

4.4.1 Structural evolution

In order to visualize the changes that the atomic structure undergoes throughout the generation and annealing process, the atomic positions (projected on the yz -plane) and coordination numbers are shown at different time steps in Fig. 4.10, namely for the initial configuration, after thermalization, i.e., before starting the high-temperature annealing, and at the end of each annealing step, i.e., at 300 K, 500 K, 700 K, and 900 K, respectively. In the initial state,

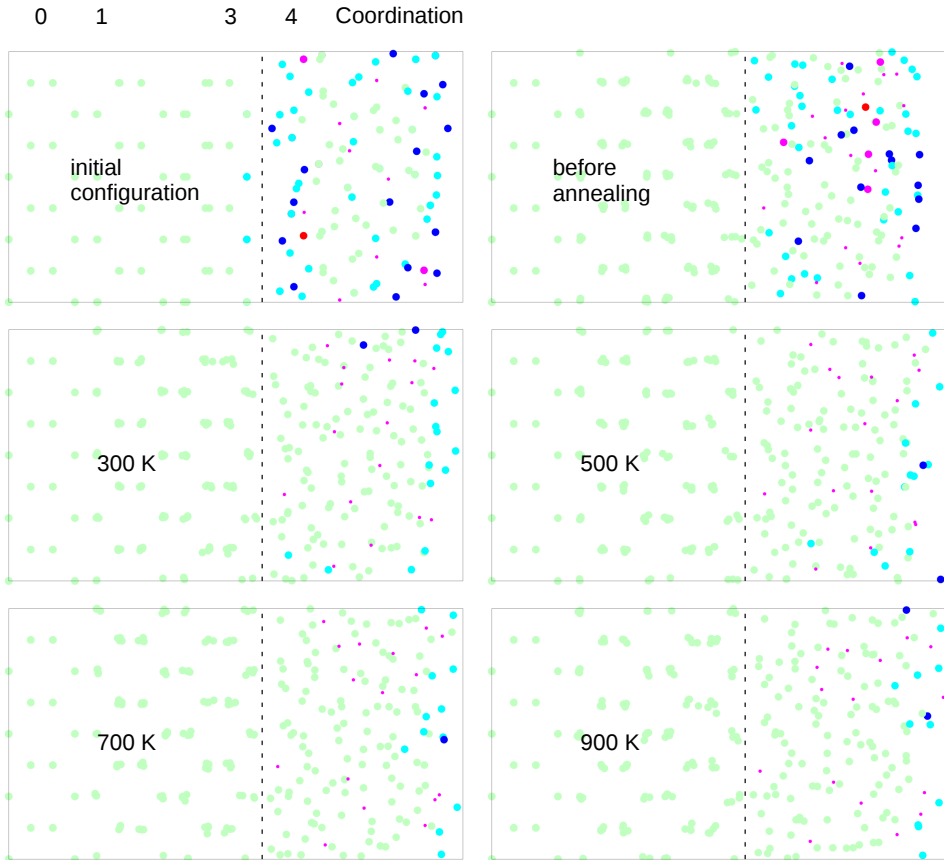


Figure 4.10: Atomic structure at different stages of the annealing process (initial configuration, prior to annealing, and after annealing at 300 K, 500 K, 700 K, and 900 K). The points represent projections of the atomic positions onto the yz -plane, where the color indicates the coordination number according to the ELF criterion. The dashed line marks the approximate position of the interface. During the thermalization prior to annealing the a-Si:H layer moves closer to the c-Si layer and new bonds form between the two layers, but the a-Si:H side of the interface remains highly defective. After annealing at 300 K the number of dangling bonds is already significantly decreased and keeps decreasing throughout the annealing, while at the same time the c-Si side of the interface becomes increasingly disordered. At 700 K defects exist only at the a-Si:H surface, and hydrogen starts accumulating there. Annealing at 900 K yields no further improvement.

the two layers of the interface are only weakly connected, meaning that not all the atoms at the c-Si surface are bonded to the a-Si:H layer. In addition, the a-Si:H layer is highly defective. During the thermalization prior to annealing the a-Si:H layer moves closer to the c-Si layer and new bonds form between the two layers, but the number of defects does not change notably. After annealing at 300 K the number of dangling bonds is significantly decreased, particularly near the interface. At 500 K the interface region is completely defect free and the number of dangling bonds is further decreasing. At 700 K defects exist only at the a-Si:H surface. Annealing at 900 K does not further reduce the amount of defects. Whereas the a-Si:H layer becomes more ordered (in the sense of less defective) throughout the annealing, the c-Si side actually loses its perfect crystalline order near the interface, blurring the transition between crystalline and amorphous part. As for the role of the hydrogen, the figure shows that the initially distributed H atoms in the a-Si:H layer accumulate at the free a-Si:H surface, whereas only one H atom is found at the interface at the end of the annealing.

The qualitative results from Fig. 4.10 concerning the defect structure are quantified in Fig. 4.11, where the behavior of dangling bonds upon annealing is shown as a function of time. Fig. 4.11(a) shows how the number of dangling bonds per atom, averaged over the whole structure, evolves. Thereby, the number of dangling bonds for each atom is defined as four minus the coordination number of that atom. In Fig. 4.11(b) the same is shown for different parts of the configuration: the interface region, defined as all atoms within a layer $z_i \pm 2.8 \text{ \AA}$, where z_i is the approximate position of the interface, the a-Si:H surface region, defined as all atoms at $z \geq L_z - 2.8 \text{ \AA}$, where L_z is the length of the configuration, and the bulk a-Si:H, defined as all atoms between the interface and the surface region. Fig. 4.11(c) shows how the center of mass $\langle z \rangle$ of all dangling bonds moves along the z -direction.

In order to obtain a smooth measure for the length L_z that does not react too sensitively to the fast movement of the surface atoms, we use a statistical definition. The a-Si:H layer has a thickness d and is centered at z_0 , and the Si atoms are approximately homogeneously distributed, such that the atomic density ϱ is constant over d . With this model assumption, the standard deviation of the atomic density in z -direction would be $\sigma_\varrho = d/\sqrt{12}$, from which follows $d = \sqrt{12}\sigma_\varrho$. The length of the structure is equal to the distance between the c-Si surface, which is held fixed at $z = 0$, and the a-Si:H surface, which is at $z = z_0 + d/2$. We therefore obtain

$$L_z = z_0 + \sqrt{3}\sigma_\varrho, \quad (4.1)$$

which means that we can relate the length of the structure to the center of mass and the standard deviation of the Si atoms in the a-Si:H layer. Calculating these as

$$z_0 = \frac{1}{N} \sum_I z_I \quad (4.2)$$

and

$$\sigma_\varrho = \sqrt{\frac{1}{N} \sum_I (z_I - z_0)^2}, \quad (4.3)$$

where the sum runs over all N Si atoms in the a-Si:H layer, and using the values in (4.1), gives us a measure for the length L_z . The behavior of L_z as a function of time and annealing temperature is shown in Fig. 4.12.

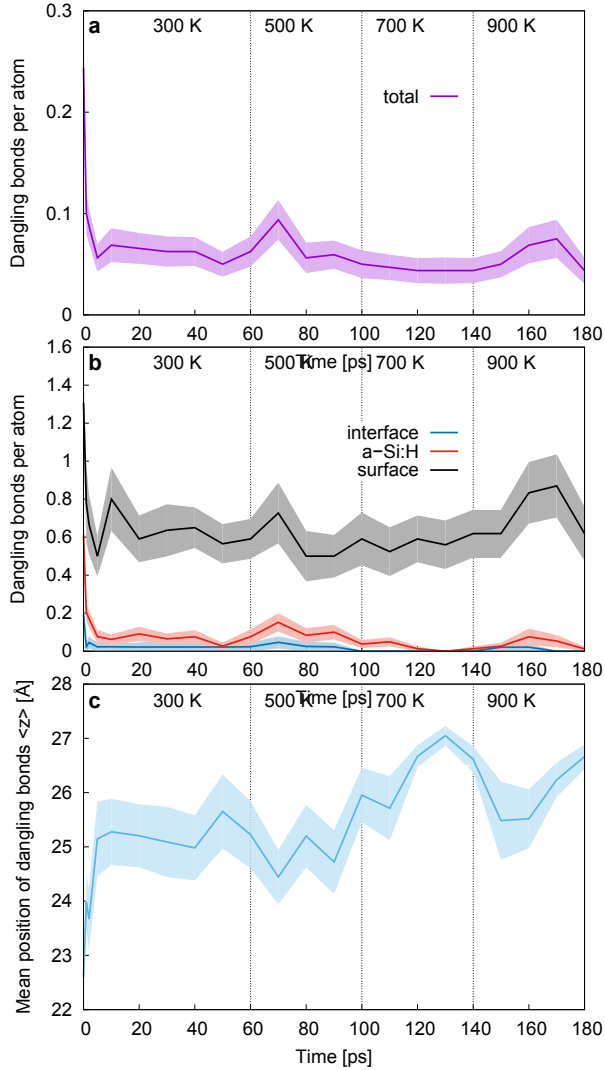


Figure 4.11: Evolution of dangling bonds upon annealing at different temperatures (indicated by vertical lines). (a) Number of dangling bonds per atom averaged over the whole structure. The filled curve represents the standard deviation of the average. (b) Number of dangling bonds per atom averaged over the interface region, the free surface region, and the rest of the a-Si:H layer. (c) Mean position $\langle z \rangle$ of dangling bonds in z -direction. The filled curve represents the standard deviation of $\langle z \rangle$. A value of $\langle z \rangle \approx 21$ Å means that the center of mass is roughly in the center of the a-Si:H layer, whereas a value of 27 Å means that the dangling bonds are located near the surface. Most of the defect healing during the first annealing step occurs in the first few ps. This is accompanied by a migration of defects towards the free surface, leaving the interface and the bulk region essentially defect free. The high-temperature annealing reduces the defect density only very slowly. [7]

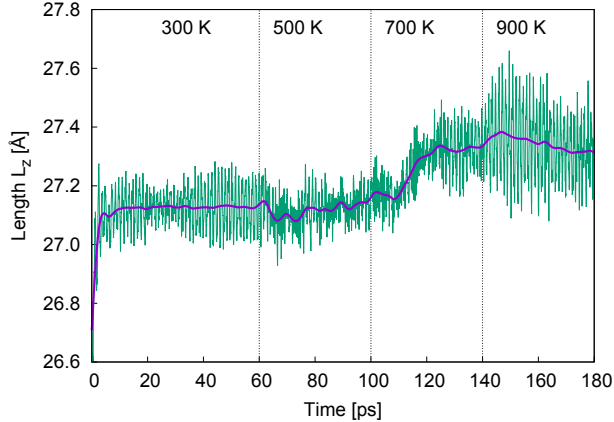


Figure 4.12: Total length of the structure as a function of time, both instantaneous (green) and time averaged (purple). The vertical lines indicate the times at which the annealing temperature was changed. Within the first few ps the structure expands rapidly, before reaching equilibrium length. During the rest of the annealing, the structure slowly expands by 0.2 Å on average, accompanied by thermal fluctuations. [7]

Fig. 4.11 shows that the largest contribution to the defect healing actually occurs within the first few picoseconds of annealing at 300 K, where a sudden and significant drop of the dangling bond density is observed. At the end of this, dangling bonds at the interface and in the bulk region have vanished almost completely, leaving the surface atoms as the main source of defects. This shows as a sudden shift of $\langle z \rangle$ toward the surface region above 25 Å. During the rest of the high-temperature annealing the number of dangling bonds still decreases, however only very slowly, by a total of about 25%.

Another important question concerns the role of the hydrogen in the interface configuration. From what we can see in Fig. 4.10 there is no accumulation of hydrogen at the interface. Nevertheless, the interface is completely defect free. This means that the healing of defects is mostly driven by reorganization of the Si atoms, and not by H-passivation. At the a-Si:H surface on the other hand, where dangling bonds cannot completely be eliminated, H-passivation does play an important role. In fact, when looking at the average hydrogen movement along the z -direction (Fig. 4.13), we see that during the high-temperature annealing the H atoms are moving towards the surface. The jumps of the center of mass $\langle z \rangle$ are thereby mostly due to hydrogen atoms hopping from one Si atom to another, i.e., one Si-H bond breaking and a new one forming. The movement happens at a very high average speed of ~ 0.01 Å/ps, which can not be explained as a hydrogen-gradient driven diffusion, as the estimated diffusion speed $v_{\text{diff}} \sim D/L_z$ is only of the order of 10^{-7} Å/ps at 900 K, assuming a diffusion coefficient $D \sim 10^{-14}$ m²/s [96]. Instead, the hydrogen movement appears to be following the movement of the dangling bonds displayed in Fig. 4.11(c).

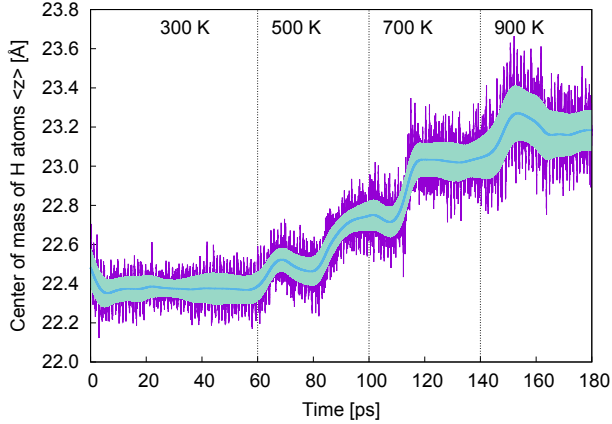


Figure 4.13: Center of mass $\langle z \rangle$ of H atoms in the amorphous layer along the z -direction as a function of time at different annealing temperatures (indicated by vertical lines). Shown is the instantaneous (purple line) and the time-averaged position (blue line). The filled curve represents the standard deviation of the time average. The H atoms move rapidly towards the surface, where the jumps in $\langle z \rangle$ are mostly due to H atoms hopping from one Si atom to another. The speed of the movement is multiple orders of magnitude higher than the expected thermal diffusion speed. Instead, the movement can be explained as a reaction to the movement of the defects (see Fig. 4.11). [7]

4.4.2 Evolution of electronic properties

In order to understand how the changes in the atomic structure upon annealing affect the electronic structure, we compare the DOS at different stages of the annealing process, both in the crystalline and in the amorphous part (Fig. 4.14). Additionally, the evolution of localized states, which are largely responsible for changes in the DOS around the gap, is displayed in Fig. 4.15. Before the annealing, the gap is completely filled with states, which are, due to the high density of dangling bonds both in the amorphous part and at the interface, spread out over the whole a-Si:H layer, and also extend into the c-Si layer, giving rise to a metallic DOS in both layers. This changes upon annealing at 300 K, when the interface becomes defect free and the number of gap states decreases significantly. The remaining gap states become localized inside the a-Si:H, such that in the crystalline layer the band gap is almost free of states, whereas in the amorphous layer the mobility gap is still filled. Only after increasing the temperature, the gap states become sparse enough such that a real gap opens. The lowest defect state density is reached at the end of the 700 K simulation, where only a small number of mid-gap states remains, which are mostly associated with surface atoms. On the other hand, with increasing time and temperature, a growing number of localized states forms in the interface region, which is supposedly due to the increasing disorder of the crystalline structure near the interface. These states are observed mostly at the top of the gap, and lead to an increase of the crystalline DOS near the conduction band edge, which gradually narrows the c-Si band gap and smears out the band edge. As opposed to that, the electronic structure near the valence band edge remains much more stable throughout the annealing.

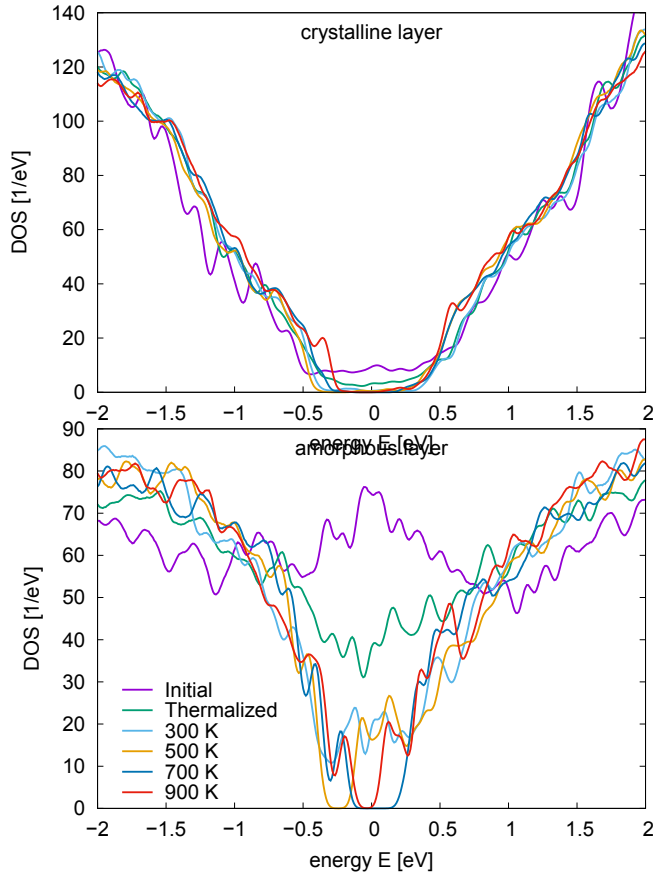


Figure 4.14: DOS integrated over the crystalline (top) and the amorphous layer (bottom), before annealing and at the end of each temperature step. The gap states in the crystalline DOS appear due to initial defects at the interface and vanish after annealing. However, states near the band edges, in particular the conduction band edge, form due to the increasing disorder of the crystalline structure near the interface. The density of gap states in the amorphous layer, arising from dangling bonds, is reduced to almost zero by the high-temperature annealing. [7]

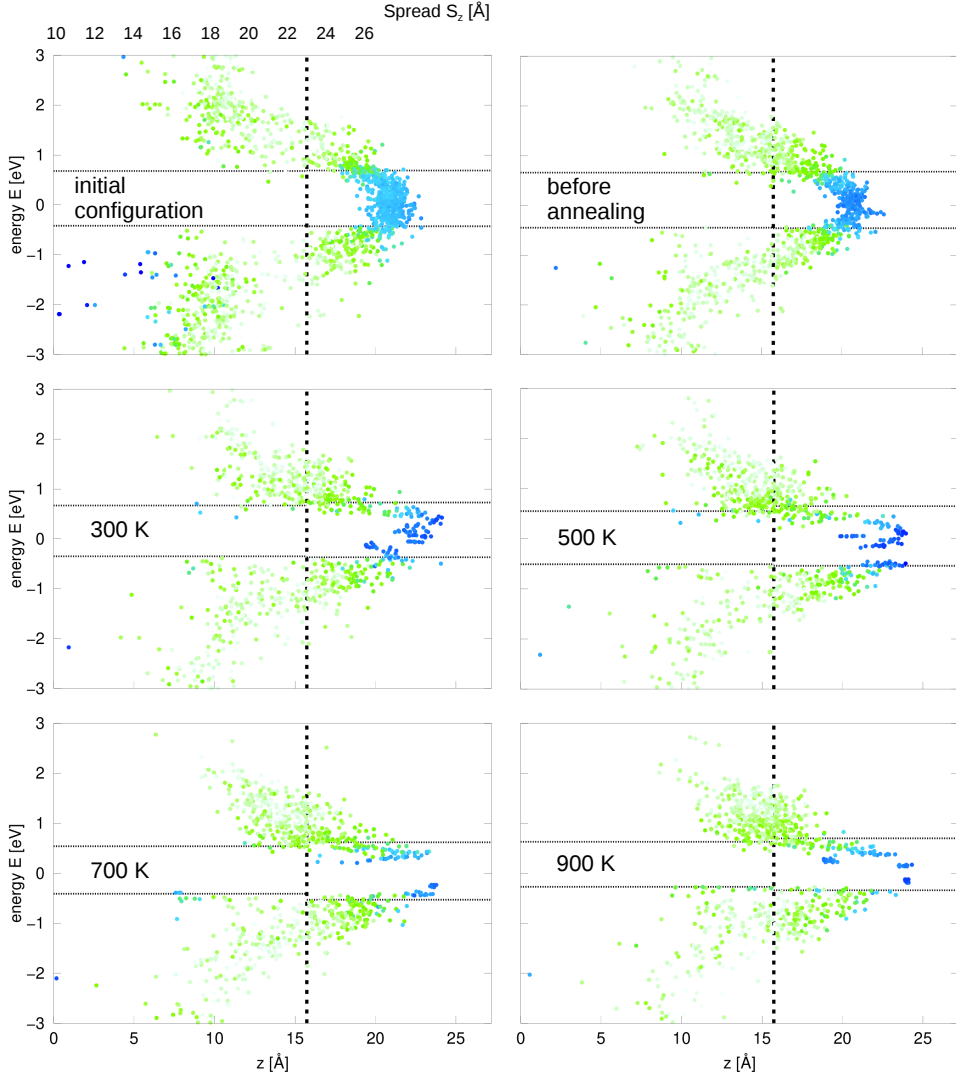


Figure 4.15: Representation of localized states with $S_z < 26 \text{ \AA}$ at different stages of the annealing process (initial configuration, prior to annealing, and after annealing at 300 K, 500 K, 700 K, and 900 K). Each dot marks the energy and the z -position of the center of one wave function, while the color represents its spread S_z . The vertical dashed line marks the approximate position of the interface, the horizontal lines indicate the band edges. In the initial configuration the effect of the weak connection between the two layers is clearly visible from the high amount of confined valence states on both sides, which decreases after thermalization. Before annealing, the mobility gap is completely filled with localized states in the a-Si:H layer. Upon annealing, the number of gap states decreases strongly. The c-Si band gap is slowly narrowing due to an increasing formation of states at the bottom of the conduction band near the interface. The valence states do not change much, on the other hand.

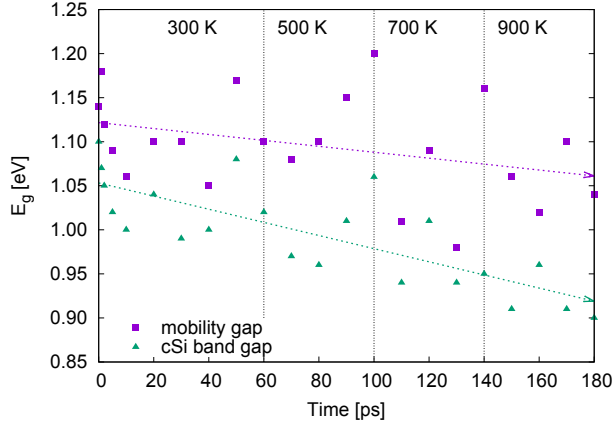


Figure 4.16: Band gap of the c-Si layer and mobility gap (according to the definition in sec. 4.3.2) as a function of time at different annealing temperatures (indicated by vertical lines). The c-Si gap decreases in time due to the increasing disorder of the crystalline structure close to the interface. The mobility gap shows large fluctuations, but decreases only slightly on average. These trends are visualized through the dashed arrows.

The effect of the changes in the DOS on the band and mobility gap, as defined in sec. 4.3.2, can be seen in Fig. 4.16. The c-Si band gap decreases significantly on average, by about 0.15 eV, probably due to the increasing disorder of the crystalline structure near the interface. Even though the method chosen to determine the band gap disregards states directly localized at the interface, the c-Si layer is too thin to eliminate interface effects completely. The mobility gap also decreases on average, but only insignificantly, by about 0.05 eV. This might be related to the expansion of the a-Si:H (cf. Fig. 4.12), but could also be a statistical artifact. The values of both gaps fluctuate because of their sensitive dependence on changes in the PDOS. This sensitivity is the stronger the flatter the PDOS is at the band edges. As the PDOS of extended states, defining the mobility gap, is in general flatter and also subject to bigger changes than the PDOS of crystalline states, defining the c-Si band gap, the fluctuations in the mobility gap are larger. All fluctuations lie however within a range of ± 0.1 eV, which is the assumed approximate error in determining the gaps.

Due to the particular importance of interface states, we shall back up the previously made qualitative observations about these states with a systematic analysis. For that purpose, we define interface states as all localized states with a mean position $13 \text{ \AA} \leq \langle z \rangle \leq 19 \text{ \AA}$ and an energy within the mobility gap. Two things should thereby be noted. (a) This is obviously not a strict definition of an interface state, as the interface does not have sharp boundaries and the mean position is subject to a large uncertainty. However, despite some inevitably wrongly classified states, it should be able to show some general trends. (b) We do not distinguish here between intrinsic and extrinsic, i.e., defect or disorder induced interface states. Interface resonances on the other hand, i.e., states localized at the interface with energies outside the gap, are disregarded, as they do not play a role in surface recombination. With the given definition, we investigate how the number and energy of both occupied and unoccupied interface states

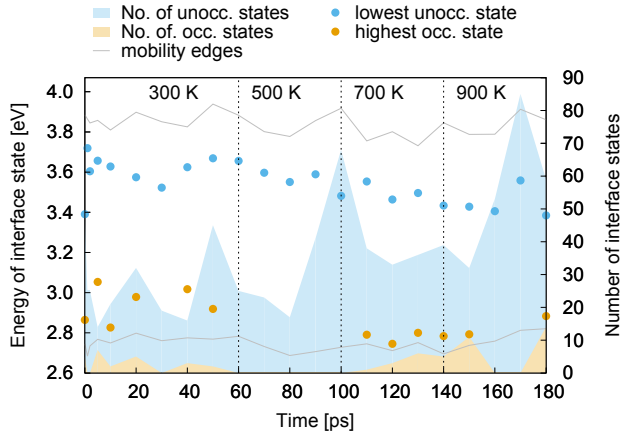


Figure 4.17: Evolution of interface states upon annealing at different temperatures (indicated by vertical lines). The points indicate the energies of the highest occupied and the lowest unoccupied interface state, respectively, while the filled curves show the total number of occupied and unoccupied interface states, respectively. The grey lines represent the mobility edges. Despite large fluctuations, the number of interface states below the conduction band edge is clearly growing, while their energies are descending into the gap. Near the valence band edge, only few interface states form, and no trend is visible.

changes upon annealing, where the energy is represented by the energy of the highest occupied and the lowest unoccupied state, respectively. This is shown in Fig. 4.17. Even though there are large fluctuations, the figure clearly shows that the number of unoccupied interface states is increasing upon annealing, whereas the number of occupied interface states is small and remains unaffected by annealing. This confirms our previous observation that interface states form mostly near the conduction band edge, which is possibly related to the chosen interface geometry. In fact, it has been shown in previous calculations that the generation conditions, such as orientation and structure of the c-Si surface, affect the position of extrinsic interface states [90]. In addition to the increasing number of unoccupied interface states, the figure also shows that, starting from 500 K, the low-lying states move from the conduction band edge deeper into the gap. As opposed to that, occupied interface states exist, if at all, only right above the valence band edge. The deep states appearing at the beginning of the annealing are induced by dangling bonds, which disappear after annealing at 300 K. As stated before, the increase in the number of gap states can probably be attributed to the increasing disorder at the interface, giving rise to tail states, i.e., states with energies close to the mobility edges, which can also be observed in Fig. 4.15. The reason for the energy shift of deep interface states, which are presumably of intrinsic nature, remains however unclear. Whereas tail states do not contribute significantly to recombination, the latter effect could actually lead to an increase of recombination at the interface upon annealing at temperatures higher than 300 K.

4.5 Effect of surface passivation

By performing an annealing at 700 K we obtained a defect-free interface and bulk region, and could reduce the total defect density to 0.04 dangling bonds per atom. From an experimental point of view, however, this defect density is still multiple orders of magnitude too high. Besides, even though the defects are located only at the surface, they still affect the electronic structure at the interface, due to the thin layer thickness. This raises the question if the quality of our model structure could be further improved by passivating the remaining dangling bonds at the surface with additional hydrogen atoms, and how this would affect the electronic properties.

For that purpose we analyzed a configuration where an extra ten H atoms were added at the free a-Si:H surface, increasing the hydrogen concentration from 11% to 17%, and which was then annealed at 1100 K. The results of this analysis are summarized in Fig. 4.18. The representation of the atomic structure (Fig. 4.18(a)) shows that the added H atoms remain at the surface instead of moving into the bulk, meaning that, together with the already present H atoms, about 70% of the hydrogen is accumulated in the surface region. Each of these atoms is bonded to exactly one Si atom, with the result that all but four dangling bonds are passivated, further reducing the defect density by 71%. Except from that, the only effect on the atomic structure is a slight expansion by about 0.9%. The effects on the electronic structure can be seen in Fig. 4.18(b). The passivation of the dangling bonds removed most localized states in the amorphous part from the mobility gap. The few remaining states near the surface can be related to the remaining dangling bonds. Apart from these, gap states are only found in the interface region, below the conduction band edge. As expected, these interface states are unaffected by the passivation. Besides the reduction of gap states, which was the purpose of the surface passivation, we also observe a significant widening of the mobility gap. This is probably a result of the H atoms shifting states away from the Fermi level, and is therefore a direct effect of the increased hydrogen concentration, which has been observed in a-Si:H both experimentally and computationally [56, 68]. This is somewhat problematic since the goal is to obtain macroscopic properties of the a-Si:H/c-Si interface under experimental conditions, where the hydrogen concentration is lower. A thicker a-Si:H layer, in combination with surface passivation, would therefore be a better, however computationally more expensive, approach to eliminate surface effects, since this would reduce the influence of the surface on the interface region, while at the same time the passivation would have less impact on the overall hydrogen concentration.

4.6 Conclusions

We used model configurations of an a-Si:H/c-Si interface consisting of a c-Si layer of 192 Si atoms, and an a-Si:H layer of 128 Si and 16 H atoms, to analyze the structural and electronic properties of a silicon heterojunction from first principles. For that purpose, multiple different configurations representing the interface at different stages of a high-temperature annealing were chosen, for which the electronic structure was calculated on the DFT level and was subsequently analyzed.

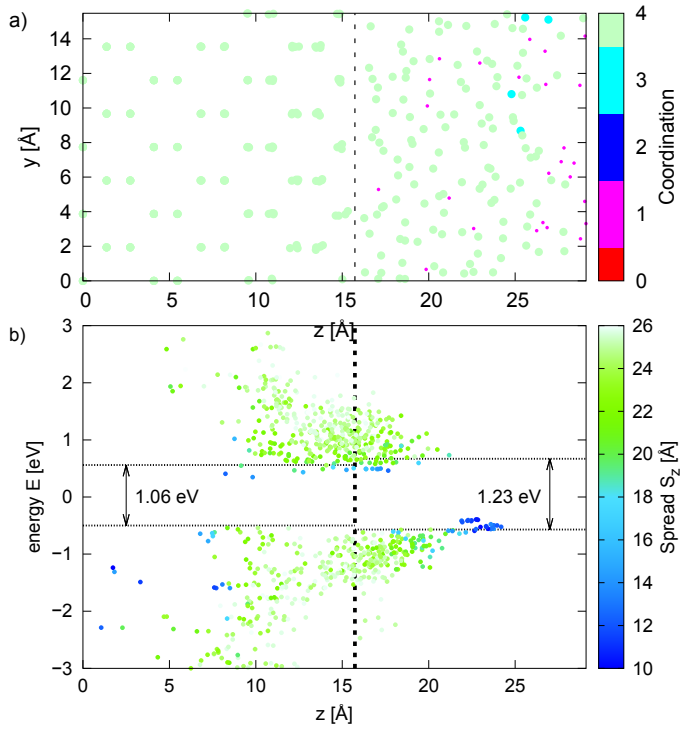


Figure 4.18: Atomic and electronic structure of the passivated configuration. (a) Projection of the positions of Si (large dots) and H (small dots) atoms onto the yz -plane. The color indicates the coordination number according to the ELF criterion. The dashed line marks the approximate position of the interface. The additional H atoms remain at the surface, where they form bonds with the under-coordinated surface atoms, resulting in a configuration that is almost completely defect free. (b) Energy and localization of states with $S_z < 26$ Å. Each dot marks the energy and the z -position of the center of one wave function, whereas the color represents its spread. The horizontal lines indicate the band edges. The passivation of the dangling bonds at the surface moves almost all states out of the mobility gap, and additionally widens the gap. Interface states, on the other hand, remain present.

We found that, in order to obtain an interface configuration that can potentially yield macroscopic properties that are comparable to the experiment, a high-temperature annealing is indispensable. Even though the defect density is relatively low already with 300 K, a satisfactory low density of gap states is achieved only with 700 K. By increasing the temperature to 900 K, no further improvement in the atomic or electronic structure could be gained. During the annealing process we observed that there is no concentration of defects at the interface. In fact both the interface region and the bulk a-Si:H are essentially defect free. Surprisingly, hydrogen passivation at the interface does not seem to play a significant role. On the contrary, there is actually a fast hydrogen movement towards the surface that seems to follow the defect concentration.

As a first step toward the ab initio description of transport and recombination in the heterojunction solar cell, we characterized the electronic states according to their energy, localization, and position, and, based on this characterization, extracted the band gap E_g in the c-Si layer and the mobility gap E_g^{mob} in the a-Si:H layer, as well as the band offsets $\Delta E_{v/c}$. For the configuration at the end of the 700 K annealing, which was found to be most promising in terms of a low concentration of defects and gap states, we obtained values of $E_g = 0.95$ eV, $E_g^{\text{mob}} = 1.16$ eV, $\Delta E_v = 0.13$ eV, and $\Delta E_c = 0.08$ eV, which are in qualitative agreement with experiments and previous calculations. We thereby, however, faced the problem that the relatively high uncertainty of ~ 0.1 eV in determining the gaps makes it very difficult to get reliable offsets.

The characterization of the electronic states also revealed the existence of strongly localized gap states close to the interface, which cannot be related to dangling bonds and therefore seem to be of intrinsic nature. Both intrinsic and extrinsic, i.e., disorder induced, interface states are found almost exclusively in the upper part of the mobility gap. This could be a result of the generation conditions of the a-Si:H/c-Si structure, in particular of the orientation of the c-Si surface. Also the use of a reconstructed surface could play a role, giving rise to a potential barrier at the interface, which could also affect the existence and energy of interface states. It would therefore be interesting and important to compare these results with other structures, employing a different c-Si surface.

The effect of the annealing on the interface states was found to be an increase of the number of unoccupied states with a simultaneous lowering of their energies deeper into the gap. This seems to be a result of the increasing disorder of the crystalline structure near the interface, which also causes a narrowing of the band gap, suggesting that a longer annealing at temperatures higher than 700 K might actually lower the quality of the structure again, and lead to a higher density of gap states.

Finally, we analyzed a configuration where the majority of the dangling bonds were passivated with additional H atoms, leading to a very low number of gap states, comparable to the 576-atom bulk a-Si:H configuration analyzed in the previous chapter. Additionally, however, the increased hydrogen concentration also leads to a larger mobility gap, which is an unwanted side effect that can only be eliminated by using thicker a-Si:H layers.

Larger model structures would be desirable as they would reduce the impact of surface effects on the interface region, and the impact of the interface region on the crystalline layer, in particular on the band gap.

This work is a first step on the way to a full ab-initio description of the silicon heterojunction solar cell. However, in order to obtain quantitatively accurate results, methods beyond DFT will have to be applied. Additionally, larger model structures will be needed to reduce the impact of surface effects on the interface region, and the impact of the interface region on the crystalline layer, in particular on the band gap. They would furthermore allow for a more accurate determination of the macroscopic properties by reducing the sensitivity to small changes in the atomic and electronic structure. Also, the generation parameters must be tested and chosen to most closely reproduce the experimental situation. For example, the choice of an unreconstructed or H-passivated crystalline surface as a starting point for the generation of the interface would change the potential and might give rise to different types of states at the interface.

5 Conclusions

The goal of this thesis was to provide a fully ab initio based description of the a-Si:H/c-Si interface, with a focus on the extraction of microscopic information and macroscopic parameters relevant for the application in photovoltaics, in particular in the silicon-heterojunction (SHJ) solar cell.

For that purpose we analyzed in a first step model structures of bulk a-Si:H, and in a second step model structures of a-Si:H/c-Si interfaces, with respect to their ability to reproduce the real experimental properties of these materials. It was found that only configurations that are free of (bulk) defects, which is achieved via a high-temperature annealing, are suitable for material modeling, as already few defects result in an unphysically high gap-state density.

After identifying suitable structures, we used a combination of new and existing methods to convert the raw electronic structure, obtained from density-functional-theory (DFT) calculations, into micro- and macroscopic properties characterizing the structural, electronic, and optical properties of these structures. In particular, in view of the application in photovoltaics, we calculated the absorption spectrum and the optical gap for a-Si:H, characterized the localized states in the a-Si:H/c-Si interface with respect to their energy, position, and origin, and suggested a way of extracting the mobility gap in a-Si:H, which was then applied to the interface in order to obtain the band offsets.

Even though the calculated densities of states and absorption spectra qualitatively resembled the experimental situation, the values of band, optical, and mobility gaps were consequently underestimated by our calculations. This problem could be partially attributed to quasiparticle effects and solved by G_0W_0 calculations, but partially also to finite-size effects, caused by the finite dimensions of the super cells, and, in case of the a-Si:H/c-Si structure, also by the presence of the interface and the surface. This error can be reduced only by enlarging the super cells, as we could observe by comparing different structure sizes. An additional error source arises from the ambiguity in the definition of the optical and the mobility gap, giving rise to an uncertainty that exceeds the necessary accuracy for determining reliable values for the band offsets. This uncertainty could, however, also be reduced by increasing the super-cell size.

Even though the exact quantification of the observed finite-size effects is difficult, we can state that, in order to obtain accurate gap values and defect densities, larger model structures will be needed, which could be realized with new electronic structure methods, such as linear-scaling DFT [97]. Also the effect of quasiparticle corrections could not be studied to its full extent within this thesis, due to the high computational costs of a fully self-consistent GW calculation that includes also the corrections to the wave functions. This should be further investigated, as it could have an additional impact both on the size of the gap and on localization. Meanwhile, the next step towards a comprehensive multiscale simulation of the SHJ will be the inclusion of electron-phonon interaction into the microscopic picture, which will allow for the calculation of the non-radiative capture cross sections for states that were identified as relevant for Shockley-Read-Hall recombination. The microscopic information on the states contributing to transport and recombination can then be integrated in a mesoscopic

model for the charge carrier dynamics, in order to obtain recombination rates and mobilities, which can finally be used as parameters in macroscopic device simulations.

Bibliography

- [1] Fraunhofer Institute for Solar Energy Systems. *Photovoltaics report* (2018). <https://www.ise.fraunhofer.de/content/dam/ise/de/documents/publications/studies/Photovoltaics-Report.pdf>. Accessed 14 Dec 2018.
- [2] Aeberhard, U., Czaja, P., Ermes, M., Pieters, B., Chistiakova, G., Bittkau, K., Richter, A., Ding, K., Giusepponi, S., and Celino, M. *Towards a Multi-scale Approach to the Simulation of Silicon Hetero-junction Solar Cells*. *Journal of Green Engineering* **5** (4), 11 (2016).
- [3] Markvart, T. and Castañer, L. *Chapter IA-1 - Principles of Solar Cell Operation*. In A. McEvoy, T. Markvart, and L. Castañer, editors, *Practical Handbook of Photovoltaics*, pages 7–31. Academic Press, Boston, second edition (2012).
- [4] Kleider, J.-P. *Band Lineup Theories and the Determination of Band Offsets from Electrical Measurements*. In W. G. J. H. M. van Sark, L. Korte, and F. Roca, editors, *Physics and Technology of Amorphous-Crystalline Heterostructure Silicon Solar Cells*, pages 405–444. Springer Berlin Heidelberg, Berlin, Heidelberg (2012).
- [5] Czaja, P., Celino, M., Giusepponi, S., Gusso, M., and Aeberhard, U. *Ab Initio Description of Optoelectronic Properties at Defective Interfaces in Solar Cells*. In E. Di Napoli, M.-A. Hermanns, H. Iliev, A. Lintermann, and A. Peyser, editors, *High-Performance Scientific Computing*, pages 111–124. Springer International Publishing, Cham (2017). ISBN 978-3-319-53862-4.
- [6] Czaja, P., Celino, M., Giusepponi, S., Gusso, M., and Aeberhard, U. *Ab initio study on localization and finite size effects in the structural, electronic, and optical properties of hydrogenated amorphous silicon*. *Computational Materials Science* **155**, 159 (2018).
- [7] Czaja, P., Giusepponi, S., Gusso, M., Celino, M., and Aeberhard, U. *Computational characterization of a-Si:H/c-Si interfaces*. *Journal of Computational Electronics* **17** (4), 1457 (2018).
- [8] Martin, R. M. *Electronic Structure: Basic Theory and Practical Methods*. Cambridge University Press (2004).
- [9] Kohanoff, J. *Electronic Structure Calculations for Solids and Molecules: Theory and Computational Methods*. Cambridge University Press (2006).
- [10] Hohenberg, P. and Kohn, W. *Inhomogeneous Electron Gas*. *Phys. Rev.* **136**, B864 (1964).
- [11] Kohn, W. and Sham, L. J. *Self-Consistent Equations Including Exchange and Correlation Effects*. *Phys. Rev.* **140**, A1133 (1965).

- [12] Gross, E. and Dreizler, R., editors. *Density Functional Theory*. NATO Science Series B.: Springer (1995).
- [13] Thomas, L. H. *The calculation of atomic fields*. *Mathematical Proceedings of the Cambridge Philosophical Society* **23** (5), 542 (1927).
- [14] Fermi, E. *Eine statistische Methode zur Bestimmung einiger Eigenschaften des Atoms und ihre Anwendung auf die Theorie des periodischen Systems der Elemente*. *Zeitschrift für Physik* **48** (1), 73 (1928).
- [15] Hartree, D. R. *The Wave Mechanics of an Atom with a Non-Coulomb Central Field. Part I. Theory and Methods*. *Mathematical Proceedings of the Cambridge Philosophical Society* **24** (1), 89 (1928).
- [16] Fock, V. *Näherungsmethode zur Lösung des quantenmechanischen Mehrkörperproblems*. *Zeitschrift für Physik* **61** (1), 126 (1930).
- [17] Vosko, S. H., Wilk, L., and Nusair, M. *Accurate spin-dependent electron liquid correlation energies for local spin density calculations: a critical analysis*. *Canadian Journal of Physics* **58** (8), 1200 (1980).
- [18] Perdew, J. P. and Wang, Y. *Accurate and simple analytic representation of the electron-gas correlation energy*. *Phys. Rev. B* **45**, 13244 (1992). Erratum: **98**, 079904 (2018).
- [19] Ceperley, D. M. and Alder, B. J. *Ground State of the Electron Gas by a Stochastic Method*. *Phys. Rev. Lett.* **45**, 566 (1980).
- [20] Perdew, J. P., Ernzerhof, M., Zupan, A., and Burke, K. *Nonlocality of the density functional for exchange and correlation: Physical origins and chemical consequences*. *The Journal of Chemical Physics* **108** (4), 1522 (1998).
- [21] Perdew, J. P. and Wang, Y. *Accurate and simple density functional for the electronic exchange energy: Generalized gradient approximation*. *Phys. Rev. B* **33**, 8800 (1986). Erratum: **40**, 3399 (1989).
- [22] Becke, A. D. *Density-functional exchange-energy approximation with correct asymptotic behavior*. *Phys. Rev. A* **38**, 3098 (1988).
- [23] Lee, C., Yang, W., and Parr, R. G. *Development of the Colle-Salvetti correlation-energy formula into a functional of the electron density*. *Phys. Rev. B* **37**, 785 (1988).
- [24] Perdew, J. P., Burke, K., and Ernzerhof, M. *Generalized Gradient Approximation Made Simple*. *Phys. Rev. Lett.* **77**, 3865 (1996). Erratum: **78**, 1396 (1997).
- [25] Perdew, J. P., Burke, K., and Wang, Y. *Generalized gradient approximation for the exchange-correlation hole of a many-electron system*. *Phys. Rev. B* **54**, 16533 (1996). Erratum: **57**, 14999 (1998).

- [26] Heyd, J. and Scuseria, G. E. *Efficient hybrid density functional calculations in solids: Assessment of the Heyd-Scuseria-Ernzerhof screened Coulomb hybrid functional.* *The Journal of Chemical Physics* **121** (3), 1187 (2004).
- [27] Zhao, Y. and Truhlar, D. G. *Calculation of semiconductor band gaps with the M06-L density functional.* *The Journal of Chemical Physics* **130** (7), 074103 (2009).
- [28] Shimazaki, T. and Asai, Y. *Energy band structure calculations based on screened Hartree-Fock exchange method: Si, AlP, AlAs, GaP, and GaAs.* *The Journal of Chemical Physics* **132** (22), 224105 (2010).
- [29] Vanderbilt, D. *Soft self-consistent pseudopotentials in a generalized eigenvalue formalism.* *Phys. Rev. B* **41**, 7892 (1990).
- [30] Kresse, G. and Joubert, D. *From ultrasoft pseudopotentials to the projector augmented-wave method.* *Phys. Rev. B* **59**, 1758 (1999).
- [31] Hamann, D. R., Schlüter, M., and Chiang, C. *Norm-Conserving Pseudopotentials.* *Phys. Rev. Lett.* **43**, 1494 (1979).
- [32] Hamann, D. R. *Generalized norm-conserving pseudopotentials.* *Phys. Rev. B* **40**, 2980 (1989).
- [33] Rappe, A. M., Rabe, K. M., Kaxiras, E., and Joannopoulos, J. D. *Optimized pseudopotentials.* *Phys. Rev. B* **41**, 1227 (1990).
- [34] Troullier, N. and Martins, J. L. *Efficient pseudopotentials for plane-wave calculations.* *Phys. Rev. B* **43**, 1993 (1991).
- [35] Goedecker, S., Teter, M., and Hutter, J. *Separable dual-space Gaussian pseudopotentials.* *Phys. Rev. B* **54**, 1703 (1996).
- [36] Topp, W. C. and Hopfield, J. J. *Chemically Motivated Pseudopotential for Sodium.* *Phys. Rev. B* **7**, 1295 (1973).
- [37] Hedin, L. *New Method for Calculating the One-Particle Green's Function with Application to the Electron-Gas Problem.* *Phys. Rev.* **139**, A796 (1965).
- [38] Bohm, D. and Pines, D. *A Collective Description of Electron Interactions. I. Magnetic Interactions.* *Phys. Rev.* **82**, 625 (1951).
- [39] Pines, D. and Bohm, D. *A Collective Description of Electron Interactions: II. Collective vs Individual Particle Aspects of the Interactions.* *Phys. Rev.* **85**, 338 (1952).
- [40] Bohm, D. and Pines, D. *A Collective Description of Electron Interactions: III. Coulomb Interactions in a Degenerate Electron Gas.* *Phys. Rev.* **92**, 609 (1953).

- [41] Hybertsen, M. S. and Louie, S. G. *First-Principles Theory of Quasiparticles: Calculation of Band Gaps in Semiconductors and Insulators*. *Phys. Rev. Lett.* **55**, 1418 (1985).
- [42] Hybertsen, M. S. and Louie, S. G. *Electron correlation in semiconductors and insulators: Band gaps and quasiparticle energies*. *Phys. Rev. B* **34**, 5390 (1986).
- [43] Godby, R. W., Schlüter, M., and Sham, L. J. *Accurate Exchange-Correlation Potential for Silicon and Its Discontinuity on Addition of an Electron*. *Phys. Rev. Lett.* **56**, 2415 (1986).
- [44] Larson, P., Dvorak, M., and Wu, Z. *Role of the plasmon-pole model in the GW approximation*. *Phys. Rev. B* **88**, 125205 (2013).
- [45] Duffy, P., Chong, D. P., Casida, M. E., and Salahub, D. R. *Assessment of Kohn-Sham density-functional orbitals as approximate Dyson orbitals for the calculation of electron-momentum-spectroscopy scattering cross sections*. *Phys. Rev. A* **50**, 4707 (1994).
- [46] Baraff, G. A. and Schlüter, M. *Migration of interstitials in silicon*. *Phys. Rev. B* **30**, 3460 (1984).
- [47] Godby, R. W., Schlüter, M., and Sham, L. J. *Self-energy operators and exchange-correlation potentials in semiconductors*. *Phys. Rev. B* **37**, 10159 (1988).
- [48] Becke, A. D. and Edgecombe, K. E. *A simple measure of electron localization in atomic and molecular systems*. *The Journal of Chemical Physics* **92** (9), 5397 (1990).
- [49] Boyd, R. J. *The shell structure of atoms*. *Journal of Physics B: Atomic and Molecular Physics* **9** (5), L69 (1976).
- [50] McWeeny, R. *Some Recent Advances in Density Matrix Theory*. *Rev. Mod. Phys.* **32** (2), 335 (1960).
- [51] Becke, A. D. *Hartree-Fock exchange energy of an inhomogeneous electron gas*. *International Journal of Quantum Chemistry* **23** (6), 1915 (1983).
- [52] Czaja, P. *Ab-initio analysis of electronic material properties*. Bachelor thesis, RWTH Aachen University (2010).
- [53] Johlin, E., Wagner, L. K., Buonassisi, T., and Grossman, J. C. *Origins of Structural Hole Traps in Hydrogenated Amorphous Silicon*. *Phys. Rev. Lett.* **110**, 146805 (2013).
- [54] Jarolimek, K., Hazrati, E., de Groot, R. A., and de Wijs, G. A. *Band Offsets at the Interface between Crystalline and Amorphous Silicon from First Principles*. *Phys. Rev. Applied* **8**, 014026 (2017).
- [55] Ziman, J. M., editor. *Models of disorder : the theoretical physics of homogeneously disordered systems*. Cambridge University Press, Cambridge (1979).

- [56] Legesse, M., Nolan, M., and Fagas, G. *Revisiting the Dependence of the Optical and Mobility Gaps of Hydrogenated Amorphous Silicon on Hydrogen Concentration*. *The Journal of Physical Chemistry C* **117** (45), 23956 (2013).
- [57] Winer, K. *Defects in Hydrogenated Amorphous Silicon*. *Annual Review of Materials Science* **21** (1), 1 (1991).
- [58] Tauc, J., Grigorovici, R., and Vancu, A. *Optical Properties and Electronic Structure of Amorphous Germanium*. *Physica Status Solidi (b)* **15** (2), 627 (1966).
- [59] Jackson, W. B., Kelso, S. M., Tsai, C. C., Allen, J. W., and Oh, S.-J. *Energy dependence of the optical matrix element in hydrogenated amorphous and crystalline silicon*. *Phys. Rev. B* **31**, 5187 (1985).
- [60] Carlson, D. E. and Wronski, C. R. *Amorphous silicon solar cell*. *Applied Physics Letters* **28** (11), 671 (1976).
- [61] Allan, D. C., Joannopoulos, J. D., and Pollard, W. B. *Electronic states and total energies in hydrogenated amorphous silicon*. *Phys. Rev. B* **25**, 1065 (1982).
- [62] Fedders, P. A. and Drabold, D. A. *Hydrogen and defects in first-principles molecular-dynamics-modeled a -Si:H*. *Phys. Rev. B* **47**, 13277 (1993).
- [63] Tuttle, B. and Adams, J. B. *Energetics of hydrogen in amorphous silicon: An ab initio study*. *Phys. Rev. B* **57**, 12859 (1998).
- [64] Valladares, A. A., Alvarez, F., Liu, Z., Sticht, J., and Harris, J. *Ab initio studies of the atomic and electronic structure of pure and hydrogenated a-Si*. *Eur. Phys. J. B* **22** (4), 443 (2001).
- [65] Jarolimek, K., de Groot, R. A., de Wijs, G. A., and Zeman, M. *First-principles study of hydrogenated amorphous silicon*. *Phys. Rev. B* **79**, 155206 (2009).
- [66] Khomyakov, P. A., Andreoni, W., Afify, N. D., and Curioni, A. *Large-Scale Simulations of a-Si:H: The Origin of Midgap States Revisited*. *Phys. Rev. Lett.* **107**, 255502 (2011).
- [67] Shockley, W. and Read, W. T. *Statistics of the Recombinations of Holes and Electrons*. *Phys. Rev.* **87**, 835 (1952).
- [68] Street, R. A. *Hydrogenated amorphous silicon*. Cambridge University Pr., Cambridge (1991).
- [69] Durandurdu, M., Drabold, D. A., and Mousseau, N. *Approximate ab initio calculations of electronic structure of amorphous silicon*. *Phys. Rev. B* **62**, 15307 (2000).
- [70] Rosato, V. and Celino, M. *Tight binding simulation of the thermodynamic behavior of amorphous silicon*. *Journal of Applied Physics* **86** (12), 6826 (1999).

- [71] Nolan, M., Legesse, M., and Fagas, G. *Surface orientation effects in crystalline-amorphous silicon interfaces*. *Phys. Chem. Chem. Phys.* **14**, 15173 (2012).
- [72] Perdew, J. P. *Density functional theory and the band gap problem*. *International Journal of Quantum Chemistry* **28** (S19), 497 (1985).
- [73] Car, R. and Parrinello, M. *Structural, Dynamical, and Electronic Properties of Amorphous Silicon: An ab initio Molecular-Dynamics Study*. *Phys. Rev. Lett.* **60**, 204 (1988).
- [74] Remeš, Z., Vaněček, M., Mahan, A. H., and Crandall, R. S. *Silicon network relaxation in amorphous hydrogenated silicon*. *Phys. Rev. B* **56**, R12710 (1997).
- [75] *Quantum ESPRESSO*. <http://www.quantum-espresso.org>. Accessed 29 Aug 2018.
- [76] Giannozzi, P., Baroni, S., Bonini, N., Calandra, M., Car, R., Cavazzoni, C., Ceresoli, D., Chiarotti, G. L., Cococcioni, M., Dabo, I., Corso, A. D., de Gironcoli, S., Fabris, S., Fratesi, G., Gebauer, R., Gerstmann, U., Gougoussis, C., Kokalj, A., Lazzeri, M., Martin-Samos, L., Marzari, N., Mauri, F., Mazzarello, R., Paolini, S., Pasquarello, A., Paulatto, L., Sbraccia, C., Scandolo, S., Sclauzero, G., Seitsonen, A. P., Smogunov, A., Umari, P., and Wentzcovitch, R. M. *QUANTUM ESPRESSO: a modular and open-source software project for quantum simulations of materials*. *Journal of Physics: Condensed Matter* **21** (39), 395502 (2009).
- [77] Deslippe, J., Samsonidze, G., Strubbe, D. A., Jain, M., Cohen, M. L., and Louie, S. G. *BerkeleyGW: A massively parallel computer package for the calculation of the quasiparticle and optical properties of materials and nanostructures*. *Computer Physics Communications* **183** (6), 1269 (2012).
- [78] Bellissent, R., Chenevas-Paule, A., Chieux, P., and Menelle, A. *a-Si:H short range order by neutron scattering*. *Journal of Non-Crystalline Solids* **77-78**, 213 (1985).
- [79] Favre, M., Curtins, H., and Shah, A. *Study of surface/interface and bulk defect density in a-Si:H by means of photothermal deflection spectroscopy and photoconductivity*. *Journal of Non-Crystalline Solids* **97**, 731 (1987).
- [80] Street, R. A. and Winer, K. *Defect equilibria in undoped a-Si:H*. *Phys. Rev. B* **40**, 6236 (1989).
- [81] Cody, G. D., Tiedje, T., Abeles, B., Brooks, B., and Goldstein, Y. *Disorder and the Optical-Absorption Edge of Hydrogenated Amorphous Silicon*. *Phys. Rev. Lett.* **47**, 1480 (1981).
- [82] Tsai, C. and Fritzsche, H. *Effect of annealing on the optical properties of plasma deposited amorphous hydrogenated silicon*. *Solar Energy Materials* **1** (1), 29 (1979).
- [83] Yoshikawa, K., Kawasaki, H., Yoshida, W., Irie, T., Konishi, K., Nakano, K., Uto, T., Adachi, D., Kanematsu, M., Uzu, H., and Yamamoto, K. *Silicon heterojunction solar*

cell with interdigitated back contacts for a photoconversion efficiency over 26%. *Nature Energy* **2**, 17032 (2017).

- [84] Jensen, N., Rau, U., Hausner, R. M., Uppal, S., Oberbeck, L., Bergmann, R. B., and Werner, J. H. *Recombination mechanisms in amorphous silicon/crystalline silicon heterojunction solar cells*. *Journal of Applied Physics* **87** (5), 2639 (2000).
- [85] Song, Y., Park, M., Guliyants, E., and Anderson, W. *Influence of defects and band offsets on carrier transport mechanisms in amorphous silicon/crystalline silicon heterojunction solar cells*. *Solar Energy Materials and Solar Cells* **64** (3), 225 (2000).
- [86] Froitzheim, A., Brendel, K., Elstner, L., Fuhs, W., Kliefoth, K., and Schmidt, M. *Interface recombination in heterojunctions of amorphous and crystalline silicon*. *Journal of Non-Crystalline Solids* **299-302**, 663 (2002).
- [87] Peressi, M., Colombo, L., and Gironcoli, S. d. *Role of defects in the electronic properties of amorphous/crystalline Si interface*. *Phys. Rev. B* **64**, 193303 (2001).
- [88] Tosolini, M., Colombo, L., and Peressi, M. *Atomic-scale model of c-Si/a-Si:H interfaces*. *Phys. Rev. B* **69**, 075301 (2004).
- [89] George, B. M., Behrends, J., Schnegg, A., Schulze, T. F., Fehr, M., Korte, L., Rech, B., Lips, K., Rohrmüller, M., Rauls, E., Schmidt, W. G., and Gerstmann, U. *Atomic Structure of Interface States in Silicon Heterojunction Solar Cells*. *Phys. Rev. Lett.* **110**, 136803 (2013).
- [90] Santos, I., Cazzaniga, M., Onida, G., and Colombo, L. *Atomistic study of the structural and electronic properties of a-Si:H/c-Si interfaces*. *Journal of Physics: Condensed Matter* **26** (9), 095001 (2014).
- [91] Schulze, T. F., Korte, L., Ruske, F., and Rech, B. *Band lineup in amorphous/crystalline silicon heterojunctions and the impact of hydrogen microstructure and topological disorder*. *Phys. Rev. B* **83**, 165314 (2011).
- [92] Chiang, T. C. and Himpsel, F. J. *Subvolume A · 2.1.3 Si*. In A. Goldmann and E.-E. Koch, editors, *Landolt-Börnstein - Group III Condensed Matter*, volume 23A. Springer-Verlag Berlin Heidelberg (1989). [SpringerMaterials](#). Accessed 10 Dec 2018.
- [93] Mews, M., Liebhaber, M., Rech, B., and Korte, L. *Valence band alignment and hole transport in amorphous/crystalline silicon heterojunction solar cells*. *Applied Physics Letters* **107** (1), 013902 (2015).
- [94] Liebhaber, M., Mews, M., Schulze, T. F., Korte, L., Rech, B., and Lips, K. *Valence band offset in heterojunctions between crystalline silicon and amorphous silicon (sub)oxides (a-SiO_x:H, 0 < x < 2)*. *Applied Physics Letters* **106** (3), 031601 (2015).
- [95] Kleider, J. P., Gudovskikh, A. S., and Roca i Cabarrocas, P. *Determination of the conduction band offset between hydrogenated amorphous silicon and crystalline silicon*

- from surface inversion layer conductance measurements. *Applied Physics Letters* **92** (16), 162101 (2008).
- [96] Street, R. A., Tsai, C. C., Kakalios, J., and Jackson, W. B. *Hydrogen diffusion in amorphous silicon*. *Philosophical Magazine B* **56** (3), 305 (1987).
- [97] Goedecker, S. *Linear scaling electronic structure methods*. *Rev. Mod. Phys.* **71**, 1085 (1999).
- [98] Jülich Supercomputing Centre. *JURECA: General-purpose supercomputer at Jülich Supercomputing Centre*. *Journal of large-scale research facilities* **2**, A62 (2016).

Publications

- Czaja, P. and Aeberhard, U. *Multiscale modeling of nanostructure-based solar cells*. Poster presented at the CECAM Workshop 'High performance models for charge transport in large scale materials systems', Bremen (2014).
- Czaja, P., Aeberhard, U., Celino, M., and Grena, R. *Assessment of computational methods for the optical characterization of aSi:H*. Poster presented at the ICANS 26, Aachen (2015).
- Czaja, P., Aeberhard, U., Celino, M., and Giusepponi, S. *Ab initio description of absorption, transport and recombination at defective interfaces in solar cells*. Poster presented at the NIC Symposium, Aachen (2016).
- Aeberhard, U., Czaja, P., Ermes, M., Pieters, B., Chistiakova, G., Bittkau, K., Richter, A., Ding, K., Giusepponi, S., and Celino, M. *Towards a Multi-scale Approach to the Simulation of Silicon Hetero-junction Solar Cells*. *Journal of Green Engineering* **5** (4), 11 (2016).
- Czaja, P., Aeberhard, U., Celino, M., and Giusepponi, S. *Ab initio description of optoelectronic properties at defective interfaces in solar cells*. Talk given at the JARA-HPC Symposium, Aachen (2016).
- Czaja, P., Aeberhard, U., Celino, M., and Giusepponi, S. *Ab initio description of absorption, transport, and recombination at defective interfaces in solar cells*. Poster presented at the JARA-HPC Symposium, Aachen (2016).
- Czaja, P., Celino, M., Giusepponi, S., Gusso, M., and Aeberhard, U. *Ab Initio Description of Optoelectronic Properties at Defective Interfaces in Solar Cells*. In E. Di Napoli, M.-A. Hermanns, H. Iliev, A. Lintermann, and A. Peyser, editors, *High-Performance Scientific Computing*, pages 111–124. Springer International Publishing, Cham (2017). ISBN 978-3-319-53862-4.
- Czaja, P., Aeberhard, U., Celino, M., Giusepponi, S., and Gusso, M. *Optoelectronic properties of a-Si:H and a-Si:H/c-Si interfaces from first principles*. Talk given at the Euro-TMCS II, Cork (2016).
- Czaja, P., Aeberhard, U., Celino, M., Giusepponi, S., and Gusso, M. *Optoelectronic properties of a-Si:H and a-Si:H/c-Si interfaces from first principles*. Talk given at the DPG Spring Meeting, Dresden (2017).
- Czaja, P., Celino, M., Giusepponi, S., Gusso, M., and Aeberhard, U. *Ab initio study on localization and finite size effects in the structural, electronic, and optical properties of hydrogenated amorphous silicon*. *Computational Materials Science* **155**, 159 (2018).
- Czaja, P., Giusepponi, S., Gusso, M., Celino, M., and Aeberhard, U. *Computational characterization of a-Si:H/c-Si interfaces*. *Journal of Computational Electronics* **17** (4), 1457 (2018).

Acknowledgements

First and foremost I would like to express my gratitude to my scientific advisor Urs Aeberhard for patiently guiding me over the course of my thesis work. From proposing the project, to providing plenty of valuable input and advice throughout the research process, and to finally reading and correcting this thesis, he has a large share in this work.

Another major contribution, without which this project could not have been realized, was made by Massimo Celino, Simone Giusepponi, and Michele Gusso, who provided the atomic configurations that formed the starting point of all our calculations. For this, and for the many interesting and fruitful discussions, I would like to thank them.

I am also very grateful to my PhD supervisor Yuriy Mokrousov, who has accompanied my scientific career since my graduate studies, and whose door was (literally) always open.

Furthermore I want to express my appreciation to Prof. Rau for giving me the opportunity to do my PhD in his institute.

Additional thanks go to Christoph Friedrich for his advice on GW calculations, and Markus Ermes for his help with IT issues and his contributions to setting up the computer cluster on which part of the calculations within this thesis were performed.

Finally I want to thank my friends and colleagues from IEK-5 and PGI-1, in particular Marta Gibertini, Flaviano dos Santos, Julen Azpiroz, and Yael Augarten, who made my time at Forschungszentrum Jülich memorable.

This work was funded from the European Commission Horizon 2020 research and innovation program under grant agreement No. 676629, and supported through the COST action MP1406 MultiscaleSolar. Computing time at the supercomputer JURECA [98] was provided by the Jülich Supercomputing Centre.

Band / Volume 480

Structural uptake and retention of safety relevant radionuclides by cementitious materials

S. Lange (2019), 133 pp

ISBN: 978-3-95806-437-9

Band / Volume 481

Quantifying the Impact of Inhomogeneity, Transport and Recombination in Emerging Thin-Film Solar Cells

P. Kaienburg (2019), vii, 258 pp

ISBN: 978-3-95806-440-9

Band / Volume 482

Studies of oxidation resistant tungsten alloys at temperatures of 1100K to 1475K

F. Klein (2019), 158 pp

ISBN: 978-3-95806-444-7

Band / Volume 483

Impact Assessment of Land-Use Change and Agricultural Treatments on Greenhouse Gas Emissions from Wetlands of Uganda and Tanzania

K. X. X. Wagner (2019), 144 pp

ISBN: 978-3-95806-447-8

Band / Volume 484

IEK-3 Report 2019

Tailor-Made Energy Conversion for Sustainable Fuels

D. Stolten, B. Emonts (Eds.) (2020), 162 pp

ISBN: 978-3-95806-451-5

Band / Volume 485

Multiskalare Modellierung integrierter Energie- und Elektrizitätssysteme

T. C. Pesch (2019), XXV, 384 pp

ISBN: 978-3-95806-452-2

Band / Volume 486

Quantitative Untersuchung des Laserablationsprozesses mittels Kombination von optischer Spektroskopie und Massenspektrometrie

J. Oelmann (2020), vii, 141 pp

ISBN: 978-3-95806-453-9

Band / Volume 487

Leistungssteigerung metallgestützter Festelektrolyt-Brennstoffzellen (MSCs) durch gezielte Optimierungen des Anoden/Elektrolytverbunds

C. Bischof (2020), X, 176 pp

ISBN: 978-3-95806-455-3

Band / Volume 488

Aluminiumoxiddispersionsverstärkte Haftvermittlermaterialien in Wärmedämmschichtsystemen

C. Vorkötter (2020), VIII, 99, XXXIII pp

ISBN: 978-3-95806-457-7

Band / Volume 489

The Balmer lines emission of fast hydrogen atoms at the plasma-solid interface in a low density plasma: challenges and applications

S. O. Dickheuer (2020), 117 pp

ISBN: 978-3-95806-458-4

Band / Volume 490

Micromechanical Characterization of Ceramic Solid Electrolytes for Electrochemical Storage Devices

J. F. Nonemacher (2020), xv, 131 pp

ISBN: 978-3-95806-461-4

Band / Volume 491

Nanoscale investigation of high temperature oxidation mechanisms of high-Cr ferritic steels

A. Vayyala (2020), xix, 105 pp

ISBN: 978-3-95806-467-6

Band / Volume 492

Electrolyte development for a SOFC operating at low temperature

J. Zhang (2020), vi, 121 pp

ISBN: 978-3-95806-471-3

Band / Volume 493

Modeling and Simulation of Polymer Electrolyte Fuel Cells

S. Zhang (2020), 4, xii, 214 pp

ISBN: 978-3-95806-472-0

Band / Volume 494

Ab initio perspective on hydrogenated amorphous silicon for thin-film and heterojunction photovoltaics

P. Czaja (2020), 107 pp

ISBN: 978-3-95806-474-4

Weitere **Schriften des Verlags im Forschungszentrum Jülich** unter
<http://www.zb1.fz-juelich.de/verlagextern1/index.asp>

Energie & Umwelt / Energy & Environment
Band / Volume 494
ISBN 978-3-95806-474-4